



University of Sussex

A University of Sussex DPhil thesis

Available online via Sussex Research Online:

<http://sro.sussex.ac.uk/>

This thesis is protected by copyright which belongs to the author.

This thesis cannot be reproduced or quoted extensively from without first obtaining permission in writing from the Author

The content must not be changed in any way or sold commercially in any format or medium without the formal permission of the Author

When referring to this work, full bibliographic details including the author, title, awarding institution and date of the thesis must be given

Please visit Sussex Research Online for more information and further details

Density Functional and Dislocation Theory of Graphite Related to Nuclear Materials

Submitted by

Glen Sheehan

to the University of Sussex as a thesis for the degree of
Doctor of Philosophy in Chemistry in the School of Life Sciences

September 2012

I certify that all the material in this thesis which is not my own work has been identified and that no material is included for which a degree has previously been conferred on me.

Acknowledgements

I would first like to thank EDF energy for their beneficence which has allowed me to undertake and complete my PhD studies.

Thanks to Professor Malcolm Heggie for his support, inspiration and generosity over the years. Thanks also to the rest of the TCCM group past and present for their help and friendship during this time. A special thanks to Pippa for her help with the program.

Thanks to Calvin for the many hours he spent fixing my motorbike during the cold winter months and to James and Jean-Jo for all the times they transported me to and from university. Thanks to Gemma for keeping us on the straight and narrow path during the Britannia Court days - especially on the rare occasions when we needed to curb our enthusiasm.

I would like to thank John and Sam for the great generosity they have shown during my correction writing period.

Finally I would like to thank my family for their unending support. It may have taken a while but I got there in the end.

Abstract

This thesis concerns the physicochemical understanding of radiation damage in graphite. It is structured in two parts, the first being a foundation of elastic and bonding properties in graphite and its intercalation compound with Bromine. The second builds on this with dislocation theory to analyse dimensional change and stored elastic energy. Part 1: Density functional theory (DFT) in the local density approximation (LDA) has been used to study the elastic properties of hexagonal graphite and of Bromine intercalated graphite. The second and third order elastic constants of graphite have been calculated ab initio. The internal strain has been considered and the results include partial and total elastic constant results. The nature of the interlayer binding energy has been studied using DFT with LDA. The London dispersion forces have been applied to the DFT results using a simple Lennard-Jones type model. The results of this study are in good agreement with other theoretical and experimental studies. The zero point energy has also been calculated and its effects applied to the interlayer energy and the related elastic constant C_{33} . This constant has also been calculated for stage-1 and stage-2 Bromine-intercalated graphite in order to aid interpretation of intercalation experiments which try to emulate with Br intercalation, the c-axis dimensional change that occurs from radiation damage. Part 2: A two dimensional dislocation model has been written based on both basal and prismatic dislocations. The model elucidates the stress fields arising from irradiation damage in graphite in either the standard damage model based on prismatic loops or the newly proposed model based on basal dislocations. It illustrates the different physical processes underlying dimensional change and should enable it to be quantified. The energy of the stress fields is calculated and found to be comparable to stored energies measured for graphite irradiated below $250^{\circ}C$.

Contents

Acknowledgements	ii
Abstract	iii
Contents	iv
1 Introduction	1
2 Background Theory	6
2.1 Density Functional Theory and the AIMPRO code	6
2.1.1 Introduction	6
2.1.2 Quantum Computational Calculations	6
2.1.2.1 The Born–Oppenheimer Approximation	7
2.1.2.2 Density Functional Theory	8
2.1.2.3 Local Density Approximation	9
2.1.2.4 Pseudopotentials	9
2.1.2.5 Basis Sets	10
2.1.2.6 k-point sampling	11
2.1.2.7 Structural Optimisation and Total Energy	13
2.2 Interlayer Binding	14
2.3 Lattice Vibrations and Zero Point Energy	16
2.4 Elasticity	19
2.4.1 Introduction	19
2.4.2 Tensors	19

2.4.3	Transformations	19
2.4.4	Stress, Strain and Displacement	22
2.4.5	Hooke's Law	23
2.4.6	Elastic Energy	26
2.4.7	Crystal Symmetry	27
2.4.8	Third Order Elastic Constants	30
2.4.9	Internal Strain	31
2.4.10	Total, Partial and Internal Elastic Constants	32
2.5	Dislocation Theory	34
2.5.1	Introduction	34
2.5.2	Dislocation glide	36
2.5.3	Dislocation Line	37
2.5.4	Burgers Vector	38
2.5.5	Types of Dislocation	40
2.5.6	Isotropy	40
2.5.7	Screw Dislocation	41
2.5.8	Edge Dislocation	42
2.5.9	Strain energy of the edge dislocation	47
2.5.10	Interaction energy	47
2.5.11	Dislocation Loops	48
2.5.12	Anisotropy	49
2.5.13	Anisotropy: Displacement	50
2.5.14	Anisotropic displacement in hexagonal graphite	52
2.5.15	Solutions for complex ϕ	55
2.5.16	Anisotropy: Stress and Energy	56
2.5.17	Interaction energy	57
3	Elastic Properties of Graphite	58
3.1	Elastic Constants	58
3.1.1	Introduction	58

3.1.2	Optimisation	63
3.1.3	Elastic Constants of Graphite	64
3.1.4	Results	67
3.2	Zero Point Energy	70
3.2.1	Method	70
3.2.2	Results	72
3.3	Interlayer Binding	73
3.3.1	Method	76
3.3.2	Results	77
4	Bromine intercalated graphite	81
4.1	Elastic Constants of Brominated Graphite	81
4.1.1	Introduction	81
4.1.2	Method	82
4.1.3	Results	83
5	Modelling Graphite Under Irradiation	85
5.1	Introduction	85
5.1.1	Irradiation damage in graphite	87
5.1.2	2-D Dislocation Models	90
5.1.3	Background	90
5.1.4	DD2D Model	91
5.1.5	Dislocation Types	92
5.1.6	Representation by prismatic dipoles	93
5.1.7	User input and graphical output	95
5.1.8	Boundary Conditions	99
5.1.9	Displacement and energy	101
5.1.10	Method	103
5.1.11	Results	104
6	Conclusion	110

Appendices	113
A Lennard-Jones Script	113
B Lennard-Jones run file	116
List of Figures	118
List of Tables	122
References	122

Chapter 1

Introduction

In the UK approximately $\frac{1}{6}$ of the electricity consumed is generated using nuclear power. There are 16 nuclear reactors currently operating. These are located at nine sites. The most common type of reactor in the UK is advanced gas cooled (AGR). There are 14 AGRs, one Magnox and one pressurised water reactor (PWR).

Thermal reactors play a crucial role in the generation of energy from nuclear power plants. Fast fission neutrons within the reactor must be slowed to down or 'moderated' to allow interactions to take place with the nuclear fuel to sustain the nuclear chain reaction. The neutrons are slowed by multiply colliding with atoms thereby lowering their kinetic energy. There are two types of moderator species commonly used. Water cooled reactors rely on collisions with hydrogen atoms to moderate the neutrons while graphite reactors use carbon atoms.

The last remaining Magnox reactor is currently operating at Wylfa nuclear power station and operated by Magnox Ltd. Magnox reactors are carbon dioxide cooled and graphite moderated. The power station is due to be decommissioned in 2014.

PWRs are the most common type of reactor used throughout the rest of the world. The coolant water is used as a moderator. The only PWR in the UK is Sizewell B run by EDF Energy.

All of the AGRs are operated by EDF Energy. These are Dungeness B, Hinkley Point B, Hunterston B, Hartlepool, Heysham 1, Heysham 2, Torness and

Sizewell B.

The AGRs currently in use throughout the UK have operating temperatures of $\sim 650^{\circ}\text{C}$. Low temperature reactors were in operation during the 1950s with operating temperatures of $\sim 250^{\circ}\text{C}$. The effects of stored energy or “Wigner energy” in irradiated graphite were not well known at this time. Strong releases of Wigner energy at $\sim 250^{\circ}\text{C}$ and $\sim 1400^{\circ}\text{C}$ are now well documented.

The effects of this energy release can lead to dangerous runaway temperatures in the reactor. This was highlighted in the 1957 Windscale accident attributed to the 250°C energy release. This problem has now been eliminated with the current running temperatures of the reactors.

The Windscale accident triggered a period of study into the effects of irradiated graphite. Experimental studies have been carried out using various techniques such as X-ray diffraction, transmission electron microscopy (TEM), high resolution TEM (HRTEM), scanning transmission electron microscopy (STEM), atomic force microscopy (AFM) and scanning electron microscopy (SEM) to shed light on the underlying physics and chemistry of irradiated graphite. The expansion of graphite in the c -direction with a complementary shrinkage in the basal plane is observed as a result of irradiation. This can lead to cracking which is a lifetime limiting type of damage for a reactor. Accompanying this is a complicated energy structure varying with dose and temperature.

Theories have been put forward to explain the results of such experimental observations. A point defect model has been proposed to explain some of these results for low and high temperature regimes based on interstitial and vacancy defects. In this model the interstitial atoms account for the observed c expansion. The model describes relatively immobile interstitial atoms at low temperature. With increased temperature the interstitials are believed to become mobile, joining together to form interstitial dislocation loops. The model accounts for dilation of the basal plane by the healing of vacancy lines at low temperature. The vacancies are considered to be mobile at higher temperatures and migrate to the edge of

the basal planes causing shrinkage on leaving the structure. The shortcomings of this model are discussed later in the thesis.

Graphite is a suitable material for use in the construction of nuclear reactors. It can be manufactured at an industrial scale while maintaining a high degree of purity. The mechanical properties of graphite hold up well under the high temperature environment and neutron fluence experienced in an operating reactor.

Pure hexagonal graphite is one of the most highly anisotropic materials. Manufactured graphite for use in nuclear reactor components must however be highly isotropic to maintain structural strength. The manufacture of suitable graphite begins with the raw material in the form of coke from coal or crude oil refining. The coke is then crushed or milled and mixed with a binder, usually pitch. The resulting product is referred to as a green article which is relatively solid and can be formed to the required shape. The green article is subsequently baked resulting in a solid carbonaceous material. The resulting material is then impregnated with pitch to fill porosity and usually rebaked to carbonise the impregnant. This is repeated until the correct density has been attained. The material is then graphitised at a temperature between $2000^{\circ}C$ and $3500^{\circ}C$ to convert the carbon material into a graphite material. The product is finally treated once again at high temperature to remove further impurities. The final product is highly isotropic with a high crystalline order and low impurity levels.

Outside of the nuclear industry graphite is well known for its anisotropic properties. “Graphein” is the ancient Greek word meaning “to write” and its use is well known in pencils. Graphite has a related use in industry as a lubricant. Other important applications are in lithium-ion batteries suitable for electric vehicles and as brake linings for heavy vehicles. Graphene is a single layer of graphite. It has many potential applications in the electrical industry for example in ultracapacitors, integrated circuits and transistor devices. Graphene is also closely related to nano tubes which consist of relatively long very narrow cylinders of graphene. These also have extraordinary electrical and mechanical properties.

The anisotropic nature of graphite is seen in the weak interlayer binding compared to the very strong intralayer binding. These properties make it a good material for intercalation with other species. The weak interlayer binding offers little resistance to expansion perpendicular to the graphite layers. Other species of atom or molecular layers can be inserted between the layers of the “expanded graphite” creating compounds. The intercalation can occur in a regular periodic manner over many layers. This regular arrangement of the intercalants is known as staging.

Intercalation leads to a wide variety of electrical, thermal and magnetic properties of the compound by adjusting the free carrier concentration of the graphite host. These properties can be controlled by varying the density or staging of the intercalant. Intercalated graphite is not used as widely in industry as graphite is. It does however have many potential applications including supercapacitors, display panels and hydrogen storage. Intercalated graphite also provides a route to large scale graphene production.

The structure of the thesis from this point is as follows. The following chapter covers the theoretical background with reference to the content of chapters three, four and five.

In chapter three I will discuss work carried out on the elastic properties of graphite. This includes calculating the 2nd and 3rd order elastic constants using DFT with LDA. Similar calculations have been carried out previously but it has been useful to revisit these calculations for two reasons. Firstly, for the first time the calculations for geometry optimisation and single point energies have been carried out using the pdddp basis set throughout. This is believed to offer the best results for the elastic constant values of hexagonal graphite using the AIMPRO code. Secondly, it is the first time that the second and third order elastic constants have been calculated using DFT with LDA while taking into consideration the phenomenon of internal strain. It is believed that the calculations provide benchmark figures for hexagonal graphite elastic constants using DFT with LDA.

The zero point energy of hexagonal graphite has also been calculated in this chapter. This calculation has been performed using vibrational mode results calculated by Haffenden [1] along with DFT with LDA calculations from this work.

The final section of chapter three considers the interlayer binding in hexagonal graphite. Calculating the interlayer binding for hexagonal graphite using DFT is known to be problematic. The theory does not account for the London dispersion forces commonly thought to be important to the interlayer binding. A calculation has been performed combining results from DFT with LDA calculations with a simple Lennard-Jones type model used to simulate the dispersion interaction.

Chapter four is concerned with bromine intercalated graphite. The elastic constants C_{33} , C_{44} and C_{55} have been calculated using DFT with LDA. Work carried out by Luyken *et al.* [2] has prompted this investigation. It is possible that intercalated graphite may show some of the properties of irradiated graphite with respect to expansion in the c-direction. This could prove useful in research as an alternative to taking irradiated graphite samples from the core of a nuclear reactor.

The fifth chapter proposes a two dimensional model to study the damage in irradiated graphite. The model is based on the dislocation theory. The introduction of the model is an attempt to bridge the gap between microscopic and macroscopic models currently in use. It is hoped that the simple model will be developed and illuminate damage processes in graphite that currently cannot be investigated using current theories.

Chapter 2

Background Theory

2.1 Density Functional Theory and the AIMPRO code

2.1.1 Introduction

The calculations to be described in Chapter 3 were performed using the AIMPRO code [3, 4, 5]. This code is based on Density Functional Theory (DFT). It is applied to calculations in the following chapters using the local density approximation (LDA).

The general background of DFT, as applied to the calculations reported, is outlined in the following sections. A more detailed description of DFT can be found in, for example, Jensen [6].

2.1.2 Quantum Computational Calculations

Computational methods of quantum mechanical theory are based around solving the Schrödinger equation. The time-independent Schrödinger equation can be written as

$$\hat{H}\Psi = E\Psi \tag{2.1}$$

for the energy E and the wavefunction Ψ . The Hamilton operator \hat{H} is the sum of the kinetic (T) and potential (V) energies of the nucleus (N) and the electrons (e) and their interactions with each other,

$$\hat{H} = T_N + T_e + V_{NN} + V_{Ne} + V_{ee} \quad (2.2)$$

Solving the Schrödinger equation gives the total energy and wave function of the system. From these it is possible to calculate other physical properties such as the geometry of the system, binding energies, vibrational frequencies and so on.

The Schrödinger equation cannot be solved analytically except in a few simple cases. To proceed it is necessary to make approximations to the equation that allow it to be solved computationally. The first approximation that will be discussed is the Born–Oppenheimer approximation.

2.1.2.1 The Born–Oppenheimer Approximation

The difference in mass of nuclei and electrons mean that the electrons move much more quickly than the nuclei. The Born–Oppenheimer approximation considers the nuclei to be stationary when compared to the electrons in the system. This allows the nuclei to be treated classically and as a result the kinetic energy of the nuclei is $T_N = 0$ and the potential of the nuclei V_{NN} constant. The position of the nuclei is then considered at a later stage of the computation when the forces on the nuclei can be calculated from the electronic wave functions.

The term V_{ee} describes the electron–electron interactions. These many body interactions cannot be decomposed into solvable equations so further approximation is required.

There are two popular techniques used for dealing with this problem. One is based on Hartree–Fock theory and the other on Density Functional Theory (DFT). DFT is best suited to describing solid state systems and is used in the AIMPRO code.

2.1.2.2 Density Functional Theory

In 1964 Hohenberg and Kohn [7] proved that the electron charge density, $n(\mathbf{r})$, completely describes the ground state electronic energy of a system. The theory was developed further in the following year by Kohn and Sham [8].

The potential V_{ee} is replaced by an effective potential represented by a functional of the electron density. It was shown [7] that for a non-degenerate ground state the energy and wave function are uniquely defined by the electron density. This means that the Schrödinger equation can be solved using the electron density.

A variational method is used to find the ground state energy of the system. The energy includes the kinetic energy of the electrons T_e and the interaction between the nuclei and the electrons. The previous electron–electron interaction term V_{ee} is broken into two parts: E_C for the Coulomb interaction and E_{xc} for the exchange–correlation. The Schrödinger equation now takes the form,

$$(T_e + [V_{Ne} + E_C + E_{xc}]) = \epsilon_i \psi_i(\mathbf{r}) \quad (2.3)$$

$$n(\mathbf{r}) = \sum_{i \text{ occupied}} |\psi_i(\mathbf{r})|^2$$

The equations in [8] are known as the Kohn–Sham equations. They are effectively one electron equations for non-interacting particles interacting with the averaged field of the other electrons. The solution leads to a charge density $n(\mathbf{r})$. This is in turn expanded into wave functions $\psi_i(\mathbf{r})$. Although the wave functions of these artificial non-interacting particles do not have an exact physical interpretation it can be shown that they give the minimum energy for the system.

To use DFT all energy terms should be expressed as functionals of the electron density. The exchange correlation term $E_{xc}[n]$ can most simply be expressed as a function of the electron density for the homogeneous electron gas. This leads to the requirement for further approximation, this time the local density approximation (LDA).

2.1.2.3 Local Density Approximation

Using the local density approximation the exchange correlation energy E_{xc} can be expressed as,

$$E_{xc}[n] = \int n(\mathbf{r})\epsilon_{xc}[n(\mathbf{r})]d\mathbf{r} \quad (2.4)$$

where ϵ_{xc} is the exchange correlation energy density of the equivalent homogeneous electron gas of electron density $n(\mathbf{r})$. LDA makes the approximation that E_{xc} for any region within the electronic system has a value equal to a homogeneous electron gas having the same density.

Although LDA works well even with rapidly varying electron density it tends to give low ground state energies and overestimates ionisation energies. The generalised gradient approximation (GGA) can be used to try to correct for these errors in the AIMPRO code. The results shown in this paper have been produced using LDA. The exchange correlation energy used in the code comes from work carried out by Perdew and Wang [9] who parametrised quantum Monte Carlo calculations carried out by Ceperley and Alder [10].

The next approximation that will be considered with respect to the AIMPRO calculations is the use of pseudopotentials.

2.1.2.4 Pseudopotentials

The use of pseudopotentials is another approximation built into the AIMPRO code. The electrons closest to the nuclei are strongly bound to it and do not play a noticeable role in chemical bonding. These electrons are classified as the core electrons as opposed to the valence electrons that do play a significant role in bonding. With this approximation the core electrons and nuclei are replaced by a core potential known as the pseudo potential. This replaces the extra KE that valence electrons have in order for their wave functions to be orthogonal to those of the core electrons, with a repulsive potential added to the nuclear potential. The pseudopotential gives the same valence energies and pseudo wavefunctions as the real atomic potentials and wavefunctions outside of the core

region. Inside the core the pseudopotential gives a smoothed out function. To model the core energy accurately involves many fitting functions because of the rapidly oscillating wavefunctions of the real atom. The pseudopotential gives an accurate representation of the energy in the area of interest outside of the core region and reduces the computational expense.

The electrons that are considered to be outside of the core region can be specified. For example the valence electrons do not give an accurate representation of transition metals in the pseudopotential so the electrons from the next shell can also be included in the calculation [6].

The construction of pseudopotentials involves first generating a reasonable all electron wavefunction for the particular atom. The valence orbitals are then replaced by a set of pseudo orbitals and the electron potential is replaced by a trial pseudo potential. These are then “tweaked” to give the correct energy levels and wavefunctions in the area outside of the core region. The pseudo potential is then fitted to analytical functions such as Gaussian functions.

There are three options of pseudopotential available in AIMPRO. These are Hartwigsen, Goedecker and Hutter (HGH) [11] type, Bachelet, Hamann and Schluter (BHS) [12] type and Troullier and Martins (TM) [13] type. The pseudopotentials used for the calculations in this thesis are the HGH type.

The core electron contribution to the energy calculation comes from the pseudo potentials. The wavefunctions to be calculated depend only on the valence electrons. These wavefunctions are expanded in terms of a basis set.

2.1.2.5 Basis Sets

The wavefunctions from the valence electrons $\psi_\lambda(r)$ are expanded in terms of a basis set $\phi_i(r)$ with expansion coefficients c_i^λ ,

$$\psi_\lambda(r) = \sum_i c_i^\lambda \phi_i(r) \quad (2.5)$$

The basis set functions can be plane waves, Wannier functions, Slater type orbitals or Gaussian type orbitals. Gaussian type orbitals have been used throughout.

The basis set expansion used by AIMPRO is of the form

$$\phi_i(r) = (x - R_{ix})^{n_1} (y - R_{iy})^{n_2} (z - R_{iz})^{n_3} e^{-\alpha_i(r-R_i)^2} \quad (2.6)$$

where R_i are the nuclear positions. Here the choice made for the n_i control the type of orbitals used in the calculation.

Using Gaussian orbitals rather than, say, plane waves has the advantage that a relatively small number of basis set functions is required. For the calculations reported in chapter 3 various combinations of orbital types were used. Another advantage is that the integration of Gaussian orbitals can be carried out analytically within the code.

2.1.2.6 k-point sampling

The Kohn–Sham equations are normally solved in k space or reciprocal space. In k space the reciprocal lattice is described by a set of vectors \mathbf{b}_1 , \mathbf{b}_2 , \mathbf{b}_3 . These vectors are related to the real space lattice vectors \mathbf{a}_1 , \mathbf{a}_2 , \mathbf{a}_3 in the following manner

$$\mathbf{b}_1 = 2\pi \frac{\mathbf{a}_2 \times \mathbf{a}_3}{\mathbf{a}_1 \cdot \mathbf{a}_2 \times \mathbf{a}_3}, \mathbf{b}_2 = 2\pi \frac{\mathbf{a}_3 \times \mathbf{a}_1}{\mathbf{a}_1 \cdot \mathbf{a}_2 \times \mathbf{a}_3}, \mathbf{b}_3 = 2\pi \frac{\mathbf{a}_1 \times \mathbf{a}_2}{\mathbf{a}_1 \cdot \mathbf{a}_2 \times \mathbf{a}_3} \quad (2.7)$$

The reciprocal lattice vector \mathbf{b}_1 has the magnitude of $\frac{2\pi}{|\mathbf{a}_1|}$ and is in the direction perpendicular to the plane described by $\mathbf{a}_2 \times \mathbf{a}_3$. Similar relationships hold for \mathbf{b}_2 and \mathbf{b}_3 .

Any point in reciprocal space can be described by the wave vector \mathbf{k} . The area of greatest interest within reciprocal space is the first Brillouin zone (BZ). All electron eigenstates are represented within the BZ. The energy as a function of wave vector, $E(\mathbf{k})$, is often plotted against \mathbf{k} and represented as a ‘band structure’ plot. There can be degeneracy of the energy bands at various points. The bands

are labelled with an index m .

The wavefunction within the crystal must reflect the periodicity of the structure. It takes the Bloch form,

$$\psi_{\mathbf{k}}(\mathbf{r}) = u_{\mathbf{k}}(\mathbf{r}) \cdot e^{i\mathbf{k}\cdot\mathbf{r}} \quad (2.8)$$

The function $u_{\mathbf{k}}$ contains the periodicity of the crystal structure.

In DFT supercell calculations the Kohn–Sham equations are solved for k points in the Brillouin zone,

$$n(\mathbf{r}) = \sum_{m\mathbf{k}} f_{m\mathbf{k}} |\psi_{m\mathbf{k}}(\mathbf{r})|^2 \quad (2.9)$$

The term $f_{m\mathbf{k}}$ takes into account the occupancy of band m at the point \mathbf{k} .

When calculating the charge density at a point \mathbf{r} it is not practical to integrate over all possible k -points in the BZ. Instead, a sum over selected grid of points is used. The calculations presented here have been performed using a k -points selection technique developed by Monkhorst and Pack [14].

The accuracy of the calculation is dependent on the density of k -points in reciprocal space. There is a linear increase in computational time with respect to the number of k -points used. The increase in computational time with the number of atoms specified is approximately n_{atoms}^3 . For this reason it is usually preferable to increase the number of k -points used whilst minimising the number of atoms when finding a suitable accuracy in calculations.

In some cases the use of a high number of atoms is unavoidable. For example a complicated structure without much symmetry. Another situation might be a defect that needs to be isolated from its repeated images in adjacent cells to minimise unwanted interactions. With high symmetry it can be much faster to use a small unit cell with fewer atoms. A higher number of k -points can then be used to give equivalent accuracy to a calculation to that given by a cell containing a larger number of atoms.

2.1.2.7 Structural Optimisation and Total Energy

The total energy and structural optimisation of a supercell can be calculated using AIMPRO with DFT. The technique is based on an iterative procedure.

The process begins with an initial charge density matrix based on that of the atoms contained within the supercell being in isolation. The wave function expansion coefficients c_j are then calculated by solving the Kohn–Sham equations

$$\sum_j (H_{ij} - E_\lambda S_{ij}) c_j^\lambda = 0 \quad (2.10)$$

where H_{ij} is the Hamiltonian matrix and S_{ij} the overlap matrix. A charge density is calculated and compared to the previous charge density. If convergence to predefined criteria is not found then this process is repeated starting with an admixture of old and new charge densities. A common criterion to be met is a certain energy change between iterations. The iterative process is called the self consistent cycle. The cycle is repeated until the criteria are met. The minimum self consistent energy for a certain initial geometry of atoms is found in this way.

The self consistent energy can be used to find the forces felt by the atoms in the supercell. The force

$$F_{\alpha l} = -\frac{\partial E}{\partial R_{\alpha l}} \quad (2.11)$$

describes the force felt by atom α in the direction l . This force, given by the Hellman–Feynman theorem, can be used directly in plane wave calculations. For the Gaussian orbital based calculations used in AIMPRO Pulay corrections are required for incomplete bases [15].

Atom positions within the supercell are optimised using a conjugate gradient method. The atoms are moved along the chosen direction to a point giving minimum energy. Forces are recalculated to give a new direction. Initially the direction is the same as the force (‘steepest descent’) but subsequent directions are chosen to be orthogonal to all previous directions. The procedure is repeated until forces drop below a user defined tolerance. This method is certain to find a

local minimum but cannot guarantee a global minimum.

2.2 Interlayer Binding

The interlayer binding of graphite is believed by many to arise in the main part from dispersion forces [16]. Dispersion forces describe interactions between remote charge distributions. This type of interaction has no overlap of wave functions. Heggie [17] believes that although the dispersion forces play a role in interlayer binding the majority of binding at small strains is due to covalent-like binding from the overlap of p_z orbitals at symmetric points between graphene layers as described by DFT in LDA. This type of binding has also been mentioned by Charlier *et al.* [18].

In quantum mechanics the square of an electron wave function $|\Psi_e(x, y, z)|^2$ describes the probability of finding the particular electron at a position (x, y, z) . Analogous to classical waves the quantum mechanical waves can interfere with one another. For two wave functions Ψ_1 and Ψ_2 this can occur constructively when the wave functions are in phase

$$\Psi_+ = \frac{1}{\sqrt{2}} (\Psi_1 + \Psi_2) \quad (2.12)$$

This leads to an increased probability or electron density compared to the isolated systems. The interaction can be destructive when the wave functions have opposite phase

$$\Psi_- = \frac{1}{\sqrt{2}} (\Psi_1 - \Psi_2) \quad (2.13)$$

In this case probability and electron density are lowered. The third case is that no interaction occurs if the wave functions are orthogonal and out of phase.

In terms of molecular orbital theory if the electrons are considered to be valence electrons of two bound nuclei the constructive interference describes a bonding orbital. In this case the wave functions have equivalent phases and add.

The binding coming from a reduced energy resulting from the increased electron density between the two nuclei when compared to two isolated nuclei.

The destructive interference is described by an antibonding orbital. In this case the phases of the wave function are opposite. This results in an energy greater than that of the isolated nuclei. For the simple case of two bound nuclei with one valence electron each this would lead to the electrons, one with spin up and the other spin down, occupying the energy level described by the combined bonding orbital.

For a carbon atom in graphite three of the four valence electrons are trigonally directed σ bonds in the sp^2 hybrid. The final electron lies in a p_z orbital normal to the plane. They interact with adjacent p_z orbitals from π bonds. Heggie states that overlap of the p_z orbitals belonging to α atoms of adjacent planes play the major role in interlayer binding in graphite from DFT calculations with LDA.

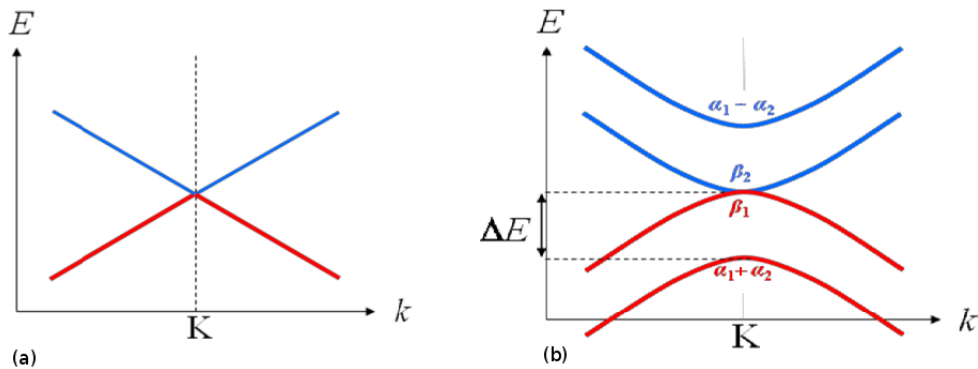


Figure 2.1: (a) Graphene electron bands at K (b) Graphene bilayer bands at K for AB

The idea of the interlayer binding through this mechanism is illustrated in Figure 2.1. The π bands at K for graphene and the π bands at K for bilayer graphene are displayed. The electron bands are degenerate at the point K in graphene. However for bilayer graphene the interaction between the layers can be seen. Bonding arises from the sublattice alignment. The π band electrons belonging to atoms that align along the c direction are described by wave functions α_1 for one layer and α_2 for the other layer. The phases add or subtract thereby lowering or increasing the electron density. The atoms that are aligned with the centre

of a hexagonal ring do not interact as they are out of phase. The relevant wave functions are labelled β_1 and β_2 . The energy ΔE is a measure of the interlayer binding that arises from DFT with LDA calculations.

The term is weak compared to the intralayer binding. This is because it only occurs for Bloch functions around the high symmetry point K in the Brillouin zone. Davison [19] has studied bilayer graphene around K for bilayer graphene. The images in Fig 2.2 have been produced using AIMVIEW and give a visualisation of the wave functions with iso-surfaces. The in phase binding wave function

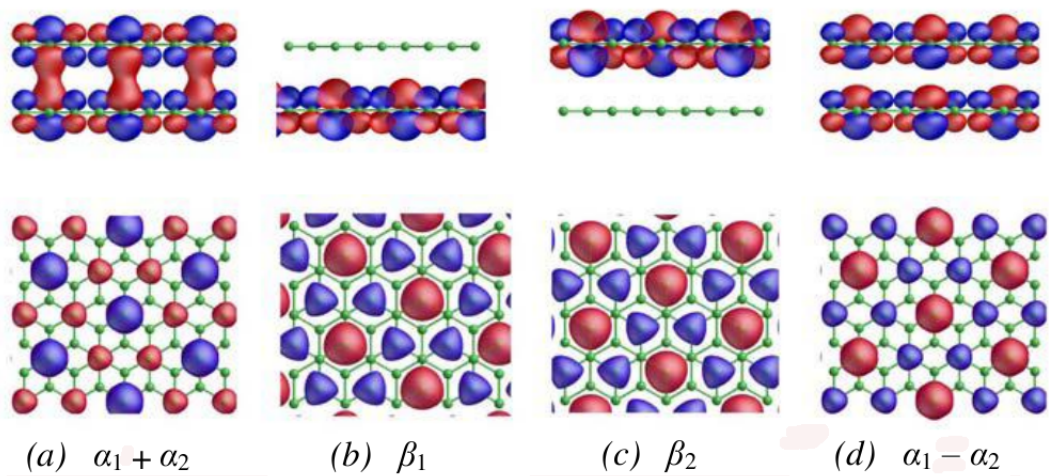


Figure 2.2: Basal direction view (top row) and c-axis view (bottom row) of wave functions at K for graphene bilayer.[19]

Iso-surfaces of positive phase wavefunctions are shown in red while negative phase iso-surfaces are shown in blue.

- (a) $(\alpha_1 + \alpha_2)$ In phase wavefunctions leading to interlayer binding
- (b) and (c) Non interacting, out of phase wavefunctions
- (d) $(\alpha_1 - \alpha_2)$ Opposite phase, anti binding wavefunctions

combinations $(\alpha_1 + \alpha_2)$ are shown in Fig 2.2(a). The non interacting out of phase wave functions are shown in Fig 2.2(b) and Fig 2.2(c). The opposite phase anti binding wave functions $(\alpha_1 - \alpha_2)$ are shown in Fig 2.2(d).

2.3 Lattice Vibrations and Zero Point Energy

Quantum mechanics predicts a residual energy at zero temperature known as the zero point energy. This is a result of the Heisenberg uncertainty principle which describes how certain measurements of a particle cannot yield a result above

a certain accuracy. The reason for this is that an exact result does not exist according to quantum mechanics. The best description that can be given is that the measurement lies within a range of values with a lower limit.

For example how well a moving electron's position can be known is inversely proportional to the momentum of the electron. The relationship between the two measurements can be described by the inequality

$$\sigma_x \sigma_p \geq \frac{\hbar}{2} \quad (2.14)$$

where σ_x and σ_p are the standard deviation of the position of the electron and momentum respectively. The constant \hbar is plank's constant h divided by 2π . Various similar relationships hold for other "conjugate variables" in quantum mechanics. Energy and time are conjugate.

The small vibratory motions of atoms within a crystal can be modelled by independent simple harmonic oscillators with frequencies ν_i . The energy levels are equivalent in both cases. The energy levels of a simple quantum harmonic oscillator are

$$\frac{1}{2}h\nu_i, \frac{3}{2}h\nu_i, \frac{5}{2}h\nu_i, \dots \quad (2.15)$$

The thermodynamical functions of a system can be determined by the energy levels of a system according to statistical mechanics [20]. The Helmholtz free energy

$$F = E - TS \quad (2.16)$$

where E is internal energy, T is temperature and S is entropy can be written as

$$F = -kT \ln Z \quad (2.17)$$

The term Z in Eq 2.17 is the partition function. The partition function is the sum of Boltzmann factors

$$Z = \sum_i \exp\left(\frac{-\epsilon_i}{kT}\right) \quad (2.18)$$

where k is Boltzmann's constant and ϵ_i are the eigenvalues of the energy. Using the energies of the quantum harmonic oscillator in Eq 2.15 the partition function Z_i and free energy F_i due to vibrational motion can be calculated.

For an arbitrary unit cell of hexagonal crystal the free energy at temperature T can be written as [21]

$$F = U_0 + \sum_i \left(\frac{h\nu_i}{2} + kT \ln \left[1 - \exp \left(\frac{-h\nu_i}{kT} \right) \right] \right) \quad (2.19)$$

Summation is taken over all vibrational modes in the unit cell. The term U_0 is the potential energy of the unit cell arising from interatomic interactions. This is sometimes referred to as the static energy. For any deformation of the unit cell the static energy and the frequencies ν_i change.

At zero temperature Eq 2.19 becomes

$$F = U_0 + \sum_i \frac{h\nu_i}{2} \quad (2.20)$$

Here the term $\sum_i \frac{h\nu_i}{2}$ is referred to as the zero point energy. Partially differentiating Eq 2.20 with respect to ϵ_3 and equating to zero leads to

$$\frac{\partial F}{\partial \epsilon_3} = \frac{\partial U_0}{\partial \epsilon_3} + \frac{h}{2} \sum_i \frac{\partial \nu_i}{\partial \epsilon_3} = 0 \quad (2.21)$$

Equation 2.21 can be solved to find the interlayer separation at zero temperature with zero point energy. The second partial differentiation of Eq 2.20 leads directly to the elastic constant term C_{33} at zero temperature with the inclusion of the zero point energy

$$C_{33} = \frac{\partial^2 F}{\partial \epsilon_3^2} = \frac{\partial^2 U_0}{\partial \epsilon_3^2} + \frac{h}{2} \sum_i \frac{\partial^2 \nu_i}{\partial \epsilon_3^2} \quad (2.22)$$

At non zero temperatures the temperature constituent of Eq 2.19 is non zero. This term is referred to as the anharmonic term. The second partial derivative

leads to the term

$$C_{33}^{an} = h \sum_i \left[\frac{\exp(-h\nu_i/kT)}{1 - \exp(-h\nu_i/kT)} \left(\frac{\partial^2 \nu_i}{\partial \epsilon_3^2} \right) - \frac{h}{kT} \frac{\exp(-h\nu_i/kT)}{(1 - \exp(-h\nu_i/kT))^2} \left(\frac{\partial \nu_i}{\partial \epsilon_3} \right)^2 \right] \quad (2.23)$$

2.4 Elasticity

2.4.1 Introduction

In this section the theory of elasticity is discussed. Detailed accounts of elasticity theory can be found in many books including those by the following authors: Love [22], Landau and Lifshitz [23] and Timoshenko [24].

2.4.2 Tensors

The various physical properties of interest in elastic theory are described by tensors. For example, the expressions for stress and strain are tensors of rank two. There is a fourth rank tensor relating the stress tensor to that of the strain. Tensors represent physical quantities related to a set of axes and can be defined by the way that they transform between different sets of axes.

2.4.3 Transformations

A vector is a tensor of rank one. To transform a vector from an initial set of axes to a new set of axes with the same origin a transformation matrix can be constructed. The coordinate systems considered are always cartesian so there is no distinction between covariant and contravariant forms. The axes are all perpendicular and the units of length along each axis are equivalent.

A relationship between the axes can be built up by taking direction cosines of each axis in the first coordinate system with respect to each of the three axes in the transformed coordinate system. The nine cosines a_{ij} can be represented as

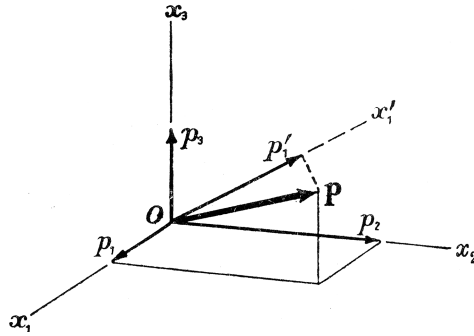


Figure 2.3: Transformation of axes [22]

shown in the following matrix

$$a_{ij} = \begin{bmatrix} a_{11} & a_{12} & a_{13} \\ a_{21} & a_{22} & a_{23} \\ a_{31} & a_{32} & a_{33} \end{bmatrix} \quad (2.24)$$

The entry a_{11} represents the value given by the cosine of the angle between axis x'_1 and axis x_1 . Whereas entry a_{12} represents the cosine of the angle between axis x'_1 and axis x_2 . The first index in a_{ij} represents the original coordinate system and the second index the coordinate system after the transformation.

Once this relationship is known an arbitrary vector can be transformed from one system to another using Eq 2.24. For example the vector \mathbf{P} with entries p_i , shown in Fig. 2.3, can be transformed to the new system, with entries p'_i by matrix multiplication

$$p'_i = a_{ij} p_j \quad (2.25)$$

The Einstein summation convention has been used in Eqn 2.25 and throughout the thesis. Summation over repeated indices contained in a term, such as the j indices in the right hand term of Eqn 2.25, is implied. To highlight the utility of using the Einstein convention the equation is written out in full

$$\begin{aligned} p'_1 &= a_{11}p_1 + a_{12}p_2 + a_{13}p_3 \\ p'_2 &= a_{21}p_1 + a_{22}p_2 + a_{23}p_3 \\ p'_3 &= a_{31}p_1 + a_{32}p_2 + a_{33}p_3 \end{aligned} \quad (2.26)$$

Eqn 2.25 works by taking each of the projections of vector \mathbf{P} onto the original axes x_1, x_2, x_3 and rewriting them as projections onto the new axes x'_1, x'_2, x'_3 . Written out in full the first entry in \mathbf{P}' , as shown in Fig 2.24, is

$$p'_1 = a_{11}p_1 + a_{12}p_2 + a_{13}p_3 \quad (2.27)$$

Similar entries for p'_2 and p'_3 complete the representation of vector \mathbf{P}' in the new coordinate system x'_i in terms of the original x_i .

A vector represented in the coordinates of x'_i can be transformed to one in x_i using the inverse of the matrix a_{ij} . For an orthogonal matrix the inverse is equal to the transpose. So the transformation can be written

$$p_i = a_{ji} p'_j \quad (2.28)$$

The expressions in 2.25 can be used to define a vector. If a vector representing some physical object can be transformed between rotated coordinate systems in this way it is a vector. As already mentioned a vector is a rank one tensor. The rank can be obtained from the number of indices of the particular tensor. This definition of a tensor generalises to all ranks of tensor. For a second rank tensor, such as the strain tensor, two transformation matrices are required to transform the tensor from one coordinate system to another. If the tensor is transformed as

$$\epsilon'_{ij} = a_{ik}a_{jl}\epsilon_{kl} \quad (2.29)$$

then it is a rank two tensor. A similar relationship holds for the transformation of the stress tensor

$$\sigma'_{ij} = a_{ik}a_{jl}\sigma_{kl} \quad (2.30)$$

The highest rank of tensor considered for rotation will be the elastic constant

tensor which is rank four. This requires four transformation matrices for rotation

$$C'_{ijkl} = a_{im}a_{jn}a_{ko}a_{lp}C_{mnop} \quad (2.31)$$

For systems with orthogonal axes of equal length the transformation shown in Eq 2.31 can be performed using matrix multiplication [25]. A 9×9 entry matrix Q_{ijkl} can be created from the relevant rotation matrices

$$Q_{mnkl} = a_{km}a_{ln} \quad (2.32)$$

An expression for the rotation of the elastic constant tensor can be put into the form of matrix multiplication using the transpose \tilde{Q} of Q

$$C'_{ijkl} = \tilde{Q}_{ijgh}C_{ghmn}Q_{mnkl} \quad (2.33)$$

The number of entries contained within a tensor of rank n is related to the number of coordinates in the coordinate system it is being represented in. The relationship for a three coordinate system is 3^n . For the elastic tensor of rank four there are $3^4 = 81$ possible entries. However, the number of entries is greatly reduced by various symmetries.

2.4.4 Stress, Strain and Displacement

The displacement vector,

$$\mathbf{u} = (u_1, u_2, u_3) \quad (2.34)$$

describes the displacement of a strained point inside a body of material relative to the point when the body is unstrained. It has the dimension of length. The displacement vector is related to the second order strain tensor ϵ in the following way,

$$\epsilon_{ij} = \frac{1}{2} \left(\frac{\partial u_i}{\partial x_j} + \frac{\partial u_j}{\partial x_i} \right) \quad (2.35)$$

The strain tensor has nine entries and is dimensionless. It contains values for the shear strains and the normal strains. The normal strains ϵ_{ii} measure the fractional change in length along the normal axes. The shear strains, ϵ_{ij} where $i \neq j$, measure the amount of shear as shown in Fig. 2.4. The partial differential $\frac{\partial u_y}{\partial x}$ gives the angle between the undeformed line AB and the deformed AB' for small strains. This is similar for $\frac{\partial u_x}{\partial y}$ and the lines AD and AD' . The lines AB' and $D'C'$ are parallel. The same is true for AD' and $B'C'$ so shearing leaves the volume unchanged.

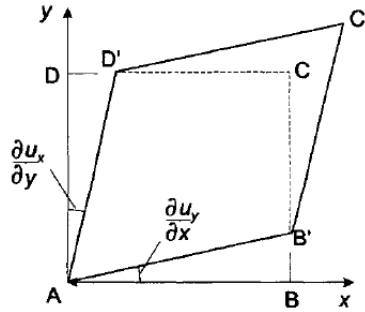


Figure 2.4: Shear on an area element [26]

In Cartesian coordinates the second order stress tensor σ_{ij} represents the forces applied to the faces of an infinitesimal cube as shown in Fig. 2.5. The dimensions are force per area or pressure. The j component of stress refers to the outward normal direction of a particular face while the i component refers to the direction of the force along the face.

2.4.5 Hooke's Law

Hooke's law can be used to relate the stress tensor to the strain tensor. It is valid when strains are small. According to Hooke's law strain is proportional to stress for small deformations. The two tensors are related linearly with the constants of proportionality contained in a fourth rank tensor with 81 entries. Writing the stresses as linear functions of the strains the relationship can be represented as,

$$\sigma_{ij} = C_{ijkl}\epsilon_{kl} \quad (2.36)$$

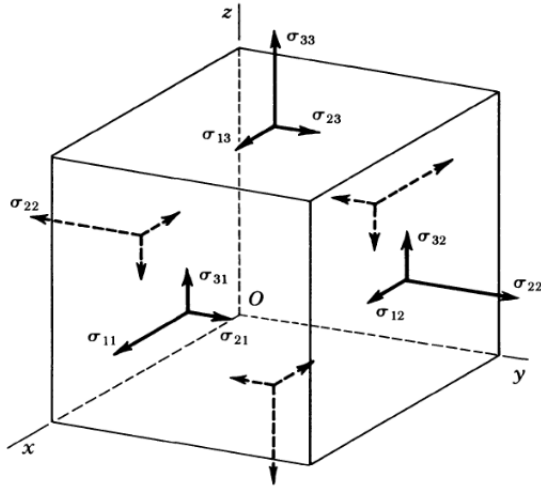


Figure 2.5: Stress on an infinitesimal cube [25]

Here C is the elastic stiffness tensor containing the elastic stiffness constants, commonly referred to as the elastic constants. The dimensions of the elastic constants are force per area or energy per volume.

The relationship between stress and strain can also be written as,

$$\epsilon_{ij} = S_{ijkl}\sigma_{kl} \quad (2.37)$$

In this case the tensor S is made up of the elastic compliance constants. The constants in S have the dimensions of area per force or volume per energy, the inverse units of the elastic constants.

In chapter 3 the elastic constants are calculated, so the version of Hooke's law that is appropriate is that of Eq 2.36. The relationship can be displayed in matrix form with 9×1 matrices for the stress and strain components and a 9×9 matrix

The equations now take the form

$$\begin{bmatrix} \sigma_1 \\ \sigma_2 \\ \sigma_3 \\ \sigma_4 \\ \sigma_5 \\ \sigma_6 \end{bmatrix} = \begin{bmatrix} C_{11} & C_{12} & C_{13} & C_{14} & C_{15} & C_{16} \\ C_{21} & C_{22} & C_{23} & C_{24} & C_{25} & C_{26} \\ C_{31} & C_{32} & C_{33} & C_{34} & C_{35} & C_{36} \\ C_{41} & C_{42} & C_{43} & C_{44} & C_{45} & C_{46} \\ C_{51} & C_{52} & C_{53} & C_{54} & C_{55} & C_{56} \\ C_{61} & C_{62} & C_{63} & C_{64} & C_{65} & C_{66} \end{bmatrix} \begin{bmatrix} \epsilon_1 \\ \epsilon_2 \\ \epsilon_3 \\ 2\epsilon_4 \\ 2\epsilon_5 \\ 2\epsilon_6 \end{bmatrix} \quad (2.40)$$

2.4.6 Elastic Energy

In the limit of small deformations the elastic energy density is quadratic. It can be thought of as a generalisation of the one dimensional potential energy for a spring, $E = \frac{1}{2}kx^2$, where k is the spring constant and x the displacement of the spring. In three dimensions the change in elastic energy from deformation is given as the work done by the stresses on a unit element,

$$dw = \sigma_i d\epsilon_i \quad (2.41)$$

using contracted notation. This is equivalent, by the generalised Hooke's law, Eq 2.36, to

$$dw = C_{ij}\epsilon_j d\epsilon_i \quad (2.42)$$

Partially differentiating Eq 2.42 with respect to the two strain terms leads to an expression of the elastic constant in terms of the energy density

$$C_{ij} = \frac{\partial^2 w}{\partial \epsilon_i \partial \epsilon_j} \quad (2.43)$$

The order of differentiation does not change the result so

$$C_{ji} = \frac{\partial^2 w}{\partial \epsilon_j \partial \epsilon_i} \quad (2.44)$$

is equivalent to Eq 2.43 and

$$C_{ij} = C_{ji} \quad (2.45)$$

The independent elastic constants are now reduced to 21 entries. This is the maximum number of independent elastic constants allowed for a crystal. This number is usually reduced by the symmetries of the particular crystal structure being investigated.

An expression for the elastic strain energy density is given by integrating Eq. 2.42,

$$w = \frac{E}{V_0} = \frac{1}{2} C_{ij} \epsilon_i \epsilon_j \quad (2.46)$$

where E is the strain energy and V_0 is the unstrained unit volume.

2.4.7 Crystal Symmetry

The symmetry of perfect crystal structures can highlight further dependent or zero valued elastic constants. The study of internal crystal symmetry was carried out independently by Federov, Schoenflies and Barlow in the nineteenth century. It was found that crystals could be arranged into 32 different classes built up from different symmetry elements. If an operation can be performed on the crystal geometry which changes the position of any of its points but leaves it coincident with itself it is said to be a symmetry operation.

There are three types of symmetry operation used to describe the crystal classes:

1) Reflection through a mirror plane. A plane of reflection symmetry that converts a point to its mirror image through a mirror plane. For a mirror plane $x_1 x_2$ a point (x_1, x_2, x_3) will be transformed to the point $(x_1, x_2, -x_3)$. This is similar for any other mirror plane. The Hermann–Mauguin symbol for a mirror plane is m .

2) Rotation about an axis. A rotation through an angle of $\frac{2\pi}{n}$ about an axis, where n is a number 1, 2, 3, 4 or 6 and the axis is known as an n -fold axis. The Hermann–Mauguin symbol used for a n -fold axis of symmetry is the number n .

3) Rotation followed by inversion. For an n -fold axis of rotatory inversion there is first a rotation through an angle $\frac{2\pi}{n}$. This is followed by inversion through a centre where inversion is described as transforming a point (x_1, x_2, x_3) into $(-x_1, -x_2, -x_3)$. The Hermann–Mauguin symbol used for a rotatory inversion axis is $\bar{1}, \bar{2}, \bar{3}, \bar{4}$ or $\bar{6}$.

The Hermann–Mauguin symbols are commonly used to identify the symmetry operations. The first symbol identifies the principal axis. For graphite this is the x_3 axis which is a 6-fold axis of rotation. For a mirror plane normal to a n -fold rotation axis this is labelled n/m . There are three mirror axes normal to the six-fold rotation axis in graphite and the Hermann–Mauguin symbol is usually written as $6/mmm$.

This information can be used in conjunction with the transformation rules of tensors described in section 2.4.3 and the generalised Hooke’s law 2.36 to show dependent or zero valued elastic constants. Any of the three symmetry operations allowed for a certain crystal class must leave the elastic constants unchanged. By the rules of tensor transformation Hooke’s law must hold for an arbitrary transformation. By comparing these two the relationships between the transformed and untransformed elastic constants can be compared and the independent elastic constants can be found.

For graphite a rotation around the x_3 axis by an angle $\frac{\pi}{3}$ must leave the elastic constants unchanged by symmetry. In terms of the transformation matrix Eq 2.24 this takes the form

$$\{a\} = \begin{bmatrix} \frac{1}{2} & \frac{\sqrt{3}}{2} & 0 \\ -\frac{\sqrt{3}}{2} & \frac{1}{2} & 0 \\ 0 & 0 & 1 \end{bmatrix} \quad (2.47)$$

Using this matrix the strain tensor can be transformed using Eq 2.29

$$\begin{aligned}
\epsilon'_{11} &= \frac{1}{4}\epsilon_{11} + \frac{3}{4}\epsilon_{22} + \frac{\sqrt{3}}{4}\epsilon_{12} \\
\epsilon'_{22} &= \frac{3}{4}\epsilon_{11} + \frac{1}{4}\epsilon_{22} - \frac{\sqrt{3}}{4}\epsilon_{12} \\
\epsilon'_{33} &= \epsilon_{33} \\
\epsilon'_{23} &= \frac{1}{2}\epsilon_{23} - \frac{\sqrt{3}}{2}\epsilon_{31} \\
\epsilon'_{31} &= \frac{\sqrt{3}}{2}\epsilon_{23} + \frac{1}{2}\epsilon_{31} \\
\epsilon'_{12} &= -\frac{\sqrt{3}}{2}\epsilon_{11} + \frac{\sqrt{3}}{2}\epsilon_{22} - \frac{1}{2}\epsilon_{12}
\end{aligned} \tag{2.48}$$

Sets of equations for the transformed elastic constants can be written out using Eq 2.31 for the constants: C_{11} , C_{22} , C_{12} , C_{66} , C_{16} and C_{26} . Adding the first four expressions results in the following equations [22]

$$\begin{aligned}
C_{11} - C_{22} &= -\frac{1}{2}(C_{11} - C_{22}) - \sqrt{3}(C_{16} + C_{26}) \\
C_{16} + C_{26} &= \frac{\sqrt{3}}{4}(C_{11} - C_{22}) - \frac{1}{2}(C_{16} + C_{26})
\end{aligned} \tag{2.49}$$

From these expressions it follows that $C_{11} = C_{22}$ and $C_{26} = -C_{16}$. Although it can also be shown that C_{16} and C_{26} are equal to zero. The rest of the symmetries can be found using similar expressions. The results lead to five independent elastic constants: C_{11} , C_{12} , C_{13} , C_{33} and C_{44} . These are displayed in matrix form

$$\{C\} = \begin{bmatrix} C_{11} & C_{12} & C_{13} & 0 & 0 & 0 \\ C_{12} & C_{11} & C_{13} & 0 & 0 & 0 \\ C_{13} & C_{13} & C_{33} & 0 & 0 & 0 \\ 0 & 0 & 0 & C_{44} & 0 & 0 \\ 0 & 0 & 0 & 0 & C_{44} & 0 \\ 0 & 0 & 0 & 0 & 0 & C_{66} \end{bmatrix} \tag{2.50}$$

2.4.8 Third Order Elastic Constants

The elastic strain energy density for the second order terms, Eq 2.46, can be extended to accomodate the third order terms [23],

$$w = \frac{1}{2!}C_{ij}\epsilon_i\epsilon_j + \frac{1}{3!}C_{ijk}\epsilon_i\epsilon_j\epsilon_k \quad (2.51)$$

Differentiating the energy density with respect to the three strain terms gives an expression for the third order elastic constant analogous to Eq 2.43

$$C_{ijk} = \frac{\partial^3 w}{\partial \epsilon_i \partial \epsilon_j \partial \epsilon_k} \quad (2.52)$$

Symmetry can be applied to the third order elastic constant tensor C_{ijk} in a similar way to that outlined in the previous section [27]. In the third order there are 10 independent elastic constants. The symmetry properties of the second and third order hexagonal graphite elastic constants are summarised in table 2.1.

C_{11}	$C_{11} = C_{22}$
C_{12}	$C_{13} = C_{23}$
C_{13}	$C_{55} = C_{44}$
C_{33}	$C_{66} = \frac{1}{2}C_{11} - C_{12}$
C_{44}	
C_{111}	$C_{112} = C_{111} - C_{166} - 3C_{266}$
C_{113}	$C_{122} = C_{111} - 2C_{166} - 2C_{266}$
C_{133}	$C_{222} = C_{111} + C_{166} - C_{266}$
C_{333}	$C_{123} = C_{113} - 2C_{366}$
C_{144}	$C_{223} = C_{113}$
C_{244}	$C_{233} = C_{133}$
C_{344}	$C_{155} = C_{244}$
C_{166}	$C_{255} = C_{144}$
C_{266}	$C_{355} = C_{344}$
C_{366}	$C_{456} = \frac{1}{2}(C_{244} - C_{144})$

Table 2.1: Symmetry of the Second and Third Order Elastic Constants of Hexagonal Graphite

2.4.9 Internal Strain

In a crystal each lattice point is associated with one or more atoms or other physical units. The lattice may be reduced to sublattices representing part of the whole lattice. The different sublattices may have their own symmetry. The symmetry class of a crystal cannot be used to infer the symmetry of the sublattices. This is illustrated by considering hexagonal diamond and hexagonal graphite which share the same space group $P6_3/mmc$ (number 194 in the International Tables for Crystallography [28]) but have different sublattice point symmetries $3m$ and $\bar{6}m2$ respectively [29]. A full formal treatment of the symmetries found in four allotropes of carbon, including hexagonal graphite, has been carried out by Cousins [30, 31, 29, 27]

The effect of differing sublattice and crystal symmetry can be observed when certain strains are applied to the crystal. Under homogeneous lattice strain the internal strains arrange in such a way as to minimise the Helmholtz free energy [32]. The atoms will find a lower energy geometry than the positions they would occupy under homogeneous strain of the lattice and sublattice. This relative displacement of the atoms cannot be described under the usual macroscopic version of strain. Internal strain is used to describe the sublattice strains.

Two necessary conditions for this type of relative displacement are:

- 1) there are more than one sublattice per lattice point
- 2) at least one of the sublattices does not contain inversion symmetry

Fig 2.6 illustrates the relative displacements of two sublattices L_α and L_β . To describe the general displacement between a point on L_α and one on L_β a vector $\mathbf{r}^{\alpha\beta}$ is used. In the unstrained state the vector $\mathbf{r}_0^{\alpha\beta}$ describes the displacement as shown in Fig 2.6(a). For a strain J applied to the lattice the sublattice vector can be described as

$$\mathbf{r}^{\alpha\beta} = J\mathbf{r}_0^{\alpha\beta} + \delta^{\alpha\beta} \quad (2.53)$$

Fig 2.6(b) illustrates the case of a strain applied to the lattice resulting in zero relative internal strain. The interlattice vector $\mathbf{r}_0^{\alpha\beta}$ becomes $J\mathbf{r}_0^{\alpha\beta}$. The vector

$\delta^{\alpha\beta}$, describing the internal displacement relative to the homogeneously strained lattice points, is zero. Fig 2.6(c) shows the case when asymmetrical displacement of the sublattices with respect to the applied strain of the lattice does occur. For this case $\delta^{\alpha\beta}$ has magnitude and direction equal to the displacement of the points relative to the homogeneous strain positions $J\mathbf{r}_0^{\alpha\beta}$. Graphite is made up of four

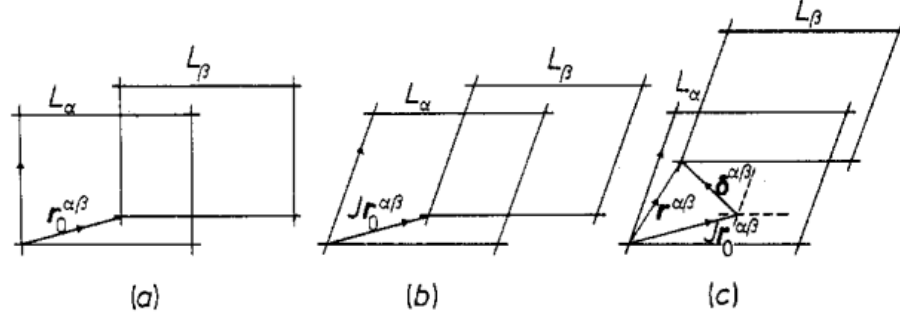


Figure 2.6: The relative displacement of two sublattices: L_α and L_β
 (a) Interlattice vector $\mathbf{r}_0^{\alpha\beta}$ in the undeformed state
 (b) Homogeneous strain J causes no internal strain
 (c) $\delta^{\alpha\beta}$ has magnitude and direction equal to the displacement of the points relative to the homogeneous strain positions $J\mathbf{r}_0^{\alpha\beta}$
 [30]

atoms per lattice point and has the necessary sublattice symmetry for relative displacement of the atoms to take place under certain strains.

2.4.10 Total, Partial and Internal Elastic Constants

The second and third order elastic constants contained in Eq 2.51 are also known as the total elastic constants [29] or the macroscopic elastic constants [32]. They describe the sum of the contributions to the energy per initial unit volume from the homogeneously strained lattice and the internally strained sublattices. The strain energy density, Eq 2.45, can be expressed in a way that displays the contributions from the lattice strain, the internal strain and combinations of the two [27].

$$\begin{aligned}
 w(\zeta^\lambda, \eta) = & \frac{1}{2}C_{IJ}^0\eta_I\eta_J + D_{iJ}^\lambda\zeta_i^\lambda\eta_J + \frac{1}{2}E_{ij}^{\lambda\mu}\zeta_i^\lambda\zeta_j^\mu + \frac{1}{6}C_{IJK}^0\eta_I\eta_J\eta_K \\
 & + \frac{1}{2}D_{iJK}^\lambda\zeta_i^\lambda\eta_J\eta_K + \frac{1}{2}E_{ijk}^{\lambda\mu}\zeta_i^\lambda\zeta_j^\mu\eta_K + \frac{1}{6}F_{ijk}^{\lambda\mu\nu}\zeta_i^\lambda\zeta_j^\mu\zeta_k^\nu \quad (2.54)
 \end{aligned}$$

The indices I, J, K are used for lattice strain and i, j, k for sub-lattice strain while λ, μ and ν denote the particular sublattice atom. In the above expression the Lagrangian strain has been used which makes the expression for the energy density thermodynamically rigorous. These have been replaced by the infinitesimal strain 2.35 for the calculations presented in Chapter 3. The Lagrangian strain

$$\eta_{ij} = \frac{1}{2} \left(\frac{\partial u_i}{\partial x_j} + \frac{\partial u_j}{\partial x_i} + \frac{\partial u_i}{\partial x_j} \frac{\partial u_j}{\partial x_i} \right) \quad (2.55)$$

contains the extra term $\frac{\partial u_i}{\partial x_j} \frac{\partial u_j}{\partial x_i}$. For the calculations of the elastic constants the strains used are between $\epsilon = -0.008$ and $\epsilon = 0.008$ resulting in a negligible value for this extra term.

The terms C_{IJ}^0 and C_{IJK}^0 are partial elastic constants. These have values equal to the total elastic constants (the term used to differentiate the elastic constants as discussed up until now) when there are no contributions to the energy from internal strain.

The terms in D, E and F describe interactions solely from the internal strain or as combinations of the internal and external strain. The measure of the internal strain is given by ζ^λ terms.

The total elastic constants can be written in the form

$$\begin{aligned} C_{IJ} &= C_{ij}^0 + \Delta_{ij} \\ C_{IJK} &= C_{ijk}^0 + \Delta_{ijk} \end{aligned} \quad (2.56)$$

The terms in Δ_{IJ} and Δ_{IJK} contain the terms from resulting from non-zero contributions from the internal strains to the energy density. This is the form that is used to calculate the hexagonal graphite elastic constants in Chapter 3.

For hexagonal graphite there is only one independent Δ_{ij} term and seven Δ_{ijk} terms. These are summarised in Table 2.2.

Δ_{ij}	Δ_{ijk}
Δ_{11}	Δ_{111}
$\Delta_{12} = -\Delta_{11}$	Δ_{113}
	Δ_{144}
	$\Delta_{244} = -\Delta_{144}$
	Δ_{166}
	Δ_{266}
	$\Delta_{366} = \Delta_{113}$

Table 2.2: Δ_{ij} and Δ_{ijk} terms for hexagonal graphite

2.5 Dislocation Theory

2.5.1 Introduction

This section concerns the theory of dislocations. An introductory text on dislocations has been written by Hull and Bacon [26]. Other more advanced texts have been written by Nabarro [33] and Cottrell [34] amongst others. The classic text describing dislocation theory is considered to be by Hirth and Lothe [25].

When considering deformation of crystalline materials such as graphite there are two types of process that can occur. The first is an elastic process. A stress is applied to some material making it deform. When the source of stress is removed the material returns to the unstressed state. This is a purely elastic process. The second process once again begins with stress applied to some material resulting in deformation. When the stress is removed, however, the material does not return completely to its unstrained state. The material in the second case has undergone some plastic deformation. Dislocation theory describes plastic deformation.

A dislocation is a form of line defect in a crystal solid. A perfect crystal, therefore, is dislocation free. In reality there are almost certainly no perfect crystalline structures. There will always be more or less defects made up of point, line, surface and volume types contained within a crystal.

The first observations of regions of plastic deformation by slip in metals were from Mugge [35] and Ewing and Rosenhain [36] towards the end of the 19th Century. The interpretation of the observations was obscure at a time when the

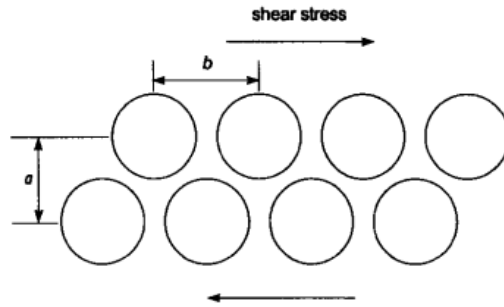


Figure 2.7: Frenkel model used to calculate the required shear stress σ for moving one atomic layer over another [26]

a interlayer spacing

b intralayer spacing

crystalline structure of metals had not been discovered. After the discovery it was accepted that the regions of the crystals had slipped relative to non slipped regions by a shearing process.

In the early 20th Century Volterra [37] applied elastic theory to homogeneous isotropic materials cutting and deforming hollow cylinders in various ways. Some of the applied deformations can be recognised as dislocations. This work was extended by Love [22] and others.

The development of dislocation theory as applied to crystalline structures came about as a way of reconciling theory with experimental evidence. Plastic deformation via shearing of a single perfect crystal without dislocations would involve moving one layer of crystal rigidly over another. Frenkel [38] used a simple model, Fig 2.7, to calculate the required stress σ_{app} for this type of operation to occur

$$\sigma = \frac{\mu b}{2\pi a} \sin \frac{2\pi x}{b} \quad (2.57)$$

where μ is the shear modulus, b is the atomic intralayer spacing, a the interlayer spacing and x the displacement of the layers from equilibrium. The sine term takes into account the atomic periodicity along the plane. Taking the small angle approximation $\sin(2\pi x/b) \approx 2\pi x/b$. With this approximation the maximum value

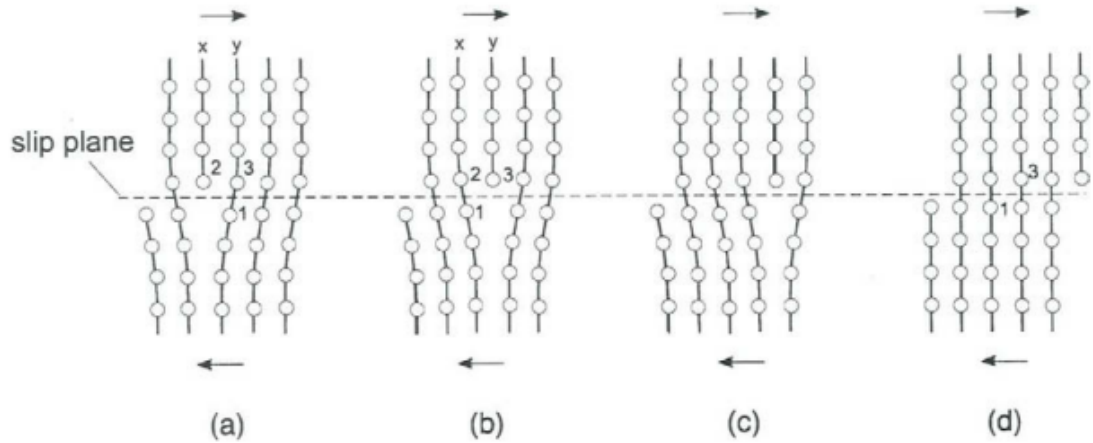


Figure 2.8: Edge dislocation moving by glide along a slip plane [26]

of σ results in a theoretical shear stress to move one layer over another

$$\sigma_{th} = \frac{\mu b}{2\pi a} \quad (2.58)$$

This formula is very approximate but it shows that σ_{th} should be a reasonable fraction of the shear modulus μ . Experimental work carried out, for example by Tinder [39] on bulk copper, showed that plastic deformation begins with applied shear stress of $\sigma_{app} = 10^{-9}\mu$. Such a large difference between σ_{app} and σ_{th} rules out rigid displacement as a mechanism for plastic deformation.

A solution to the discrepancy between the theoretical stress and the experimental stress was given by Orowan [40], Polanyi [41] and Taylor [42] in 1934. They described dislocations as a mechanism to describe plastic deformation under small shear stresses. It is far easier for a dislocation to affect plastic slip by passing through material than for a layer to be displaced rigidly.

2.5.2 Dislocation glide

The way in which the dislocation glides along a glide plane is shown in Fig 2.8. This is the case for a perfect edge dislocation as described in Sec (2.5.8). In Fig 2.8(a) a half plane is terminated with the atom labelled (2). The section of crystal is under shear in the direction shown by the arrows at top and bottom of

the figures. As the dislocation glides to the right in Fig 2.8(b) atom (3) denotes the termination of a half plane while atom (1) bonds to atom (2) completing a full plane. A similar operation occurs until the dislocation leaves the crystal section Fig 2.8(d) leaving a slip step.

In the above example the direction taken by the dislocation is dependent on the extra material introduced. In this case the extra material between the planes is in the form of an extra half plane inserted above the glide plane. This formulation is known as a positive edge dislocation. For a situation where the half plane is inserted below the glide plane the dislocation would move in the opposite direction i.e. towards the left. A dislocation of this type is known as a negative edge dislocation.

2.5.3 Dislocation Line

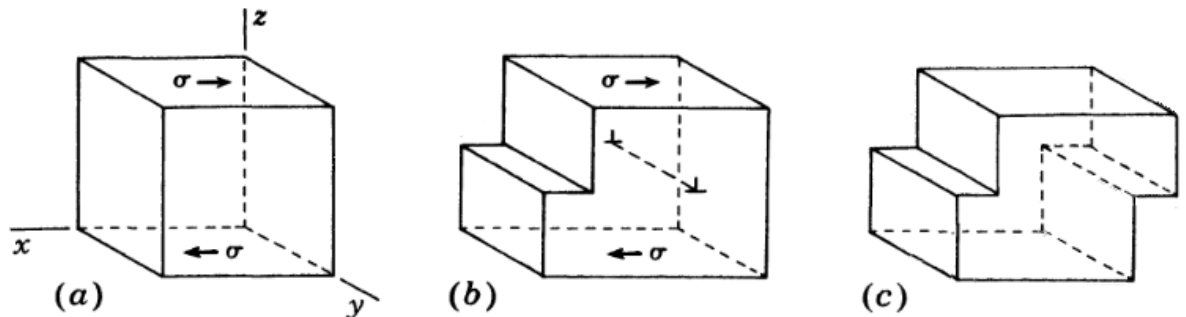


Figure 2.9: (adapted from [25])

(a) Shear applied to perfect crystal

(b) Dislocation moves from left to right leaving slip step to left

(c) Dislocation leaves slip step to right on leaving crystal

A perfect crystal is under stress σ as shown in Fig 2.9(a). It is cut along an xy plane at half its height and displaced in the direction of applied stress 2.9(b) then rejoined leaving a step. The material is conserved and slips over the material below under the influence of the stress. The dislocation line lies between the two inverted “T” symbols and marks the boundary between the slipped and unslipped region in the crystal. The dislocation has left the crystal in Fig 2.9(c) leaving a slip step. No internal strain remains in the crystal after the dislocation has exited

but plastic deformation has occurred.

The movement of a dislocation by shear in this way is known as glide. Its movement is described as conservative with the number of atoms being the physical property being conserved. The xy plane that the dislocation swept across in the above example is known as a glide plane. Shear displacement by a number of dislocations is more commonly referred to as slip.

2.5.4 Burgers Vector

One of the most fundamental properties of a dislocation is the dislocation displacement vector known as the Burgers vector. To calculate the Burgers vector of a dislocation a path from atom to atom can be taken around the defect as shown in Fig 2.10. This is known as a Burgers circuit. There are two alternative ways to calculating the Burgers vector using this method as described by Bilby *et al.* [43]. For both cases the line vector ξ of the dislocation is taken to be pointing into the page. The Burgers circuit is then taken in a right handed sense relative to the line vector.

A path in Fig 2.10(a) beginning at (S)tart in the dislocated crystal continues to (F)inish via points 1, 2 and 3. A similar path is then repeated in a defect free crystal of the same material as shown in Fig 2.10(b). The vector that closes the circuit in the perfect crystal is chosen to begin at F and end at S. This is the Burgers vector as defined by the FS/RH (finish to start/right hand) convention.

The second approach to defining the Burgers vector is to use a Burgers circuit taken from S to F firstly in a perfect crystal as shown in Fig 2.10(c). The S and F coincide in this case. This path is repeated in Fig 2.10(d) enclosing the dislocation in the second crystal. The vector closing the circuit is this time taken from S to F in the dislocated crystal. This convention is known as SF/RH (start to finish/right hand). The vector defined in this way is known as the *local* Burgers vector [43].

As the closure vectors for the two different methods of calculating the Burgers and local Burgers vectors are in the perfect and strained crystals respectively they

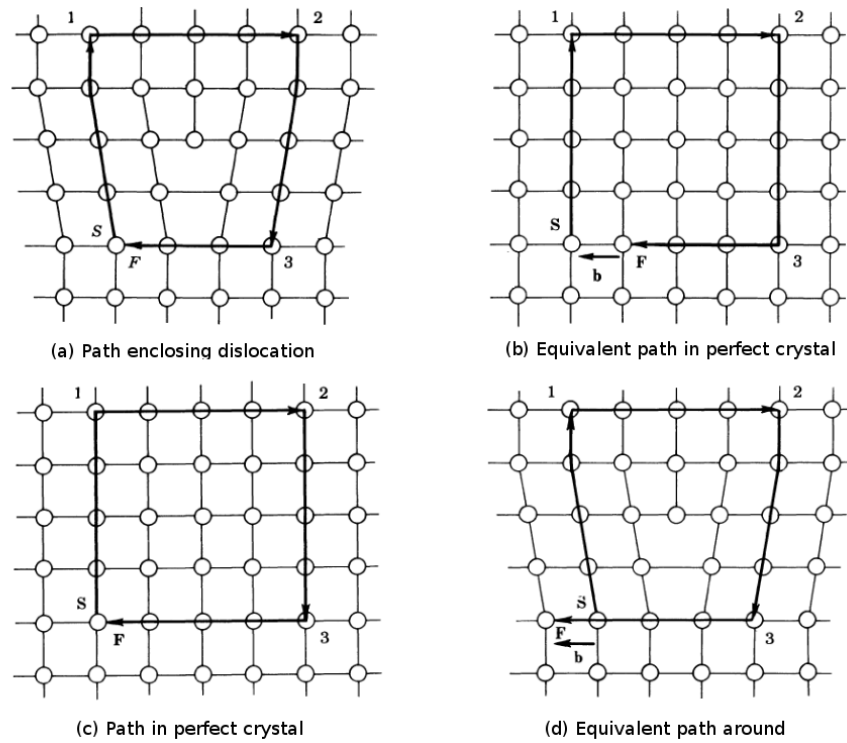


Figure 2.10: Burgers circuit [25]

(a), (b) begin by creating a path around the deformation (a). This is then repeated in the perfect crystal (b). The Burgers vector is the vector closing the circuit from finish (F) to start (S)

(c), (d) a path is drawn inside the perfect crystal (a). This path is then taken around the crystal containing the deformation (b). The Burgers vector, in this case, is the vector pointing from start (S) to finish (F).

are not identical. For a dislocation in an otherwise perfect crystal the two methods tend towards equality for large Burgers circuits [43]. The Burgers vector method was used by Burgers [44] and others while the local Burgers vector method was used by Peach and Koehler [45], Bilby [43] and others. The Burgers vector as opposed to the local Burgers vector is used in this thesis.

2.5.5 Types of Dislocation

The two fundamental dislocation types are screw and edge. Dislocations that are not pure edge or screw can be described as a combination of these two. A pure edge dislocation has a Burgers vector \mathbf{b} perpendicular to the line vector ξ where as a screw dislocation has a Burgers vector parallel to the line vector. The stress, strain and displacements for the case of the screw dislocation are straight forward to calculate. The edge dislocation is more complicated.

2.5.6 Isotropy

The simplest lattice to describe is the simple cubic lattice. Three elastic constants are required to describe this system: C_{11} , C_{12} and C_{44} . For the case of a simple cubic lattice with elastic isotropy only two of the three elastic constants are independent. These two elastic constants are often referred to using the symbols λ and μ . Here λ is known as the Lamé constant and $\lambda = C_{12}$. The shear modulus C_{44} is represented by μ . These two constants are related by the expression,

$$\mu = C_{44} = \frac{1}{2}(C_{11} - C_{12}) \quad (2.59)$$

It can be seen from this relationship that $C_{11} = \lambda + 2\mu$.

From these expressions Hooke's law Eq 2.36 can be written for the isotropic case

$$\sigma_{ii} = (\lambda + 2\mu) \epsilon_{ii} + \lambda (\epsilon_{jj} + \epsilon_{kk}) \quad (2.60)$$

for $i \neq j \neq k$ and for the remaining terms

$$\sigma_{ij} = 2\mu\epsilon_{ij} \quad (2.61)$$

where $i \neq j$. Also, the components of the elastic constant tensor can be represented as,

$$C_{ijkl} = \mu(\delta_{ik}\delta_{jl} + \delta_{il}\delta_{jk}) + \lambda\delta_{ij}\delta_{kl} \quad (2.62)$$

where the Kronecker delta function is used, $\delta_{ij} = 1$ for $i = j$ and $\delta_{ij} = 0$ for $i \neq j$.

2.5.7 Screw Dislocation

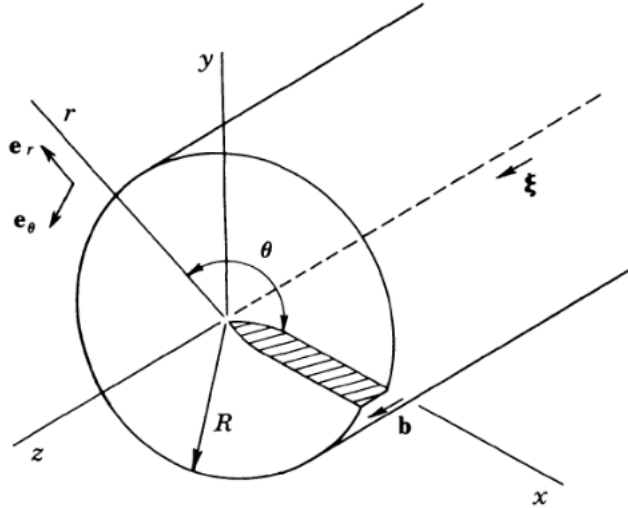


Figure 2.11: Screw dislocation with radius R perpendicular and Burgers vector \mathbf{b} horizontal to the line vector ξ [25]

A pure screw dislocation in a semi-infinite isotropic elastic material is modelled in Fig 2.11. The cylinder has been cut radially along the z -axis and displaced leaving a slip step equal to the magnitude of the Burgers vector $|\mathbf{b}| = b$ parallel to the line of the dislocation ξ . The displacement is in u_z only with $u_x = u_y = 0$. For an isotropic material it can be expected that the displacement in u_z occurs smoothly. The radius is followed, starting at one edge of the discontinuity and ending at the other, along the path perpendicular to \mathbf{b} . Using polar coordinates,

as θ increases from 0 to 2π , u_z increases from 0 to b ,

$$u_z = \frac{b\theta}{2\pi} \quad (2.63)$$

The expression can be represented in the cartesian system as,

$$u_z = \frac{b}{2\pi} \arctan\left(\frac{y}{x}\right) \quad (2.64)$$

From these expressions the strains can be found using (2.35). The non-zero terms are,

$$\begin{aligned} \epsilon_{xz} = \epsilon_{zx} &= -\frac{b}{4\pi} \arctan\left(\frac{y}{x^2 + y^2}\right) = -\frac{b}{4\pi} \frac{\sin \theta}{r} \\ \epsilon_{yz} = \epsilon_{zy} &= \frac{b}{4\pi} \arctan\left(\frac{x}{x^2 + y^2}\right) = \frac{b}{4\pi} \frac{\cos \theta}{r} \end{aligned} \quad (2.65)$$

Using Eq 2.61 and Eq 2.65 the non zero stresses are

$$\begin{aligned} \sigma_{xz} = \sigma_{zx} &= -\frac{\mu b}{2\pi} \frac{y}{x^2 + y^2} = -\frac{\mu b}{2\pi} \frac{\sin \theta}{r} \\ \sigma_{yz} = \sigma_{zy} &= \frac{\mu b}{2\pi} \frac{x}{x^2 + y^2} = \frac{\mu b}{2\pi} \frac{\cos \theta}{r} \end{aligned} \quad (2.66)$$

2.5.8 Edge Dislocation

The isotropic pure edge dislocation is considered for the special case where the dislocation line is straight. The edge dislocation is modelled using a semi-infinite cylinder of elastic material (Fig 2.12). All of the forces are applied perpendicular to the z axis so that the stresses are only functions of x and y independent of z . For this situation solutions for plane stress and strain can be used to describe the dislocation. The method for calculating the stress, strain and displacement of the straight edge dislocation is summarised following the outlines in Hirth and Lothe [25] and Timoshenko [24].

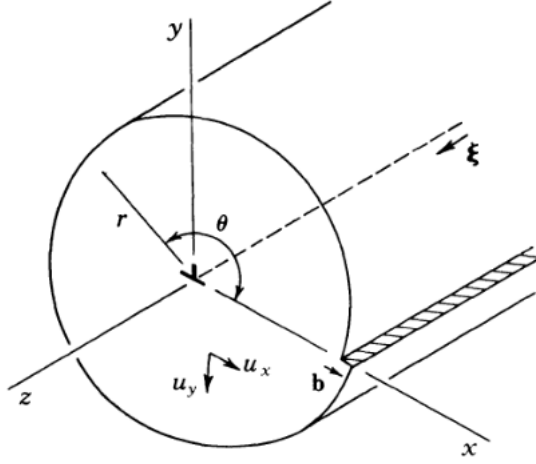


Figure 2.12: Edge dislocation with radius r and Burgers vector \mathbf{b} perpendicular to the line vector ξ [25]

For the case of plane strain the displacement in one direction is zero and there is no dependence on this direction from the remaining displacements. Taking displacement in the z direction to be zero the two remaining displacements u_x and u_y are dependent on x and y

$$\begin{aligned} u_x &= u_x(x, y) & u_y &= u_y(x, y) \\ u_z &= 0 & \frac{\partial}{\partial z} &= 0 \end{aligned} \quad (2.67)$$

The equilibrium equations of elasticity describe the situation when no net forces act on a volume element

$$\frac{\partial \sigma_{ij}}{\partial x_j} + f_i = 0 \quad (2.68)$$

The term f_i is the component of body force per unit volume. This term can be set to zero as body forces are not being considered. Combining Eq 2.67 and Eq 2.68 gives

$$\begin{aligned} \frac{\partial \sigma_{xx}}{\partial x} + \frac{\partial \sigma_{xy}}{\partial y} &= 0 \\ \frac{\partial \sigma_{xy}}{\partial x} + \frac{\partial \sigma_{yy}}{\partial y} &= 0 \end{aligned} \quad (2.69)$$

For the case of plane strain the equations in Eq 2.69 can be solved if the Airy

function ψ can be found where

$$\sigma_{xx} = \frac{\partial^2 \psi}{\partial y^2} \quad \sigma_{yy} = \frac{\partial^2 \psi}{\partial x^2} \quad \sigma_{xy} = -\frac{\partial^2 \psi}{\partial x \partial y} \quad (2.70)$$

The relationship between the three stress components can be expressed using the *relation of compatibility* [24]. This is in general a set of six partial differential equations that assure the displacement u_i is single valued and continuous. For the case of plane strain there is only one equation

$$\frac{\partial^2 \epsilon_{xx}}{\partial y^2} + \frac{\partial^2 \epsilon_{yy}}{\partial x^2} = 2 \frac{\partial^2 \epsilon_{xy}}{\partial x \partial y} \quad (2.71)$$

The inverse of Eqs 2.66 and 2.61

$$\epsilon_{ii} = \frac{1}{E} \sigma_{ii} - \nu (\sigma_{jj} + \sigma_{kk}) \quad \epsilon_{ij} = \frac{1}{2\mu} \sigma_{ij} \quad (2.72)$$

can be used, along with Eqs 2.70 and 2.71 to restate the equation to be solved in terms of Airy functions

$$\frac{\partial^4 \psi}{\partial x^4} + 2 \frac{\partial^4 \psi}{\partial x^2 \partial y^2} + \frac{\partial^4 \psi}{\partial y^4} = 0 \quad (2.73)$$

Using polar coordinates Eq 2.73 becomes

$$\left(\frac{\partial^2}{\partial r^2} + \frac{1}{r} \frac{\partial}{\partial r} + \frac{1}{r^2} \frac{\partial^2}{\partial \theta^2} \right)^2 \psi = 0 \quad (2.74)$$

Equation 2.73 can be restated in the form of a Laplace equation

$$\nabla^2 \phi = \left(\frac{\partial^2}{\partial r^2} + \frac{1}{r} \frac{\partial}{\partial r} + \frac{1}{r^2} \frac{\partial^2}{\partial \theta^2} \right) \phi = 0 \quad (2.75)$$

with the relationship

$$\phi = \nabla^2 \psi \quad (2.76)$$

The Laplace equation is separable and a particular solution is [25]

$$\psi_e = \frac{\beta_1}{2} r \sin(\theta) \ln r \quad (2.77)$$

where β_1 is a constant. This solution characterises the edge dislocation for regions far from the core.

The dislocation is modelled as a half plane with width equal to the Burgers vector inserted into the material. The difference in passing from one side of a slip plane to the other containing the extra material must reflect this. An expression for the Burgers vector can therefore be written as

$$b = - \int_{-\infty}^{\infty} \epsilon_{xx}(x, \eta) - \epsilon_{xx}(x, -\eta) dx \quad (2.78)$$

where η represents a small positive real number. The integral approaches the slip plane from either side depending on the sign of η in Eq 2.78.

Using the particular solution Eq 2.77 the stresses can be calculated using Eq 2.70. The strains related to these stresses can then be expressed using Eqs 2.72. The strains can then be used to find b in Eq 2.78

$$b = - \frac{2\pi(1-\nu)\beta_1}{2\mu} \quad (2.79)$$

This gives the solution to β_1

$$\beta_1 = - \frac{\mu b}{\pi(1-\nu)} \quad (2.80)$$

which can be used to give the explicit term for the stress function

$$\psi_e = - \frac{\mu b y}{4\pi(1-\nu)} \ln(x^2 + y^2) \quad (2.81)$$

The terms for the stresses of the edge dislocation can now be given by Eqs 2.70

$$\begin{aligned}\sigma_{xx} &= -\frac{\mu b}{2\pi(1-\nu)} \frac{y(3x^2 + y^2)}{(x^2 + y^2)^2} \\ \sigma_{yy} &= \frac{\mu b}{2\pi(1-\nu)} \frac{y(x^2 - y^2)}{(x^2 + y^2)^2} \\ \sigma_{xy} &= \frac{\mu b}{2\pi(1-\nu)} \frac{x(x^2 - y^2)}{(x^2 + y^2)^2}\end{aligned}\quad (2.82)$$

The displacements can be found by integrating Eqs 2.35 as described in [24]

$$\begin{aligned}u_x &= \frac{b}{2\pi} \left(\arctan \frac{y}{x} + \frac{xy}{2(1-\nu)(x^2 + y^2)} \right) \\ u_y &= -\frac{b}{2\pi} \left(\frac{1-2\nu}{4(1-\nu)} \ln(x^2 + y^2) + \frac{x^2 - y^2}{4(1-\nu)(x^2 + y^2)} \right)\end{aligned}\quad (2.83)$$

The solutions to the stresses and displacements given above are for the case of edge dislocations in infinite isotropic material. In the integration of u_x in Eq 2.83 the constant of integration is calculated using the conditions $u_x = 0$ at $y = 0$. For u_y the constant of integration is chosen to make the solution symmetric in x and y .

For different dislocation models boundary conditions must be taken into consideration. For example a common model for an edge dislocation is a hollow cylinder with internal radius r_c and external radius R . Boundary conditions at the surfaces must be satisfied such as the condition that no forces can act on a free surface

$$\sigma_{ij}n_j = 0 \quad (2.84)$$

where n_j is the component of normal force to the surface. The solution leading to the calculation of the stress terms etc. when considering the boundary conditions come from additional stress functions. These cancel the fictitious stresses introduced at the surfaces.

2.5.9 Strain energy of the edge dislocation

The energy per unit length is calculated for the model of an infinite cylinder with outer radius R_a and core radius r_0 . The material is cut along the plane $y = 0$ and displaced to form a dislocation. The work done in making this displacement is calculated by

$$\frac{E_{self}}{L} = -\frac{1}{2} \int_{r_0}^{R_a} \sigma_{i2} b_i dx_i \quad (2.85)$$

The solution to Eq 2.85 is [25]

$$\frac{E_{self}}{L} = \frac{\mu b^2}{4\pi(1-\nu)} \ln \frac{R_a}{r_0} \quad (2.86)$$

The above model is commonly adjusted so that the cylinder has a hollow core and a free outer surface. Allowing for the relaxation of the outer and core surfaces results in a lowering of the energy. The expression becomes [25]

$$\frac{E_{self}}{L} = \frac{\mu b^2}{4\pi(1-\nu)} \ln \left(\frac{R_a}{r_0} - 1 \right) \quad (2.87)$$

This energy term describes the self energy of an edge dislocation disregarding the core region. The contribution from this term is always positive. For the case when there are two or more dislocations interacting with one another in a crystal the interaction energy must also be considered.

2.5.10 Interaction energy

A useful equation for the interaction between two parallel straight dislocations has been given by Nabarro [33]

$$\begin{aligned} \frac{E_{12}}{L} = & -\frac{\mu}{2\pi} (\mathbf{b}_1 \cdot \boldsymbol{\xi}) (\mathbf{b}_2 \cdot \boldsymbol{\xi}) \ln \frac{R}{R_a} - \frac{\mu}{2\pi(1-\nu)} [(\mathbf{b}_1 \times \boldsymbol{\xi}) \cdot (\mathbf{b}_2 \times \boldsymbol{\xi})] \ln \frac{R}{R_a} \\ & - \frac{\mu}{2\pi(1-\nu)R^2} [(\mathbf{b}_1 \times \boldsymbol{\xi}) \cdot \mathbf{R}] [(\mathbf{b}_2 \times \boldsymbol{\xi}) \cdot \mathbf{R}] \end{aligned} \quad (2.88)$$

The separation of the two dislocations is given by R . The first term on the right hand side of Eq 2.88 refers to any screw component of the two dislocations. The final two terms refer to the edge components.

For the case of plain strain with straight edge dislocation lines Eq 2.88 can be simplified to

$$\frac{E_{12}}{L} = \frac{\mu b_1 b_2}{2\pi(1-\nu)} \left[\ln \frac{R}{R_a} - \cos^2 \theta \right] \quad (2.89)$$

Where θ is the angle between the dislocations. Unlike the self energy of Eq 2.87, which is always a positive contribution to the total energy, the interaction energy can be positive or negative. The sign of the resulting energy is dependent on the position of the dislocations, represented by the \cos term, and the sign of the Burgers vectors.

2.5.11 Dislocation Loops

The dislocations discussed so far are of the type screw and edge with infinite straight line vectors. In general the dislocation line is not straight. The line cannot terminate in a section of perfect material [25]. It can join another dislocation at a node, conserving the Burgers vector. suitable defect, terminate at the surface of the crystal or be in the form of a dislocation loop.

A dislocation loop is a region of slipped material enclosed within a continuous dislocation line as shown in Fig 2.13. In an otherwise perfect crystal the material outside the dislocation loop will remain perfect.

The loop can move conservatively or shrink or expand by glide in the direction of the Burgers vector. The Burgers vector is invariant at all positions around the loop while the line vector direction changes according to the tangent of a specific point around the loop. This means that the dislocation is of different character around the loop. The dislocation is in general made of a combination of edge and screw character. The Burgers vector component of screw can be calculated as

$$\mathbf{b}_s = (\mathbf{b} \cdot \boldsymbol{\xi}) \boldsymbol{\xi} \quad (2.90)$$

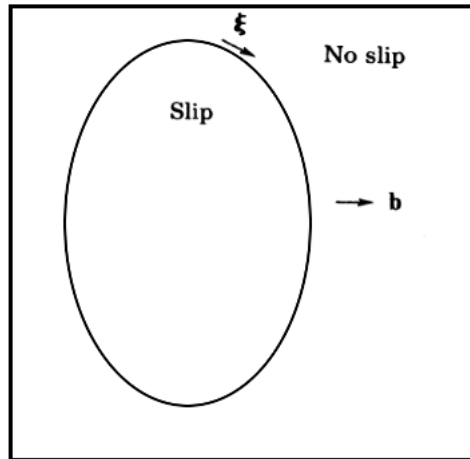


Figure 2.13: A dislocation loop within a crystal

and the edge component as

$$\mathbf{b}_e = \boldsymbol{\xi} \times (\mathbf{b} \times \boldsymbol{\xi}) \quad (2.91)$$

2.5.12 Anisotropy

Graphite is a highly anisotropic material. This can be seen by comparing the stiffness within the graphite layers [46], $C_{11} = 1060 \text{ GPa}$, to that of the stiffness in the direction perpendicular to the layers [46], $C_{33} = 36.5 \text{ GPa}$. For an isotropic crystal these values would be equivalent. To represent dislocations in an anisotropic framework is more complicated than for the isotropic theory.

In 1953 Eshelby *et al.* [47] published a paper outlining a theory for anisotropic elasticity in three dimensions to be applied to dislocation theory. This is known as the classical sextic anisotropic elasticity theory of straight dislocations. The case considered was for stress independent of one Cartesian coordinate. This is the case for straight dislocations where the dislocation line is along the direction of one of the coordinate axes. This work was developed further by Foreman [48] to consider the anisotropic elastic energies of straight dislocations. Further development to the theory has come from Stroh [49], Spence [50], Chou [51], Hirth and Lothe [25] and others. The sextic theory is most useful for cases of high symmetry where simplifications allow for analytical solutions. Teutonico [52] published a paper in

1961 outlining a method for numerical solutions to the sextic theory for the general case of straight dislocations. The technique for finding solutions within the sextic theory is summarised below. The first property considered is the displacement.

2.5.13 Anisotropy: Displacement

Following Eshelby [47] and Hirth and Lothe [25] the axes are oriented so the line of the dislocation is parallel to the z axis. The displacement strains and stresses are independent of the z direction so that $\partial/\partial x_3 \equiv 0$. The equilibrium condition for the stress under plane strain is

$$\frac{\partial \sigma_{i\alpha}}{\partial x_\alpha} = 0 \quad (2.92)$$

Where Greek letters such as α run over 1 and 2 and Roman letters such as i run over 1, 2 and 3. Using the expressions Eq 2.36 and Eq 2.35 the stress $\sigma_{i\alpha}$ can be written as

$$\sigma_{i\alpha} = C_{i\alpha k\beta} \frac{\partial u_k}{\partial x_\beta} \quad (2.93)$$

By substituting Eq 2.93 into Eq 2.92 a partial differential equation can be produced

$$C_{i\alpha k\beta} \frac{\partial^2 u_k}{\partial x_\alpha \partial x_\beta} = 0 \quad (2.94)$$

With summation over the indices α , k and β Eq 2.94 results in three simultaneous equations to be solved. The solutions of the equations give the displacements u_k . The form of the solution to each equation is

$$u_k = A_k f(x_1 + px_2) \quad (2.95)$$

The expression for u_k in Eq 2.95 can be substituted into Eq 2.94. After cancelling the term $\partial^2 f / \partial (x_1 + px_2)^2$ the equations can be summarised as

$$a_{ik} A_k = 0 \quad (2.96)$$

where

$$a_{ik} = C_{i1k1} + (C_{i1k2} + C_{i2k1})p + C_{i2k2}p^2 \quad (2.97)$$

To find non zero solutions to the A_k in Eq 2.95 the determinant of the matrix $\{a_{ik}\}$ must be equal to zero

$$|\{a_{ij}\}| = 0 \quad (2.98)$$

This leads to a sixth order equation in terms of p with six roots p_n with $n = 1, 2, 3, 4, 5, 6$. To satisfy Eq 2.96 a set of values can be found for $A_k(n)$ to correspond with each root p_n . This can be calculated using subdeterminants of $a_{ij}(n)$ as detailed in Hirth and Lothe[25]. Eshelby *et al.* [47] showed that the roots p_n are never real. The roots are always complex conjugates since u_k must be real. This means that only three of the six roots need to be considered p_1, p_2 and p_3 , along with $A_k(1), A_k(2)$ and $A_k(3)$.

The function $f(x_1 + p_n x_2)$ in Eq 2.95 needs to reflect the properties of dislocations with respect to displacement. It must be single valued outside of the dislocation core and discontinuous across the region of dislocation. The function is made of two parts

$$f(x_1 + p_n x_2) = -\frac{D}{2\pi i} \ln(x_1 + p_n x_2) + \sum_{n=-\infty}^{\infty} a_n (x_1 + p_n x_2)^n \quad (2.99)$$

The first, $-\frac{D}{2\pi i} \ln(x_1 + p_n x_2)$, deals with the discontinuity arising from the dislocation and the second, $a_n (x_1 + p_n x_2)^n$ summed over $n = -\infty \dots \infty$, is a power series that does not contribute to the discontinuity. $D(n)$ is related to the components of the Burgers vector b_n by [25]

$$Re \left(\sum_{n=1}^3 \pm A_k(n) D(n) \right) = b_k \quad (2.100)$$

for $k = 1, 2, 3$. The plus sign is used when the imaginary part of p is positive and minus when negative. Using Eq 2.100 accompanied with the requirement that

there be no net force on the dislocation core

$$\oint (\sigma_{i1} dx_2 - \sigma_{i2} dx_1) = 0 \quad (2.101)$$

allows $D(n)$ to be solved. The details are outlined in Hirth and Lothe [25].

The expression for u_k can now be written

$$u_k = \text{Re} \left(\frac{-1}{2\pi i} \sum_{n=1}^3 A_k(n) D(n) \ln(x_1 + p_n x_2) \right) \quad (2.102)$$

2.5.14 Anisotropic displacement in hexagonal graphite

For the case of displacements in the x and y directions being independent of the z direction the sixth order polynomial in p is reduced to the fourth order. The matrices are reduced from 3×3 to 2×2 . For the z direction the polynomial is second order and the matrices 1×1 . This is identical to having solutions to the edge and screw components independent of one another.

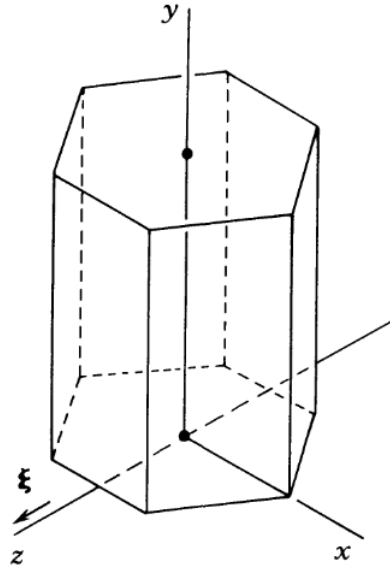


Figure 2.14: Coordinate system for hexagonal graphite with line direction ξ parallel to z

The coordinate system for hexagonal graphite with the line direction ξ parallel with the $-z$ direction is shown in Fig 2.14. In this geometry the basal plane is xz . The elastic constants must be rotated to align with this coordinate system

relative to the standard coordinate directions with the basal plane xy . Applying a rotation of $\pi/2$ about the x axis to the elastic constant tensor using Eq 2.33 and representing as a 6×6 matrix the elastic constants of Eq 2.50 become

$$\{C\} = \begin{bmatrix} C'_{11} & C'_{12} & C'_{13} & 0 & 0 & 0 \\ C'_{12} & C'_{22} & C'_{12} & 0 & 0 & 0 \\ C'_{13} & C'_{12} & C'_{11} & 0 & 0 & 0 \\ 0 & 0 & 0 & C'_{44} & 0 & 0 \\ 0 & 0 & 0 & 0 & C'_{55} & 0 \\ 0 & 0 & 0 & 0 & 0 & C'_{44} \end{bmatrix} \quad (2.103)$$

The values of the elastic constants for hexagonal graphite under standard orientation are [46]

$$C_{11} = 1060GPa, \quad C_{12} = 180GPa, \quad C_{13} = 7.9GPa, \quad C_{33} = 36.5GPa, \quad C_{44} = 5.05GPa \quad (2.104)$$

The rotated values of the elastic constants are related to the standard orientation as follows

$$C'_{11} = C_{11}, \quad C'_{12} = C_{13}, \quad C'_{13} = C_{12}, \quad C'_{44} = C_{44}, \quad C'_{22} = C_{33} \quad (2.105)$$

A term \bar{C}'_{11} is also used where

$$\bar{C}'_{11} = (C'_{11}C'_{22})^{1/2} \quad (2.106)$$

The determinant of matrix $\{a_{ij}\}$ in Eq 2.98 becomes

$$|\{a_{ij}\}| = \begin{vmatrix} C'_{11} + C'_{44}p^2 & (C'_{12} + C'_{44})p & 0 \\ (C'_{12} + C'_{44})p & C'_{44} + C'_{22}p^2 & 0 \\ 0 & 0 & C'_{55} + C'_{44}p^2 \end{vmatrix} \quad (2.107)$$

The subdeterminant relating to the edge dislocation is

$$C'_{22}C'_{44}p^4 + (C'_{11}C'_{22} - 2C'_{12}C'_{44} - C'^2_{12})p^2 + C'_{11}C'_{44} = 0 \quad (2.108)$$

The solutions to the roots of Eq 2.108 are of the form [25]

$$p_2 = \lambda e^{i\phi} \quad p_5 = \lambda e^{-i\phi} \quad p_3 = -\lambda e^{i\phi} \quad p_6 = -\lambda e^{-i\phi} \quad (2.109)$$

with the solutions

$$\lambda = \left(\frac{C'_{11}}{C'_{22}} \right)^{1/4} \quad (2.110)$$

and

$$\phi = \frac{1}{2} \cos^{-1} \frac{C'^2_{12} + 2C'_{12}C'_{44} - C'^2_{11}}{2\bar{C}'_{11}C'_{44}} \quad (2.111)$$

For the case of λ and ϕ being real p_2 and p_3 can be chosen as the fundamentally different roots with their respective conjugates p_5 and p_6 respectively. The non zero results from Eq 2.96 for this case are

$$\begin{aligned} A_1(2) &= 1 & A_2(2) &= -\lambda \frac{C'_{44}e^{i\phi} + \bar{C}'_{11}e^{-i\phi}}{C'_{12} + C'_{44}} = A \\ A_1(3) &= 1 & A_2(3) &= -A_2(2) = -A \end{aligned} \quad (2.112)$$

$$\begin{aligned} u_x &= -\frac{b_x}{4\pi} \left(\tan^{-1} \frac{2xy\lambda \sin \phi}{x^2 - \lambda^2 y^2} + \frac{\bar{c}'_{11} - c'_{12}}{2\bar{c}'_{11}c'_{44} \sin 2\phi} \ln \frac{q}{t} \right) \\ &\quad - \frac{b_y}{4\pi \lambda \bar{c}'_{11} \sin 2\phi} \left[(\bar{c}'_{11} - c'_{12}) \cos \phi \ln qt \right. \\ &\quad \left. - (\bar{c}'_{11} + c'_{12}) \sin \phi \tan^{-1} \frac{x^2 \sin 2\phi}{\lambda^2 y^2 - x^2 \cos 2\phi} \right] \end{aligned} \quad (2.113)$$

The resulting expressions for the displacements in x and y are

$$\begin{aligned}
u_y = & \frac{\lambda b_x}{4\pi \bar{c}'_{11} \sin 2\phi} \left[(\bar{c}'_{11} - c'_{12}) \cos \phi \ln qt \right. \\
& \left. - (\bar{c}'_{11} + c'_{12}) \sin \phi \tan^{-1} \frac{y^2 \lambda^2 \sin 2\phi}{x^2 - \lambda^2 y^2 \cos 2\phi} \right] \\
& - \frac{b_y}{4\pi} \left(\tan^{-1} \frac{2xy\lambda \sin \phi}{x^2 - \lambda^2 y^2} - \frac{\bar{c}'_{11} - c'_{12}}{2\bar{c}'_{11} c'_{44} \sin 2\phi} \ln \frac{q}{t} \right) \quad (2.114)
\end{aligned}$$

2.5.15 Solutions for complex ϕ

For the case of ϕ in Eq 2.110 being imaginary the particular roots of the polynomial resulting from Eq 2.107 must be chosen differently than for real ϕ . This situation has been considered by Malen [53].

For hexagonal graphite, using the elastic constant values in Eq 2.104, the value of ϕ is

$$\phi = \frac{1}{2} \cos^{-1} \frac{C'_{12}{}^2 + 2C'_{12}C'_{44} - C'_{11}{}^2}{2\bar{C}'_{11}C'_{44}} = \left(\frac{\pi}{2} - 3.51i \right) \quad (2.115)$$

So ϕ is of the form $\frac{\pi}{2} - \delta i$. This leads to the expressions

$$\begin{aligned}
\cos 2\phi &= -\cosh 2\delta & \sin 2\phi &= i \sinh 2\delta \\
\cos \phi &= i \sinh \delta & \sin \phi &= \cosh \delta
\end{aligned} \quad (2.116)$$

For this case p_2 and p_3 cannot be chosen as the fundamental roots. The pairs of complex conjugate roots are now (p_2, p_3) and (p_6, p_5) with p_2 and p_6 chosen as the fundamental roots. With these choice of roots Malen [53] reports that the solutions for the case of real ϕ are equivalent to those shown above with respect to the calculation of displacement and stress.

To get the solutions to the displacements for complex angle ϕ involves a different set of intermediate steps to that outlined above. However substituting

the expressions in Eq 2.116 along with the following substitutions

$$\begin{aligned}
q^2 &= x^2 + y^2\lambda^2 + i2xy\lambda \sinh \delta \\
t^2 &= x^2 + y^2\lambda^2 - i2xy\lambda \sinh \delta \\
\ln \frac{q}{t} &= i \tan^{-1} \frac{2xy\lambda \sinh \delta}{x^2 + \lambda^2 y^2} \\
\tan^{-1} ia &= \frac{1}{2i} \ln \frac{1-a}{1+a}
\end{aligned} \tag{2.117}$$

into equations 2.113 and 2.114 give equivalent results [53] for u_x and u_y

$$\begin{aligned}
u_x &= -\frac{b_x}{4\pi} \left(\tan^{-1} \frac{2xy\lambda \cosh \delta}{x^2 - \lambda^2 y^2} + \frac{(c_{11}c_{33}) - c_{13}^2}{2(c_{11}c_{33})^{1/2} c_{44} \sinh 2\delta} \tan^{-1} \frac{2xy\lambda \sinh \delta}{x^2 + \lambda^2 y^2} \right) \\
&\quad - \frac{b_y}{4\pi\lambda (c_{11}c_{33})^{1/2} \sinh 2\delta} \left[\left((c_{11}c_{33})^{1/2} - c_{13} \right) \sinh \delta \ln \left[(x^2 + \lambda^2 y^2)^2 \right. \right. \\
&\quad \left. \left. + 4x^2 y^2 \lambda^2 \sinh^2 \delta \right]^{1/2} \right. \\
&\quad \left. + \left((c_{11}c_{33})^{1/2} + c_{13} \right) \cosh \delta \frac{1}{2} \ln \frac{1 - (x^2 \sinh 2\delta) / (\lambda^2 y^2 + x^2 \cosh 2\delta)}{1 + (x^2 \sinh 2\delta) / (\lambda^2 y^2 + x^2 \cosh 2\delta)} \right]
\end{aligned} \tag{2.118}$$

$$\begin{aligned}
u_y &= \frac{\lambda b_x}{4\pi (c_{11}c_{33})^{1/2} \sinh 2\delta} \left[\left((c_{11}c_{33})^{1/2} - c_{13} \right) \sinh \delta \ln \left[(x^2 + \lambda^2 y^2)^2 \right. \right. \\
&\quad \left. \left. + 4x^2 y^2 \lambda^2 \sinh^2 \delta \right]^{1/2} \right. \\
&\quad \left. + \left((c_{11}c_{33})^{1/2} + c_{13} \right) \cosh \delta \frac{1}{2} \ln \frac{1 - (y^2 \lambda^2 \sinh 2\delta) / (x^2 + \lambda^2 y^2 \cosh 2\delta)}{1 + (y^2 \lambda^2 \sinh 2\delta) / (x^2 + \lambda^2 y^2 \cosh 2\delta)} \right] \\
&\quad - \frac{b_y}{4\pi} \left(\tan^{-1} \frac{2xy\lambda \cosh \delta}{x^2 - \lambda^2 y^2} - \frac{(c_{11}c_{33}) - c_{13}^2}{2(c_{11}c_{33})^{1/2} c_{44} \sinh 2\delta} \tan^{-1} \frac{2xy\lambda \sinh \delta}{x^2 + \lambda^2 y^2} \right)
\end{aligned} \tag{2.119}$$

2.5.16 Anisotropy: Stress and Energy

The stresses can be calculated from Eqs 2.35 and 2.36 with Eq 2.102.

The energy terms for isotropic theory can be used in the anisotropic theory. This can be achieved by exchanging the term $\frac{\mu}{1-\nu}$ of Eq 2.87 with the relevant

energy coefficient K for edge dislocation energies. For screw dislocations the terms in μ are exchanged for the appropriate energy coefficient. This results in the anisotropic self energy for an edge dislocation of

$$\frac{E}{L} = \frac{Kb^2}{4\pi} \ln \left(\frac{R}{r_0} - 1 \right) \quad (2.120)$$

With K referring to the energy coefficient relating to the dislocation.

The energy coefficient itself is defined by

$$Kb^2 = b_i Im \left[\sum_{n=1}^3 B_{i2k} A_k(n) D(n) \right] \quad (2.121)$$

It can be noted that the greatest effect of the anisotropic theory on the energy term in Eq 2.120 arises from the energy factor.

The energy factor terms for the plane strain edge dislocation can be solved exactly for b_x and b_y using equation 2.121

$$K_{e_x} = (\bar{c}'_{11} + c'_{12}) \left[\frac{c'_{44} (\bar{c}'_{11} - c'_{12})}{(\bar{c}'_{11} + c'_{12} + 2c'_{44}) c'_{22}} \right]^{1/2} \quad (2.122)$$

$$K_{e_y} = (\bar{c}'_{11} + c'_{12}) \left[\frac{c'_{44} (\bar{c}'_{11} - c'_{12})}{(\bar{c}'_{11} + c'_{12} + 2c'_{44}) c'_{11}} \right]^{1/2} \quad (2.123)$$

2.5.17 Interaction energy

In the same way that the energy coefficients were introduced to the self energy expression Eq 2.120 the expressions for the isotropic interaction energy can be altered to give anisotropic expressions. Equation 2.89 becomes

$$\frac{E_{12}}{L} = \frac{Kb_1 b_2}{2\pi} \left[\ln \frac{R}{R_a} - \cos^2 \theta \right] \quad (2.124)$$

Where the energy factor K has been substituted into the expression.

Chapter 3

Elastic Properties of Graphite

3.1 Elastic Constants

3.1.1 Introduction

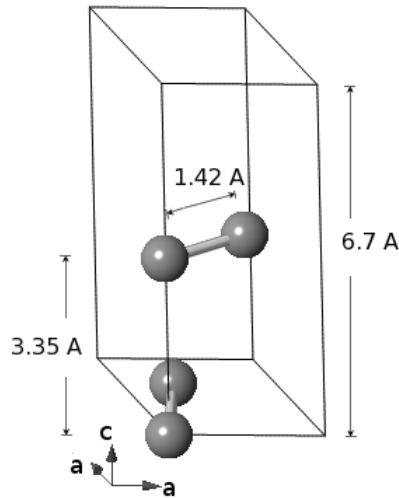


Figure 3.1: Hexagonal graphite primitive unit cell

Graphite is formed of layers of carbon atoms arranged in hexagonal networks. Carbon has the atomic number 6 and electronic structure $1s^2 2s^2 2p^2$. The strong bonding between atoms within the layers comes from the overlap of sp^2 hybridised orbitals forming σ bonds between nearest neighbour atoms. The weaker bonding between layers comes, in part, from the overlap of p_z orbitals [54]. London dispersion forces also play a role in the interlayer bonding.

The lowest energy stacking of the layers in perfect graphite is AB . This was the structure determined by Bernal [55] in 1924. It is usually referred to as Bernal graphite or hexagonal graphite. The primitive unit cell is shown in Fig 3.1.

This describes a system of layering with two alternating layer geometries. A layer with one type of geometry is labelled A . This is sandwiched between layers of the alternate geometry B and vice versa. Alpha atoms in A and B layers are directly above and below one another (see Fig 3.2 (a)). Beta atoms are situated directly above and below the centres of the hexagon formations in adjacent layers.

Two other graphite allotropes have layering systems with AA and ABC stacking [56]. ABC stacked graphite is known as rhombohedral graphite. This [57]

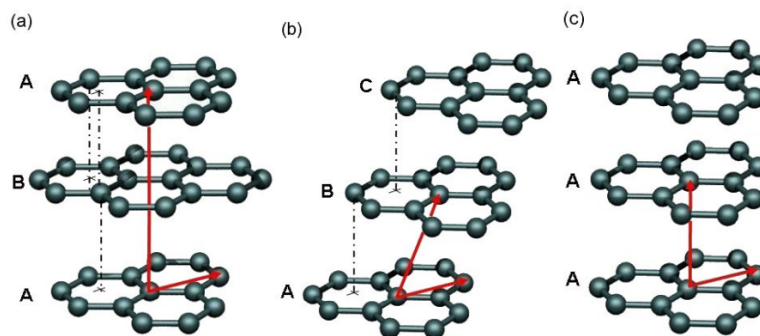


Figure 3.2: The stacking formation of three allotropes of graphite [57] (a) Hexagonal (Bernal) AB stacking (b) Rhombohedral ABC stacking (c) AA stacking

stacking has recently been found in isolated rhombohedral crystallites within graphite blocks during a HRTEM study [58].

AA is a high energy stacking of the graphite layers. This arrangement can be favourable for graphite intercalated with other species. For example stage-1 bromine intercalated graphite [59].

Another type of layer stacking is also found in nature. It is common to find a situation where the graphite layers are randomly oriented having no regular stacking pattern. Each layer can be translated and/or rotated with respect to its surrounding layers. This leads to slightly differing interlayer separations found

throughout the system. This is known as turbostratic stacking.

Natural single crystal graphite flakes are sometimes used in experimental work although they commonly contain a high density of defects. It is often preferable to use a high purity treated graphite. Highly Oriented Pyrolytic Graphite (HOPG) is prepared by the pyrolysis of hydrocarbons at high temperature, above $2000^{\circ}C$. The resulting pyrolytic carbon is subsequently heat treated to higher temperature $3000^{\circ}C$ improving its crystalline order. The material has a very well aligned c axis, typically within a few tenths of a degree. The resulting material has the thermal and mechanical properties similar to a perfect crystal of graphite although it is still polycrystalline.

The second and third order elastic constants of AB stacked graphite are calculated in Sec 3.1.4. The AIMPRO code uses DFT with LDA. The results are compared to other theoretical results and to experimental results.

Blakslee *et al.* [60] published a paper in 1970 giving experimental values for the five elastic constants of HOPG. These results were from experiments using ultrasonic, sonic resonance and static test methods. Two of the results, C_{13} and C_{44} , have since been revised as reviewed by Cousins and Heggie [46].

Highly mobile basal dislocations were believed to have affected the measurement of C_{44} using transverse ultrasonic wave experiments. Experiments of this type have been carried out by Soule and Nezbeda [61], Blakslee *et al.* [60] and Seldin and Nezbeda [62]. The values obtained were very low, between 0.25 and 1.2 GPa . For the case of an ideal perfect crystal these dislocations would not be present. With light neutron irradiation Seldin and Nezbeda [62] reported a higher value of $C_{44} \geq 4.0 GPa$. It is believed that the dislocations were pinned as a result of the irradiation.

Grimsditch [63, 64] used Brillouin scattering from surface waves to calculate $C_{44} = 5.05 \pm 0.35 GPa$. A neutron scattering study from Nicklow *et al.* [65] reports a value of $C_{44} = 4.6 \pm 0.2 GPa$. It is believed that a realistic value is amongst the higher measurements reported for C_{44} . Kelly's review [66] stated that the higher

results were consistent with specific heat data.

The value of $C_{13} = 15 \pm 5 \text{ GPa}$ calculated by Blackslee *et al.* [60] was called into question by Zhao and Spain [67]. They proffered a correction using their calculated linear modulus B_a combined with the values of C_{11} and C_{12} . This led to a value of $C_{13} = 22 \pm 2 \text{ GPa}$. However this correction was shown to be in error by Cousins and Heggie [46]. The planar modulus had been used in place of the linear modulus. Following the correction with the linear modulus value in place they reported a corrected value of $C_{13} = 7.9 \pm 3.5 \text{ GPa}$.

An inelastic x-ray scattering study was carried out in 2007 by Bosak and Krisch [68]. Kish graphite samples made up of large single grains, $\sim 0.8 \text{ mm}$ in the lateral direction and $\sim 0.1 \text{ mm}$ in the c direction, were used in the study. Small grain regions of the crystal could be examined because of the small beam dimension. The lattice parameters were reported to be very close to that of previous neutron diffraction results [69].

In 2008 Michel and Verbeck [70] used a force constant model to calculate the elastic properties of graphite. The model was based on a fifth-nearest-neighbour force-constant model fitted to inelastic x-ray scattering data by Mohr *et al.* [71]. Born's long wave method [20] was used to calculate some elastic properties of graphene. The model was subsequently extended to consider graphite. The interlayer forces were modelled using Lennard-Jones type potentials.

The most accurate *ab initio* theoretical calculations of the mechanical properties of graphite come from DFT calculations. Theoretical calculations of the elastic constants of hexagonal graphite have been undertaken by Mounet and Marzari [16] using the ν -ESPRESSO package. DFT was used with plane wave basis sets and ultra soft pseudo potentials. The exchange correlation functional used was the Perdew-Burke-Ernzerhof (PBE) generalized gradient approximation (GGA). The calculations for the elastic constants were also repeated using LDA.

The Mounet and Marzari calculations were based on the total energy of the system under various strains of lattice parameters. The lattice parameters used

for the calculations were taken from the optimised unit cells using GGA and LDA. The GGA calculations were repeated using experimental a and c lattice parameter values. A large difference was seen between the GGA calculated interlayer parameter when compared to the experimental value. The use of experimental values for GGA calculations was shown to give good agreement with experimental elastic constants.

Theoretical studies using the AIMPRO code were undertaken by Savini *et al.* [72, 73, 74]. In the 2011 paper [72] the ABINIT code [75] was also used. The elastic constant results calculated using the two different packages were reported to agree within 3%. In both cases DFT with LDA were used along with norm conserving pseudopotentials. A cut off energy of 150 *Ryd* was given for the ABINIT calculations. The k point mesh used in the ABINIT calculations was reported to be $32 \times 32 \times 16$. The basis set functions were expanded using plane waves.

For the AIMPRO calculations the charge density represented by a plane wave basis was used with an energy cutoff of 600 *Ryd* for the elastic constant calculations and up to 2000 *Ryd* for the optimisation of the unit cell. The k point mesh was reported as $16 \times 16 \times 6$ with those used for optimisation up to $128 \times 128 \times 16$. The basis set functions were expanded using gaussian type orbitals. The basis set used for the elastic constant calculations was reported to be pdpp with pdddp used for the optimisation.

The third order elastic constants of hexagonal graphite were studied by Savini [73] using DFT with LDA. Another study was carried out by Cousins and Heggie [46]. They applied a fit to a modified anharmonic Keating model to calculate up to third order elastic constants. The model used parameters from fits to the second order elastic constants, optic mode frequencies and pressure derivatives of the second order elastic constants.

There are currently no direct third order experimental measurements available for the third order elastic constants of hexagonal graphite. This may well be because of the difficulty involved in taking measurements. The second order

elastic constants are isotropic in the basal plane making measurements much more straight forward because of the wide availability of highly aligned c-axis samples. This is not the case in the third order.

3.1.2 Optimisation

Before calculating the energy density of hexagonal graphite the unit cell must be optimised as outlined in section 2.1.2.7. The AIMPRO code was used for all calculations with DFT using the LDA with the exchange-correlation functional as parametrized by Perdew and Wang [76]. The norm conserving pseudopotentials used were based on the Hartwigsen-Goedecker-Hutter scheme [11]. A plane wave basis represented the charge density in reciprocal space. The Brillouin zone integrations were performed with a Monkhorst-Pack scheme.

For the optimisation calculations of hexagonal graphite a pddd basis set of Gaussian orbital functions was used. A pdpp basis set was also tested. This led to a slightly smaller interlayer separation with an accompanying increase in C_{33} value when compared to the pddd basis set. It was believed that the fuller pddd basis set would give the more useful result.

The integrations over the Brillouin zone were carried out with a Monkhorst-Pack [14] scheme and a k-point mesh of $72 \times 72 \times 26$. Various other k-point mesh values were tested. Some variation in the energy and geometry results from optimising the unit cell were seen when using lower combinations of values of k-point mesh. The results were seen to be well converged at $72 \times 72 \times 26$.

The unit cell used in the AIMPRO calculations (see Fig 3.1) is made up of the hexagonal lattice vectors a , b , c

$$\begin{pmatrix} a \\ b \\ c \end{pmatrix} = \begin{pmatrix} \frac{1}{2}a_0 & -\frac{\sqrt{3}}{2}a_0 & 0 \\ \frac{1}{2}a_0 & \frac{\sqrt{3}}{2}a_0 & 0 \\ 0 & 0 & c_0 \end{pmatrix} \quad (3.1)$$

The lattice parameters and energy are optimised to a satisfactory level of convergence.

Various parameters can be adjusted between runs of the AIMPRO code by altering input data files, known as “dat files”. A full description of the parameters that may be altered is available on the AIMPRO website [77].

When the unit cell is optimised the lattice and subattices are unstrained. The lowest energy lattice parameter magnitudes, a_0 and c_0 in the case of graphite, are found. Using the parameters described the values are shown in Table 3.1.

	a_0 (Å)	c_0 (Å)
Present Work	2.444	6.641
Experimental(295K)[67]	2.462 ± 0.002	6.707 ± 0.001

Table 3.1: Lattice Parameters of Hexagonal Graphite

As expected for DFT with LDA calculations the intralayer parameter a_0 is very close to experiment. The interlayer parameter c_0 is also seen to be close to the experimental value. It is likely that the interlayer separation will be slightly lowered by the London dispersion forces missing from the DFT. Also, there will be a slight expansion to both terms if the effects of temperature are taken into consideration; the LDA calculations do not account for temperature so can be considered zero temperature results.

3.1.3 Elastic Constants of Graphite

As noted in Chapter 2.4.7 there are five independent second order and 10 third order elastic constants required to describe graphite. Using the symmetry relationships shown in Table 2.1 and Eqn 2.45 the elastic strain energy per unit volume in

terms of the second and third order elastic constants can be written as

$$\begin{aligned}
w &= \frac{1}{2}C_{11}(\epsilon_1^2 + \epsilon_2^2 + \frac{1}{2}\epsilon_6^2) + \frac{1}{2}C_{33}\epsilon_3^2 + C_{12}(\epsilon_1\epsilon_2 - \frac{1}{4}\epsilon_6^2) + C_{13}(\epsilon_1\epsilon_3 + \epsilon_2\epsilon_3) + \frac{1}{2}C_{44}(\epsilon_4^2 + \epsilon_5^2) \\
&+ \frac{1}{6}C_{111}(\epsilon_1^3 + 3\epsilon_1^2\epsilon_2 + 3\epsilon_1\epsilon_2^2 + \epsilon_2^3) + \frac{1}{6}C_{333}\epsilon_3^3 + \frac{1}{2}C_{113}(\epsilon_1^2\epsilon_3 + 2\epsilon_1\epsilon_2\epsilon_3 + \epsilon_2^2\epsilon_3) \\
&+ \frac{1}{2}C_{133}(\epsilon_1\epsilon_3^2 + \epsilon_2\epsilon_3^2) + \frac{1}{2}C_{144}(\epsilon_1\epsilon_4^2 + \epsilon_2\epsilon_5^2 - \epsilon_4\epsilon_5\epsilon_6) + \frac{1}{2}C_{244}(\epsilon_2\epsilon_4^2 + \epsilon_1\epsilon_5^2 + \epsilon_4\epsilon_5\epsilon_6) \\
&+ \frac{1}{2}C_{344}(\epsilon_3\epsilon_4^2 + \epsilon_4\epsilon_5^2) + \frac{1}{6}C_{166}(3\epsilon_1\epsilon_6^2 - 3\epsilon_1^2\epsilon_2 - 6\epsilon_1\epsilon_2^2 + \epsilon_2^3) \\
&+ \frac{1}{6}C_{266}(3\epsilon_2\epsilon_6^2 - 9\epsilon_1^2\epsilon_2 - 6\epsilon_1\epsilon_2^2 - \epsilon_2^3) + \frac{1}{2}C_{366}(\epsilon_3\epsilon_6^2 - 4\epsilon_1\epsilon_2\epsilon_3)
\end{aligned} \tag{3.2}$$

The strain components in Eqn 3.2 are those of the 6×1 strain matrix shown in Eqn 2.40.

Equally spaced increments of strain are applied to the optimised unstrained lattice in order to extract the various elastic constants. A total energy is calculated for each geometry. The energy as a function of strain is then fitted to a least squares fit polynomial. This fitting technique is equivalent to taking partial differentials of the energy with respect to the strain or strains applied in the energy calculation. The second and third order elastic constants are then compared to the similar coefficients of the polynomial.

Depending on the strain applied to the lattice for the energy calculation, a combination of elastic constant values may make up the equivalent second or third order polynomial in the fit. A single strain or a combination of two or three are used as required. The strains used and the make up of the resulting energies calculated are summarised in Table 3.2.

To find the contributions to the internal elasticity, represented by Δ_{ij} and Δ_{ijk} as listed in Table 2.2, involves two different types of energy calculation. The energy of the lattice is calculated with strains applied equally to the lattice and sublattices. The elastic constants calculated in this way are the partial elastic constants, C_{ij}^0 and C_{ijk}^0 . The calculation is then rerun allowing the sublattice to optimise to the geometry with the lowest energy. This calculation results in the total elastic constants made up of the partial and internal contributions. The

ϵ_i	ϵ_j	ϵ_k	Energy density term
1			$w = \frac{1}{2}C_{11}\epsilon_1^2 + \frac{1}{6}C_{111}\epsilon_1^3$
1	2		$w = C_{11}(\epsilon_1^2 + \epsilon_2^2) + C_{12}\epsilon_1\epsilon_2 + \frac{1}{6}C_{111}\epsilon_1^3 + \frac{1}{6}C_{222}\epsilon_2^3 + \frac{1}{2}C_{112}\epsilon_1^2\epsilon_2 + \frac{1}{2}C_{122}\epsilon_1\epsilon_2^2$
1	3		$w = \frac{1}{2}C_{11}\epsilon_1^2 + C_{13}\epsilon_1\epsilon_3 + \frac{1}{2}C_{33}\epsilon_3^2 + \frac{1}{6}C_{111}\epsilon_1^3 + \frac{1}{6}C_{333}\epsilon_3^3 + \frac{1}{2}C_{113}\epsilon_1^2\epsilon_3 + \frac{1}{2}C_{133}\epsilon_1\epsilon_3^2$
1	4		$w = \frac{1}{2}C_{11}\epsilon_1^2 + \frac{1}{2}C_{44}\epsilon_4^2 + \frac{1}{6}C_{111}\epsilon_1^3 + \frac{1}{2}C_{144}\epsilon_1\epsilon_4^2$
1	6		$w = \frac{1}{4}C_{11}(2\epsilon_1^2 + \epsilon_6^2) + \frac{1}{6}C_{111}\epsilon_1^3 + \frac{1}{2}C_{166}\epsilon_1\epsilon_6^2$
1	2	3	$w = C_{11}(\epsilon_1^2 + \epsilon_2^2) + C_{12}\epsilon_1\epsilon_2 + C_{13}\epsilon_1\epsilon_3 + \frac{1}{2}C_{33}\epsilon_3^2 + \frac{1}{6}C_{111}\epsilon_1^3 + \frac{1}{6}C_{222}\epsilon_2^3 + \frac{1}{6}C_{333}\epsilon_3^3 + \frac{1}{2}C_{112}\epsilon_1^2\epsilon_2 + \frac{1}{2}C_{122}\epsilon_1\epsilon_2^2 + \frac{1}{2}C_{113}\epsilon_1^2\epsilon_3 + \frac{1}{2}C_{133}\epsilon_1\epsilon_3^2 + C_{123}\epsilon_1\epsilon_2\epsilon_3$
2	4		$w = \frac{1}{2}C_{11}\epsilon_2^2 + \frac{1}{2}C_{44}\epsilon_4^2 + \frac{1}{6}C_{222}\epsilon_2^3 + \frac{1}{2}C_{244}\epsilon_2\epsilon_4^2$
2	6		$w = \frac{1}{4}C_{11}(2\epsilon_2^2 + \epsilon_6^2) + \frac{1}{6}C_{222}\epsilon_2^3 + \frac{1}{2}C_{266}\epsilon_2\epsilon_6^2$
3			$w = C_{33}\epsilon_3^2 + \frac{1}{6}C_{333}\epsilon_3^3$
3	4		$w = \frac{1}{2}C_{33}\epsilon_3^2 + \frac{1}{2}C_{44}\epsilon_4^2 + \frac{1}{6}C_{333}\epsilon_3^3 + \frac{1}{2}C_{344}\epsilon_3\epsilon_4^2$
3	6		$w = \frac{1}{2}C_{33}\epsilon_3^2 + \frac{1}{4}(C_{11} - C_{12})\epsilon_6^2 + \frac{1}{6}C_{333}\epsilon_3^3 + \frac{1}{2}C_{366}\epsilon_3\epsilon_6^2$
4			$w = C_{44}\epsilon_4^2$

Table 3.2: Combinations of second and third order elastic constants for various strains

relationship between the total, partial and inner elastic constants is shown in Eq.2.56.

The plot shown in Fig 3.3 displays the energy density points used to calculate the total elastic constants C_{11} and C_{111} . The energy for the lattice at each strain, $\epsilon_1 = \{ -0.008, -0.006, -0.004, -0.002, 0.000, 0.002, 0.004, 0.006, 0.008 \}$, along the lower axis has been divided by the volume of the unstrained lattice. Once the polynomial has been fitted using a least squares fit algorithm, such as that offered by the open source Octave software, the results are shown simply by rearranging the energy equation as listed in Table 3.2. For the example of strain ϵ_1 this gives

$$C_{11} = 2 \frac{\partial^2 w}{\partial \epsilon_1^2} \quad (3.3)$$

and

$$C_{111} = 6 \frac{\partial^3 w}{\partial \epsilon_1^3} \quad (3.4)$$

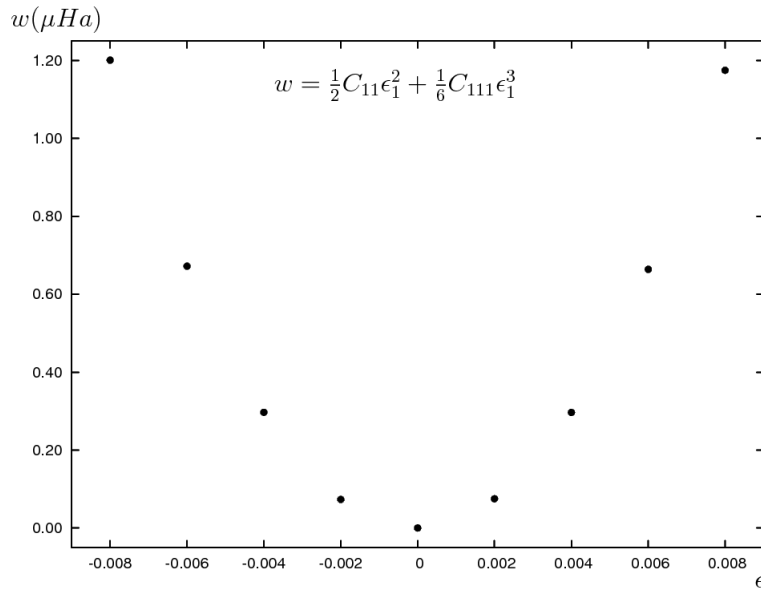


Figure 3.3: Energy per unit cell volume vs strain

Calculations are similar for the remaining terms.

3.1.4 Results

The results for the calculated second order elastic constants are shown in Table 3.3. The results are compared to various experimental and theoretical results. The values are in general agreement with those of the Cousins and Heggie review [46].

The value of C_{13} is the most obvious difference as it is negative implying a negative poisson ratio between the c axis and a direction in the ab plane. This negative result for C_{13} is the case for the other two DFT studies. As can be seen in Table 3.2 the energy per volume term from which C_{13} is calculated contains three second order terms

$$w = \frac{1}{2}C_{11}\epsilon_1^2 + C_{13}\epsilon_1\epsilon_3 + \frac{1}{2}C_{33}\epsilon_3^2 \quad (3.5)$$

The difference of large values may be responsible for the negative value.

Another issue that may be responsible is the interlayer interactions as represented in DFT. This is most obvious in GGA calculations such as those by Mounet and Marzari [16] where the c parameter is 8.94 Å compared to 6.68 Å for LDA. There

is a difference of $\sim 22\%$ between LDA and experimental results for C_{33} , the elastic constant recording the measure of interlayer stiffness. This difference is believed to arise from van der Waals dispersion forces that are missing from the DFT.

Elastic Constant	Current pddd DFT/LDA	Savini ^(a) DFT/LDA	Michel/ Verbeck ^(b)	Bosak ^(c)	Mounet / Marzari ^(d)	Cousins ^(e) exp review
C_{11}	1092	1109	1211	1109	1118	$1060 \pm 20^{(f)}$
C_{11}^0	1119					1064
Δ_{11}	-27					-3.85
C_{12}	202	175	276	139	235	$180 \pm 20^{(f)}$
C_{12}^0	175					176
Δ_{12}	27					3.85
C_{13}	-2.9	-2.5	0.6	0	-2.8	7.9 ± 3.5
C_{33}	30	29	36.8	38.7	29	$36.5 \pm 1.0^{(f)}$
C_{44}	4.7	4.5	4.2	4.95	4.5	$5.05 \pm 0.35^{(g)}$

Table 3.3: Hexagonal Graphite: 2nd order elastic constants [GPa] (C_{xx} denotes total elastic constant, C_{xx}^0 partial elastic constant, Δ_{xx} internal contribution to the elastic constant)

- (a) Savini *et al.* [72]
- (b) Michel and Verbeck [70]
- (c) Bosak *et al.* [68]
- (d) Mounet and Marzari [16]
- (e) Cousins and Heggie [46]
- (f) Blackslee *et al.* [60]
- (g) Grimsditch [64]

The only study available for comparison with the third order elastic constant terms is that of Cousins and Heggie. The results presented in that study were calculated using a modified Keating model. This involved the fitting of experimental data as well as certain assumptions being made concerning the internal strain. The results, therefore, must be considered to contain large uncertainties. Having said that, many of the results are seen to be similar.

The results presented in the thesis are believed to be the best obtainable for the current theory, DFT with LDA, and the most complete. The calculations have

Elastic Constant	Current pdddP DFT/LDA	Cousins [46]	Elastic Constant	Current pdddP DFT/LDA	Cousins [46]
C_{111}	-5950	-11690.5	C_{244}	279.5	-4.8
C_{111}^0	-7139	-8641.4	C_{244}^0	289.9	-9.0
Δ_{111}	1189	-3049.5	Δ_{244}	-10.4	4.2
C_{113}	-12.0	-7.4	C_{166}	-814.3	-6786.8
C_{113}^0	12.0	-14.1	C_{166}^0	-1579.0	-899.7
Δ_{113}	-16.8	6.7	Δ_{166}	-2393	-5887.1
C_{133}	54.0	-120.0	C_{266}	2296	972.0
C_{333}	-473.1	-572.0	C_{266}^0	-1403.9	2046.7
C_{144}	34.1	-8.6	Δ_{266}	3699	-1074.7
C_{144}^0	29.7	-4.4	C_{366}	38.2	3.4
Δ_{144}	4.4	-4.2	C_{366}^0	65.4	-3.4
C_{344}	-65.4	-74.7	Δ_{366}	-27.2	6.8

Table 3.4: Hexagonal Graphite: 3rd order elastic constants [GPa]

Cousins' results are from a modified Keating model.

(C_{xxx} denotes total elastic constant, C_{xxx}^0 partial elastic constant, Δ_{xxx} internal contribution to the elastic constant)

been carried through, for optimisation and single point energy, using consistent parameters for basis set and k-point grid. Internal strain has been considered throughout the second and third order terms for the first time and the results recorded for total and partial elastic constants as well as the internal contributions.

3.2 Zero Point Energy

In 1974, a study by Kelly and Eslick [21] was published calculating the effects of zero point lattice vibrations from the out of plane modes in hexagonal graphite. A model of the lattice vibration spectrum by Komatsu [78] was used in the Kelly study. Kelly [79] had shown that the the strain ϵ_3 was only affected by the out of plane modes in this model.

From the results of this study it was reported that the interlayer spacing was increased by $\sim 0.5\%$. It was also shown that the model predicted a contribution from the zero point energy to the elastic constant C_{33} of $\sim 2.4 \text{ GPa}$ approximately 6% of the experimental value.

3.2.1 Method

The free energy at zero temperature Eq 2.20 can be calculated ab initio under the AIMPRO code using DFT with LDA. The free energy contributions

$$U_0 \quad \text{and} \quad \frac{\hbar}{2} \sum_i \nu_i$$

are calculated separately.

The potential energy arising from the interatomic interactions is calculated in a similar manner to the elastic constants described above. The calculation is made with respect to the separation of the layer planes therefore ϵ_3 is the only strain required. The layers are strained in the same way as for the C_{33} calculations but over a larger range of strains ($\epsilon_3 = -0.16 \dots 3.0$).

For the vibrational mode calculations a set of results calculated by Haffenden [1] have been used. The AIMPRO code was used to calculate the vibrational modes with DFT under LDA. The calculations were performed using a 64 atom unit cell. Haffenden reported a “negligible difference” between the results using this size unit cell compared to a much larger 100 atom unit cell. A *pdpp* basis set was used for the calculations.

In the Haffenden study the vibrational modes were calculated over a range of interlayer strains

$$\epsilon_3 = \{-0.06, -0.04, -0.02, 0.10, 0.15, 0.20, 0.25\} \quad (3.6)$$

In this thesis a polynomial fit, Fig 3.4, has been applied to these results yielding the numerical second order differential of the vibrational terms with respect to the strain ϵ_3

$$\sum_i \frac{\partial^2 \nu_i}{\partial \epsilon_3^2} \quad (3.7)$$

For $T = 0$ C_{33} can be expressed as

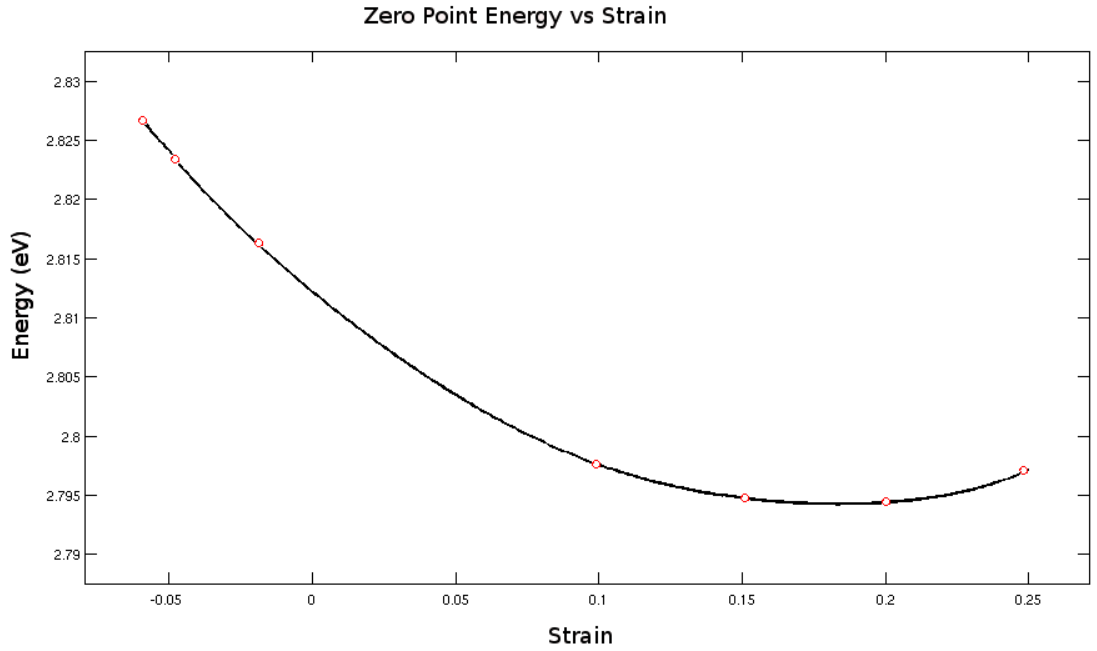


Figure 3.4: Anharmonic contribution to C_{33} vs strain

$$C_{33} = \frac{\partial^2 F}{\partial \epsilon_3^2} = \frac{\partial^2 U_0}{\partial \epsilon_3^2} + \frac{h}{2} \sum_i \frac{\partial^2 \nu_i}{\partial \epsilon_3^2} \quad (3.8)$$

The anharmonic term arising from the temperature contributions to Eq 2.19 can also be calculated using the vibrational mode results. This allows a polynomial fit of the energy and the second differential to be calculated numerically. The results can be used to find anharmonic contributions to the elastic constant C_{33}

as described in Eq 2.23.

The results from the vibrational mode calculations described above and two Lennard-Jones models, to be discussed further in section 3.3, have been used in combination to calculate interlayer separations. A target value of $C_{33}^{LJ} = 4.4 \text{ GPa}$ was used for the LJ models. Combining the resulting energies with the energy values given for ZPE and 300 K temperature corrections a value for the interlayer separation was found for both of the LJ models [5 – 10] and [6 – 12].

3.2.2 Results

The result for the zero point energy contribution to C_{33} from Eq 3.8 is

$$C_{33}^{ZPE} = \frac{\hbar}{2} \sum_i \frac{\partial^2 \nu_i}{\partial \epsilon_3^2} = 1.6 \text{ GPa} \quad (3.9)$$

The fit to the vibrational mode calculations was taken over large strain increments and not in detail around the energy minimum. Because of this the effect of the zero point energy contribution cannot be calculated with high accuracy.

The plot of C_{33}^{an} versus temperature in Fig 3.5 shows the temperature contributions to C_{33} . At room temperature $\sim 300 \text{ K}$ the contribution is

$$C_{33}^{an} = 0.4 \text{ GPa} \quad (3.10)$$

The correction to the elastic constant from zero point energy and the anharmonic effects at 300 K account for $\sim 2 \text{ GPa}$. This result, combined with the LDA single point energy calculations, reveal a shortfall of $\sim 4.4 \text{ GPa}$ when compared to the experimental value of $C_{33} = 36.5 \text{ GPa}$.

The effects to the interlayer separation resulting from the ZPE and 300 K temperature contribution combined with the LDA SPE and LJ models are summarised in Table 3.5. The 0 K interlayer separation results for LDA SPE with the LJ models are also listed along with an experimental value for reference. The interlayer

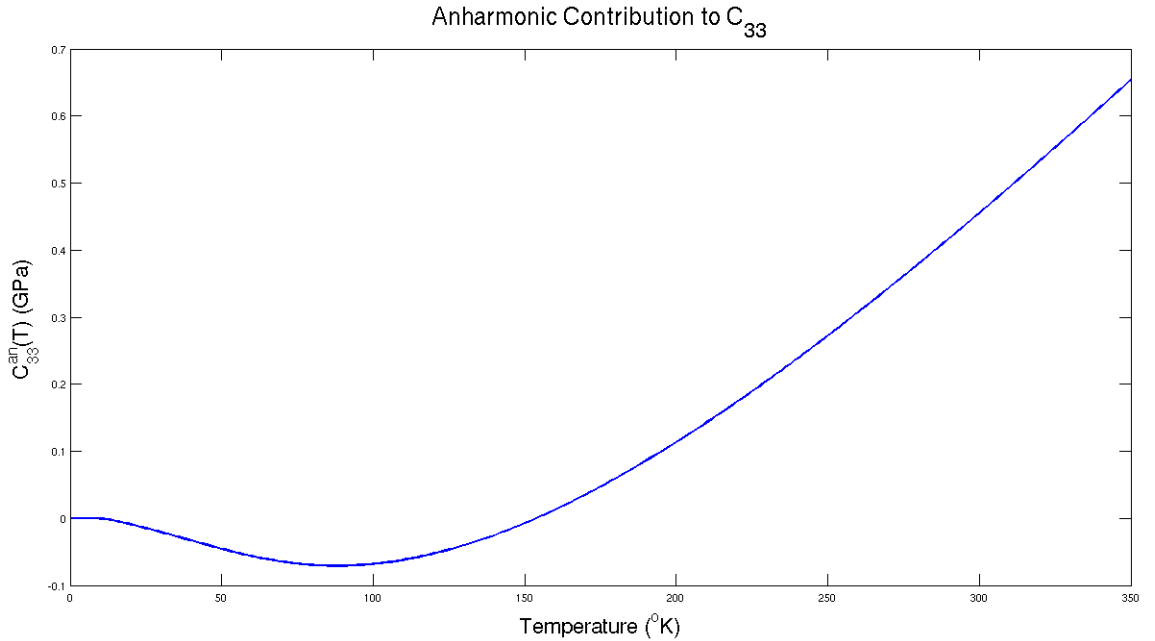


Figure 3.5: Anharmonic contribution to C_{33} in hex graphite vs temperature

separation recorded for LDA SPE, ZPE with the LJ [6 – 12] model at 300 K , $D = 3.37 \text{ \AA}$, is in excellent agreement with the experimental value $D = 3.35 \text{ \AA}$ [80].

3.3 Interlayer Binding

The binding energy calculated in this section is the energy required to separate all layers to infinity of a layered material such as graphite. This is most closely

Method	Interlayer separation (\AA)
LDA SPE, ZPE, LJ [5 – 10] at 300 K (this work)	3.27
LDA SPE, LJ [5 – 10] at 0 K (this work)	3.24
LDA SPE, ZPE, LJ [6 – 12] at 300 K (this work)	3.37
LDA SPE, LJ [6 – 12] at 0 K (this work)	3.32
Experimental (300K) ⁽¹⁾	3.35

Table 3.5: Interlayer separation

LDA SPE with ZPE using LJ [5 – 10] and [6 – 12] models at 300 K and LDA SPE with LJ [5 – 10] and [6 – 12] models at 0 K

(1) Donohue [80]

related to the exfoliation energy which involves removing a surface layer from a bulk material. The exfoliation energy is not to be confused with the cleavage energy which is the energy required to separate two layers within a bulk of material to infinity. An early paper by Girifalco and Lad [81] calculated the exfoliation energy of graphite to be approximately 18% smaller than the cleavage energy.

The exfoliation energy of graphite was measured by Girifalco and Lad using heat of wetting experiments. The result was reported to be $E_{ex} = 43 \pm 5 \text{ meV/atom}$. Unfortunately there is no information available for the type of graphite used in the experiments. This makes the uncertainties inherent in the experiment difficult to calculate.

Benedict *et al.*[82] inferred the cohesive energy of graphite by studying collapsed multiwall carbon nanotubes. The experimental procedure was based on the measurement of the diameter of hollow “bulbs” adjacent to three different collapsed carbon nanotubes. The precision of measurement was believed to be within $1 - 2 \text{ \AA}$. The results published in the report were $E_{ex} = 35_{-10}^{+15} \text{ meV/atom}$

A third study was undertaken by Zacharia *et al.* [83]. They studied the interaction of polyaromatic hydrocarbons (PAH) with the basal plane of graphite using thermal desorption spectroscopy. They reported a binding energy per carbon atom of the PAH of $52 \pm 5 \text{ meV}$ which can be identified with the interlayer cohesive energy of graphite. This study was carried out with particular emphasis on clearly defined experimental conditions with “a well characterized model system”.

A 2012 experimental study was carried out by Liu *et al.* [84]. They use a new technique based around the discovery of a “self-retraction phenomenon” in graphite flakes reported in a previous paper [85] by the group.

A graphite flake and a graphite step are created with smooth surfaces. The top surface of each graphite flake is then coated with a SiO_2 thin film. The energy, related to the binding energy, is a combination of elastic deformation energy of the top graphite/ SiO_2 flake and of the energy of the exposed graphite surfaces between the top flake and bottom mesa. A combination of atomic force energy (AFM) and

finite energy analysis is used to determine the binding energy of $31 \pm 2 \text{ meV/atom}$.

The interlayer interactions in graphite were modelled theoretically by Kelly [86] in 1970. Kelly used Lennard–Jones potentials between atoms in different layers. It was found that this type of potential was unsuitable for modelling interlayer interactions in graphite. The most obvious problem noted was the failure to describe the shearing motion of layers. The elastic constant C_{44} describing the shearing stiffness was calculated as 0.23 GPa using this model.

Since that time different theoretical techniques have been applied to the interlayer binding. Quantum Monte Carlo (QMC) methods have been used [87] also random phase approximation (RPA) [88, 89]. DFT with LDA [16, 72] and GGA [16] have been used. London dispersion force models have been developed to integrate with DFT with LDA [90, 91, 92, 93, 94].

In 2009 Spanu *et al.* [87] performed an *ab initio* study of the interlayer binding energies of graphite. Both variational QMC and lattice regularized diffusion Monte Carlo calculations were performed using the TURBORVB code [95]. These techniques inherently account for dispersion forces. A binding energy of $56 \pm 5 \text{ meV/atom}$ was reported after adding zero point energy and lattice vibration contributions at 300 K . It was noted that the calculation of the binding energy is more closely related to the cleavage energy than the exfoliation energy.

Spanu also noted that between 4 and 8 Å interlayer separation the energy curve follows a $D^{-4.2}$ behaviour, where D is the interlayer separation. This is a similar result to that found by Lebegue *et al.* [89] using adiabatic-connection fluctuation-dissipation theorem (ACFDT) for the random phase approximation (RPA) to the correlation energy. They reported a similar power law behaviour between 3 and 9 Å interlayer separation. The result calculated for the interlayer binding was 48 meV/atom .

DFT with GGA calculations of the interlayer interactions of graphite have been carried out by Savinini *et al.* [72]. The *ab initio* calculations result in an unacceptable interlayer separation of 4.2 Å . This led to Savini dismissing GGA

and using LDA alone. The resulting exfoliation energy for the LDA calculation was 24 meV/atom . The value was raised to 80 meV/atom when the dispersion forces and weak out of plane interactions were included in the calculation. The FIREBALL code [96] was used to implement these interactions.

A recent study by Graziano *et al.* [94] reports interlayer binding energies using various density functionals. These include the optimized Becke88 van der Waals (optB88-vdW) and the optimized PBE van der Waals [97]. Zero point energy contributions were also incorporated into the results. They found the zero point energy results to be similar for different functionals with a value less than 5 meV/atom .

3.3.1 Method

The method used for the DFT with LDA calculations used for the elastic constant C_{33} was applied to the inter layer interactions. The parameters for the previous C_{33} calculations were used as described in Section 3.1.2.

To calculate the exfoliation energy the ϵ_3 strain was increased until the energy levelled off implying no further interlayer binding interactions. The difference in the minimum and maximum calculated energies gives the binding energy from this method.

Dispersion interactions have been modelled using Lennard–Jones [5–10] Eq 3.11 and Lennard–Jones [6 – 12] Eq 3.12 type potentials.

$$V_{LJ}(r) = 4\epsilon \left[- \left(\frac{\sigma}{r} \right)^5 + \left(\frac{\sigma}{r} \right)^{10} \right] \quad (3.11)$$

$$V_{LJ}(r) = 4\epsilon \left[- \left(\frac{\sigma}{r} \right)^6 + \left(\frac{\sigma}{r} \right)^{12} \right] \quad (3.12)$$

Here r is the distance between atoms, σ is the interlayer separation for the DFT calculated energy minimum and ϵ is a coefficient with units of energy.

Other variations of the Lennard–Jones model were tested, for example LJ [4 – 8], but discarded. The LJ [5 – 10] model was found to give a similar long

range gradient to that reported by Spanu *et al.* [87]. The LJ [6 – 12] model was seen to give the closest binding energy and interlayer separation values to experimental results.

A short Octave program (see Appendix A) was written to run the calculation with the following structure. An α and a β atom were used as reference carbon atoms within a reference graphite layer. The carbon atom positions were taken from the AIMPRO hexagonal graphite unit cell optimisation. The interaction between atoms in layers above the reference layer were calculated using both Eq 3.11 and Eq 3.12 for the α and β atoms separately. A cut off radius r_c from the reference atoms was used within the layers to limit the horizontal distance for atom-atom calculations.

The coefficient ϵ used in Eq 3.11 and Eq 3.12 was adjusted to give a combined LDA SPE with LJ result of $C_{33} = 36.5 \text{ GPa}$. A layer cut off was used above the reference atom layer to limit vertical atom-atom calculations. The energies were found to converge for a horizontal cut off radius of 400 Å and a layer cut off of 40 layers above the reference atoms.

3.3.2 Results

Having calculated the energies, in the manner described above, the combined AIMPRO DFT with LDA single point energies, ZPE, anharmonic temperature contributions at 300 K and LJ [5 – 10] and LJ [6 – 12] result in binding energies of: $BE[5 - 10] = -117.3 \text{ meV/atom}$ and $BE[6 - 12] = -50.6 \text{ meV/atom}$. This is compared to -29 meV/atom for the DFT with LDA SPE calculations alone.

Fig 3.6(a) shows the LDA SPE binding energy versus separation. A plot of the binding energy for the LDA SPE combined with Lennard-Jones energies for [5 – 10] and [6 – 12] are presented in Fig 3.6(b). The plot shown in Fig 3.6(c) illustrates the QMC results from Spanu *et al.* [87] for comparison. It may be noted, when comparing the LDA SPE and LDA SPE + LJ plots, that the LDA SPE energy asymptotes to zero more rapidly than the combined results. This is

Method	Energy (meV/atom)
LDA SPE and LJ [5 – 10] (this work)	–117
LDA SPE and LJ [6 – 12] (this work)	–51
Heat of wetting (expt) ⁽¹⁾	–43 ± 5
PAH (expt) ⁽²⁾	–52 ± 5
Self retraction (expt) ⁽³⁾	–31 ± 2
Quantum Monte Carlo ⁽⁴⁾	–56 ± 5
ACFD theorem with DRA ⁽⁵⁾	–48
LDA optB88-vdW ⁽⁶⁾	–60
LDA optPBE-vdW ⁽⁶⁾	–56

Table 3.6: Binding energy results from experiment (expt) and theory

- (1) Girifalco [81]
- (2) Zacharia *et al.* [83]
- (3) Liu *et al.* [84]
- (4) Spanu *et al.* [87]
- (5) Lebegue *et al.* [89]
- (6) Graziano *et al.* [94]

as expected knowing that the LDA SPE calculations only model the close range interlayer binding arising from the p_z orbital overlap.

The addition of the LJ terms apply a long range, weakly attractive force between the layers when added to the DFT LDA results. This extended range of interlayer interaction can be observed as the LDA SPE + LJ energy gradient gradually tends towards zero. Spanu *et al.* [87] reported that their best fit was given by the LRDMC using a $2 \times 2 \times 2$ super cell. This can be seen in Fig 3.6(c).

It should be noted that the method used for the Spanu calculations produced a result comparable to the cleavage energy rather than the exfoliation energy. As mentioned above the cleavage energy has been estimated to be $\sim 18\%$ greater than the exfoliation energy. Assuming that this were true the adjusted figure for the Spanu calculation would become $BE = 46 \pm 4 \text{ meV/atom}$. It should also be noted that the Spanu result includes contributions from zero point energy.

The DFT with LDA SPE and Lennard Jones results shown in this work are most closely related to the exfoliation energy experiments as summarised in

Table 3.6. The result presented for LDA SPE and LJ [6 – 12] is equal to the Liu [84] experimental result within the error bars given. It must be remembered, however, that the results for the binding energy presented in this work do not include the contributions from the ZPE or temperature effects.

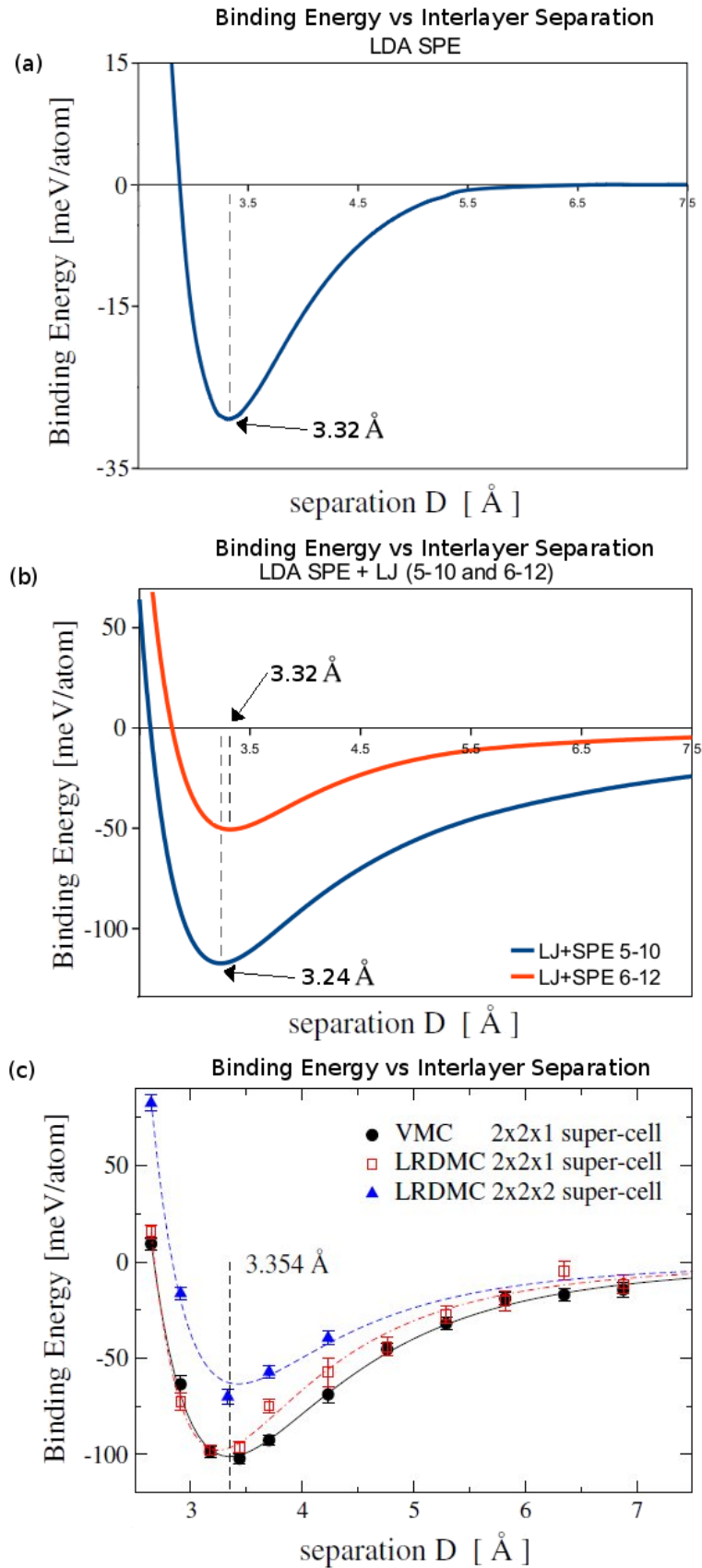


Figure 3.6: Binding energy vs interlayer separation
 (a) DFT with LDA Single Point Energy (SPE)
 (b) DFT with LDA SPE, ZPE and LJ [5–10] and LJ [6–12] (current work)
 (c) Spanu [87] using Quantum Monte Carlo

Chapter 4

Bromine intercalated graphite

4.1 Elastic Constants of Brominated Graphite

4.1.1 Introduction

Graphite is a host material that readily accepts intercalation compounds. This arises from the highly anisotropic nature of graphite with very strong intralayer bonding compared to the weak interlayer bonding. Molecular layers of a certain species are inserted between the layers of graphite. The amount of intercalation is measured by the number of intercalated layers compared to the host layers. The number of host layers lying between the intercalant layers is classified by a stage index n . The staging can exist in a regular pattern over a range of many layers [59].

Eeles and Turnbull [98] studied graphite-bromine compounds in 1965 using electron and x-ray diffraction and electron microscopy. They noted the ease with which graphite can be brominated “at room temperature merely on immersion of the graphite in bromine liquid or vapour”. They reported that the most stable compound in the lower half of the concentration range was C_8Br with quasi stable states of $C_{16}Br$ and $C_{24}Br$.

Heald and Stern [99] carried out an extended-x-ray-absorption-fine-structure (EXAFS) study on intercalated graphite in 1978. They found a very small

separation between graphite layer and intercalated bromine of 2.12 Å. However Eeles and Turnbull [98] reported a larger separation of 3.5 Å.

Sasa *et al.* [100] identified 2nd, 3rd, 4th and 5th stage structures of intercalated bromine in graphite using x-ray diffraction. For C_8Br in stage-2 they found a graphite interlayer spacing of 7.03 Å between layers sandwiching the bromine.

In 1986 Simon *et al.*[101] published inelastic neutron scattering results for the elastic constants C_{44} and C_{55} for stage-2 brominated graphite. They reported very weak elastic constants of $C_{44} = 0.02 \pm 0.03$ GPa and $C_{55} = 0.18 \pm 0.04$ GPa.

A DFT with LDA study of brominated graphene and stage one and stage two bromine intercalated graphite was carried out in 2011 by Yaya *et al.* [102]. For graphite they found a minimum Br_2 concentration for exothermic intercalation of $C_{16n}Br_2$ where n is the number of stages.

4.1.2 Method

The study of the stage-1 and stage-2 bromine intercalated graphite elastic constants was carried out with the AIMPRO code using DFT with LDA. The same stage-1 and stage-2 structures used in the Yaya study were used here along with similar parameters. The stage-1 structure is made of 18 carbon atoms in a graphene sheet with a dimer of two bromine atoms as shown in Fig 4.1 (a). The structure is repeated as a super cell in three dimensions resulting in AA stacking of the graphene layers. The stage-2 structure, shown in Fig 4.1 (b), is formed of 36 carbon atoms in two graphene layers with the bromine dimer intercalated between the layers. The layers in the stage-2 case are AB stacked.

Two different wave function basis sets were used to match the two species involved in the calculations. For the graphene layers the wave function basis set used was *pdpp* and for the bromine dimers an *fddd* basis set was used. To aid convergence of the structure a finite temperature electron level filling of $kT = 0.04$ eV was used. Hartwigsen, Goedecker, and Hutter [11] norm conserving pseudopotentials were used to model the core electrons. The Brillouin zone

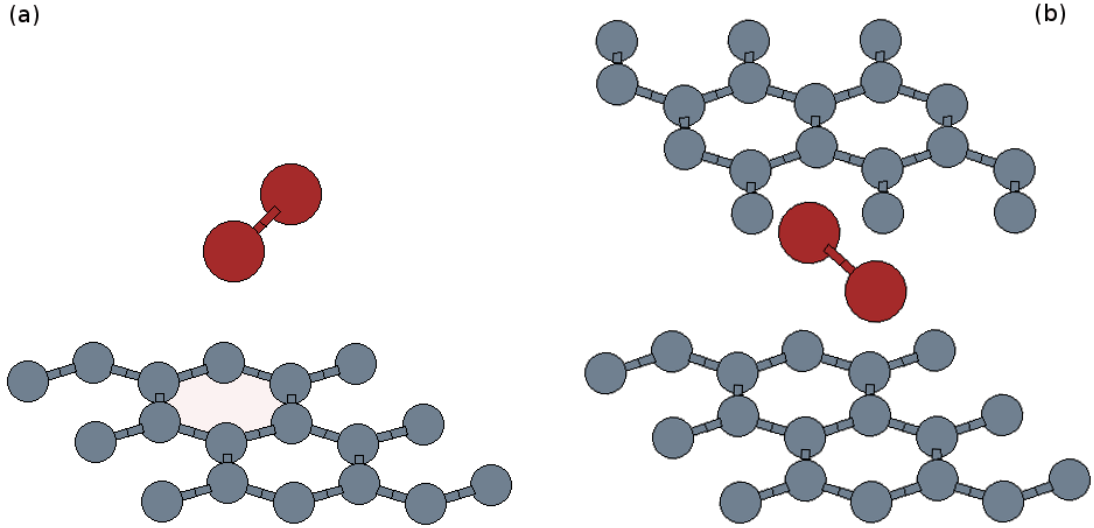


Figure 4.1: (a) $C_{18}Br_2$ unit cell (b) $C_{36}-Br_2$ unit cell

integrations were carried out with a mesh of $6 \times 6 \times 4$ k-points.

The method used to extract the elastic constant data for the stage-1 and stage-2 bromine intercalated graphite was similar to that applied to finding the C_{33} elastic constants of hexagonal graphite as described in Chapter 3. The interlayer strain ϵ_3 was increased in equal increments of 0.002, from -0.006 to 0.006 , and the single point energy results fitted to a polynomial. The elastic constants could then be found as the coefficients of the polynomial fit multiplied by the relevant coefficient.

4.1.3 Results

After optimising stage-1 and stage-2 the unit cell lattice parameters were found. For the stage-1 optimised cell $a = 7.33 \text{ \AA}$ and $c = 6.56 \text{ \AA}$ and for the stage-2 unit cell $a = 7.33 \text{ \AA}$ and $c = 9.80 \text{ \AA}$. The $Br-Br$ bond length was calculated to be 2.35 \AA for stage-1 calculations and 2.36 \AA for the stage-2 calculations.

The total elastic constant C_{33} for Stage-1 was calculated to be $C_{33} = 12.5 \text{ GPa}$. For Stage-2 a result of $C_{33} = 21.4 \text{ GPa}$ was found for the total elastic constant. There is no internal strain contribution to the values of C_{33} .

The strength of the elastic constant C_{33} is seen to decrease with staging as the ratio of graphite to bromine increases. Linearly fitting the C_{33} values found for

Stage-1 and Stage-2 intercalation with the ratios of graphene layers to bromine layers leads to an extrapolated value, for infinite staging (i.e. pure graphite), of $C_{33} = 39.3 \text{ GPa}$. This is compared to the calculated value of $C_{33} = 39.5 \text{ GPa}$.

The total elastic constant values for C_{44} and C_{55} have also been calculated for Stage-1 and Stage-2. The values are summarised, along with those for C_{33} in table 4.1.

Stage	C_{33}	C_{44}	C_{55}
1	12.5	1.2	0.9
2	21.4	5.3	4.5

Table 4.1: Elastic constant values (GPa) for Br_2 intercalated graphite

It has been noted [103] after these calculations were completed that a lower energy layer stacking may exist for the Stage-2 intercalated graphite. This is a job that could be undertaken in the future. The stacking alluded to is that of the form $AB - \text{Br}_2 - BA$ in place of the $AB - \text{Br}_2 - AB$ presented in this work. Other ideas for future work may include the use of higher k -points in calculations of a similar type as the $6 \times 6 \times 4$ used in this work is rather low. Higher staging could also be attempted to show the value of fitting linearly to predict higher staging values of C_{33} .

Chapter 5

Modelling Graphite Under Irradiation

5.1 Introduction

The UK nuclear industry has been generating power using graphite moderated carbon dioxide cooled reactors since the 1950s. The working life of the reactor is directly linked to the graphite used in the moderators. Under the normal running operation of the generator the graphite is continually bombarded by particle radiation. When the graphite becomes so damaged that it is deemed no longer safe for use in the reactor the entire plant must be decommissioned. This has led to a large number of experiments being carried out and the resulting data concerning irradiated graphite.

The two main areas of interest are the dimensional changes experienced by the graphite under irradiation and the accompanying changes in energy stored within the material. Large scale measurable changes in structure can be broken down to interactions between smaller scales. In this section a two dimensional model at the macroscopic scale ($\sim 1\mu m$) is proposed to explain the dimensional and energy changes seen in crystallites of graphite.

Under irradiation graphite is seen to expand along the c-direction, perpendicular

to the graphene layers and contract along the a direction, parallel to the graphene planes [104, 105]. The currently accepted model [106] used to explain the dimensional changes is based on interstitial dislocation loops causing expansion in the c -direction. The contraction of the layers is thought to come from the annealing of vacancy lines resulting from the interstitial atoms removed from the lattice.

The validity of this model, often referred to as the 'standard model', has been called into question [107]. The model describes the aggregation of interstitial atoms forming new graphene sheets. This has not been seen experimentally. Studies of irradiated graphite using high resolution transmission electron microscopy (HRTEM) have been carried out [108, 109, 110, 111]. Images showing the layered sheets give evidence of bending and breaking of the layers rather than interstitial clusters. This can be seen in Fig 5.1. The images are not of neutron irradiation but electron beam irradiation. The HRTEM images were created at low temperature ($\sim 100^\circ C$). The authors stated that the images were "quite similar" to the images of irradiated graphite presented in their study [111]. They stressed that care must be taken when interpreting the HRTEM images as they are not a direct image of the real lattice.

The way that energy is stored and released by graphite under irradiation is controlled by different mechanisms depending on temperature. At temperatures up to $600^\circ C$ point defect annihilation releases formation energy stored in the system. This type of stored energy is commonly referred to as Wigner energy. A large peak in energy release is seen at $\sim 200^\circ C$. The release of energy is so large that it can lead to dangerous runaway temperature rises in the reactor. An example of this type of behaviour was witnessed in 1957 at Windscale Pile 1 accident [112].

The model presented in this chapter tackles the problems of dimensional change and energy storage in irradiated graphite using dislocation theory. Within a two-dimensional crystal basal dislocations are responsible for transporting material by glide along the layers. Pileups of basal dislocations occurring in a simulation represent different damage scenarios. It is postulated that these dislocation

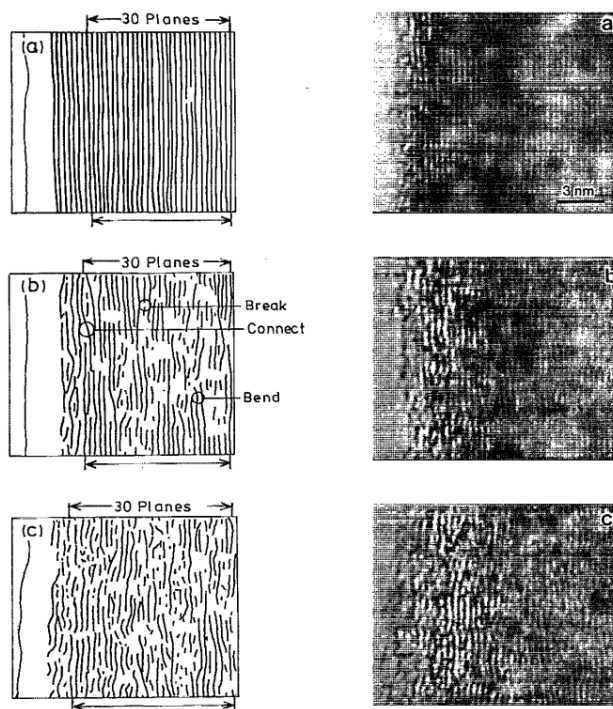


Figure 5.1: Bending, breaking and cross connecting of the graphene planes[110]. Left hand images are basal plane traces of right hand images

arrangements created by basal glide can be represented using prismatic dislocations. The prismatic dislocations create the required expansion in the c -direction. They are also responsible for introducing energy into the crystal. The internal energy is seen to peak for a certain density of dislocations.

5.1.1 Irradiation damage in graphite

The aim of the model is to explore the c -direction expansion of graphite and the change in stored energy, both as a function of fluence. Graphite is used as a nuclear moderator in high temperature reactors. This has created a great interest in its material behaviour under such conditions. Many studies have been carried out from the 1950s up until present times.

The first X-Ray measurements of irradiated graphite showing prismatic expansion and basal contraction are thought to have been carried out by Zachariassen[113] in 1945. Transmission electron microscope (TEM) studies have given the most useful observations of irradiated graphite. The first transmission electron microscope

images of irradiated graphite were published in 1958 by Grennall [114] and 1960 by Bollman [115]. Lattice scale imaging became possible using techniques such as scanning-tunnelling microscopy (STM), atomic-force microscopy (AFM) and high resolution TEM.

Under irradiation the atoms in the lattice can be displaced by incident high energy particles. These particles can be charged, such as ions or electrons, or uncharged neutrons. Wigner[116] was the first to estimate the number of carbon atoms displaced from their lattice sites under neutron irradiation in graphite. This work was carried out in 1942. In 1949 Seitz[117] calculated a value of 1870 displacements for a 2 MeV neutron being slowed to thermal energies in graphite.

The most commonly accepted theory put forward to describe the dimensional change in graphite is referred to as the standard model. Under fast neutron irradiation the displaced atoms are thought to be displaced as self interstitial atoms between the graphene layers. The interstitial atoms are believed to be highly mobile and aggregate into prismatic loops which grow to form new layers. It is this arrangement that is thought to account for the c expansion [118, 119, 120, 121].

The contraction of the graphene sheets was proposed by Kelly [120] and others. At temperatures where the vacancies left from the self interstitial atoms were believed to be relatively immobile there was thought to be “collapse parallel to the basal plane” thereby removing the vacancy. At temperatures where the vacancies were believed to be mobile they were thought to “diffuse to crystal boundaries” with the same net affect of basal contraction.

Bollmann’s [115] study of irradiated graphite compared his TEM data to x-ray data from Woods *et al.* [122]. The study was carried out on extruded grade A reactor graphite. Samples were irradiated to 10^{20} n/cm^2 and $8 \times 10^{20} \text{ n/cm}^2$ at temperatures of 30°C and 50°C respectively.

The image in Fig 5.2 (a), for a dose of 10^{20} n/cm^2 at room temperature, shows light and dark dots with dimensions up to $\sim 60 \text{ \AA}$ diameter. The defects at this dose are mostly separated. Bollmann refers to a “transition dose” at

$\sim 6 \times 10^{20} \text{ n/cm}^2$ where the defects interact to a much greater extent. This is shown by the increase in overlapping in Fig 5.2 (b) for a dose of $8 \times 10^{20} \text{ n/cm}^2$.

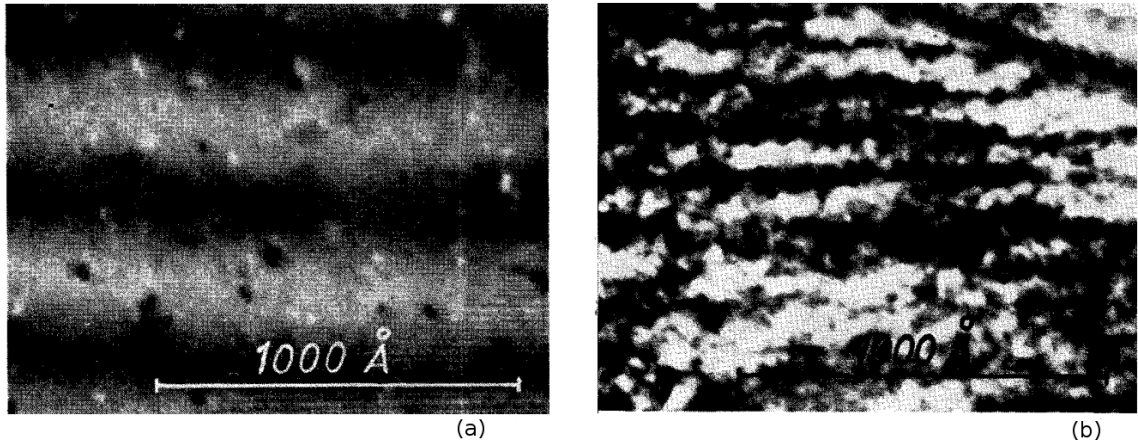


Figure 5.2: (a) Graphite irradiated to 10^{20} n/cm^2 at 30°C
 (b) Graphite irradiated to $8 \times 10^{20} \text{ n/cm}^2$ at 50°C [115]

This can be compared to the Woods x-ray data of Fig 5.3. The narrow peaks seen for unirradiated and $4.39 \times 10^{20} \text{ NVT}$ suggest an interlayer expansion for material with similar periodicity. An increased broadening in the 0002 x-ray line shown above these doses indicates the breakdown in periodicity of the lattice. This shows agreement with the TEM images in Fig 5.2.

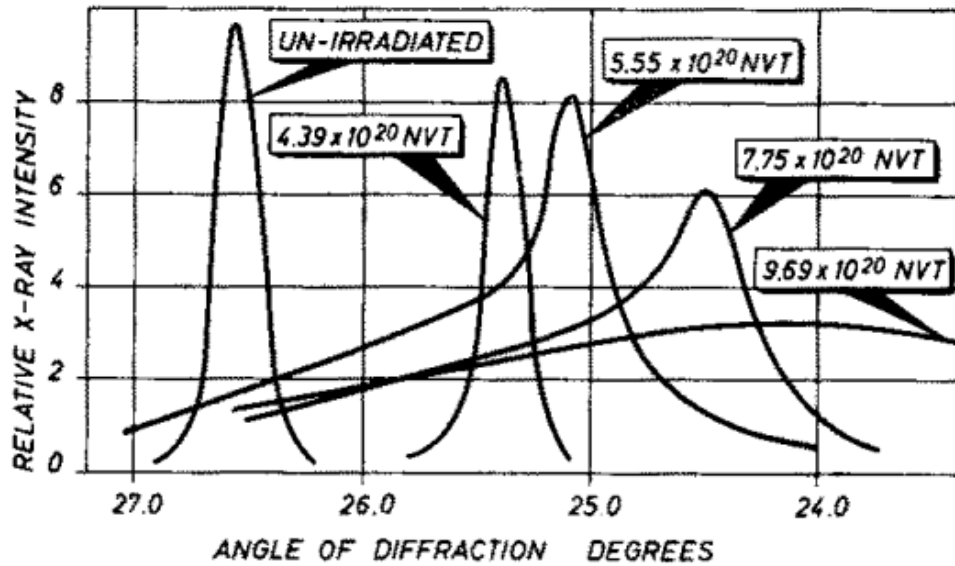


Figure 5.3: Changes of the 0002 x-ray line with increasing dose [122]

5.1.2 2–D Dislocation Models

5.1.3 Background

Two dimensional dislocation dynamic simulations have been found in the literature for some time. During the latter 1980s the first simulations were undertaken by Ghoniem and Amodeo [123] and Lepinoux and Kubin [124, 125]. The two dimensional models were developed by Guluoglu *et al.* [126], Ghoniem and Amodeo [127, 128], Lubarda *et al.* [129] and others in subsequent years.

With increasing computer power it became viable to produce three dimensional dislocation models. The models for three dimensional simulations vary in the treatment of the dislocation line. A group of simulations for pure edge or screw with straight line segments were produced by Kubin *et al.* [130], Devincere *et al.* [131] and Moulin *et al.* [132] and similar for mixed edge and screw Zbib *et al.* [133]. Another model was developed for curved dislocation line segments. This was seen in the work of Kukta and Freund [134] and Ghoniem and Sun [135].

The introduction of these three dimensional dislocation models has not ended the usefulness of the two dimensional model. Studies by Buehler *et al.* [136], Espinosa *et al.* [137] and others have been carried out on small scale plasticity. Various applications to crack tips have been undertaken by Deshpande *et al.* [138], Broedling *et al.* [139], Bhandakkar *et al.* [140] and others. A study of void growth has been carried out by Hussein *et al.* [141] and Segurado and Llorca [142], delamination by ODay [143] and size effects in single crystals by Guruprasad and Benzerga [144]. Mechanical response under load for single and polycrystalline materials has been simulated by Biner and Morris [145], Lefebvre *et al.* [146], Chakravarthy and Curtin [147], Ahmed and Hartmaier [148] and others.

Boundary conditions are normally applied to the dislocation models. The two main groups of boundary condition are periodic and non periodic. A method for non periodic boundary condition can be found in the paper by Mura [149]. A periodic boundary solution can be found in Pang [150].

A paper by Ahmed [148] published in 2010 uses a two dimensional dislocation dynamics model to study the stress–strain relationship of a material.

5.1.4 DD2D Model

The dislocation program is referred to as DD2D standing for dislocation dynamics in two dimensions. I have developed the program during my thesis. It has been written using the C++ language compiled under the QT [151] platform. In this section the workings of the DD2D model will be discussed.

The model was originally created using isotropic theory and applied solely to basal dislocations. The dislocations were allowed to glide under the influence of the Peierls forces generated between the dislocations. Oppositely signed dislocations that came within a critical radius would annihilate with one another and release their energies from the system. Basal dislocations in graphite can glide along planes very easily if unobstructed.

The overarching idea was to combine basal and prismatic dislocations into one model. The prismatic dislocations provide a mechanism for expansion in the c-direction while the basal dislocations provide a mechanism for transport of material along the graphene layers. The combination of these two mechanisms could provide a simple theory for c-expansion in irradiated graphite. The basal dislocations would be used to model material displacements within the two-dimensional crystal caused by neutron irradiation while the prismatic dislocations would model the various types of deformation that may occur such as ruck and tuck, wrinkling of the layers or prismatic loops from displaced material situated between layers. This is discussed further in Section 5.1.6.

The results shown in this thesis have come from adapting the model to use only prismatic dislocations. These are used to simulate the deformations as described above. The transport of material that would come about by basal dislocation glide has not yet been included. The idea of the model in this form is to show that it is suitable to describe c-axis expansion in a layered material such as graphite and

that it can be used to study energy behaviour in graphite.

During the final year of my PhD studies I have been assisted by Pippa Young a DPhil student studying under the supervision of Professor Malcolm Heggie. She has been especially helpful in advancing the graphical output of the program.

5.1.5 Dislocation Types

According to Fujita and Izui [152] there are four fundamental dislocation types in graphite:

1. Burgers vector parallel and dislocation line perpendicular to the basal plane.
2. Burgers vector and line perpendicular to the basal plane.
3. Burgers vector parallel to the basal plane and line lying within the basal plane.
4. Burgers vector perpendicular to the basal plane and dislocation line within the basal plane.

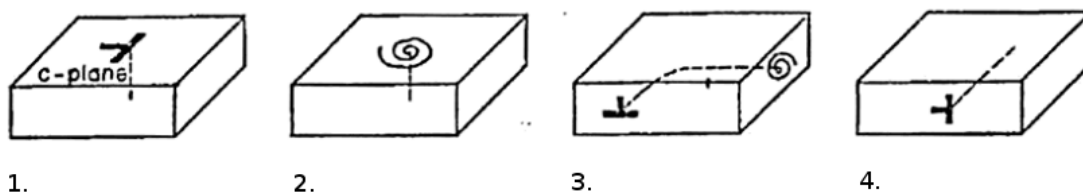


Figure 5.4: The four fundamental dislocation types of graphite.
Adapted from [152]

Two of these dislocations are considered in this thesis. Both types will be considered to have infinite straight line vectors perpendicular to a plane containing the dislocation's Burgers vectors. Type 3. is a basal edge dislocation. This type of dislocation has very low resistance to glide within the basal plane. This is a result of the low shear stiffness of graphite represented by the elastic constant C_{44} . Graphite samples from material irradiated in nuclear reactors are known to have

large turbostratic regions. The layers randomly oriented around the c axis have been studied [153] and shown to have C_{44} close to zero. This implies the basal edge dislocations have almost no resistance to glide.

The second is type 4. a prismatic edge dislocation. Prismatic edge dislocations have Burgers vector perpendicular to the basal plane. The prismatic dislocations considered are used to represent either a group of interstitial prismatic atoms or some another source of deformation that results in c axis dilation.

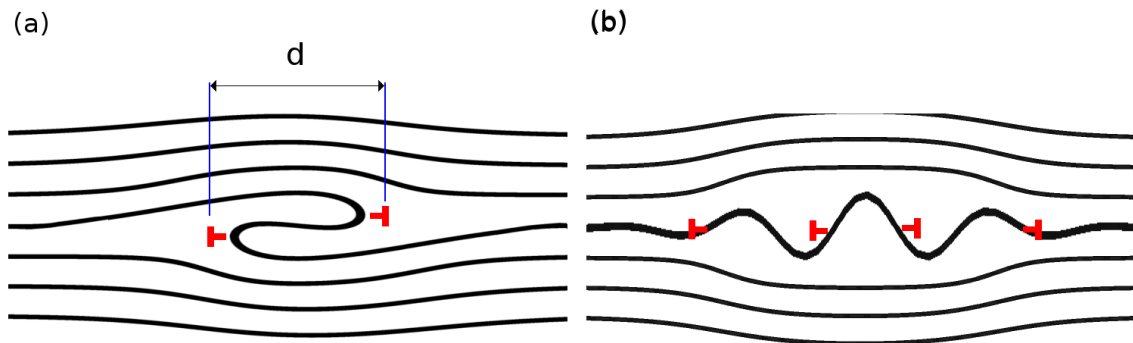
The dislocations are always formed as pairs of oppositely signed dislocation dipoles in the model. A prismatic dislocation dipole is considered to be sessile with respect to glide in the prismatic direction i.e. along the direction of layer stacking. It is possible, however, for the prismatic dislocations to move by climb in the glide direction of the basal dislocations.

The movement by climb of an interstitial dislocation has a different mechanism to the shear stress responsible for the basal dislocation glide. The climb comes about from the interlayer stresses. The material enclosed between the dipoles is sandwiched between layers of material so does not interact with other atoms during climb in the way that a basal dislocation does when moving through a layer of atoms. The movement depends on a stress gradient across the width of the dipole. A relative compression of layers one side of the dipole compared to the other of sufficient magnitude will cause climb.

In the model any climb of prismatic dipoles takes place conservatively. No atoms are added or removed and the dipole representing the section of material is moved with constant separation between the dipoles.

5.1.6 Representation by prismatic dipoles

The effect of a prismatic dipole introduced into a continuum using the displacement equations Eq 2.119 is to cause an area of dilation in the c axis above and below the width of the dislocation pair. This can be used to represent other possible defects in the structure. Heggie [107] has proposed a Ruck and Tuck structure that

**Figure 5.5:**

(a) Ruck and tuck

(b) Wrinkle

dislocations shown in red
 dislocation dipole separation d

can be modelled by either a pile up of basal dislocations or prismatic dislocation dipoles [154]. A schematic of the Ruck and Tuck defect is shown in Fig 5.5 (a). Another possible defect is the wrinkling of a layer or layers as shown in Fig 5.5 (b). The details of this deformation have not been worked out completely but a suggested representation using prismatic dislocations is shown in the figure.

In the DD2D runs two different values of Burgers vector were used, $b = 3.32 \text{ \AA}$ and $b = 6.64 \text{ \AA}$. The smaller value corresponds to material trapped between layers in the form of prismatic loops. This type of defect can be considered to be a single partial layer with a Burgers vector equal to the separation of one interlayer spacing. The larger value is used to model the Ruck and Tuck defect. For this case the folded structure must be represented by a Burgers vector with magnitude equal to two layer separations. The selected output produced below is for Burgers vector $b = 6.64 \text{ \AA}$.

The horizontal separation d of the dislocation dipoles is a measure of the size of the deformation. This is highlighted in Fig 5.5 (a). The value of d also relates to the amount of extra material being placed into the crystal, for example in the extra material in the folds of the Ruck and Tuck.

Two different values of d were used in the DD2D runs, $d = 30 \text{ \AA}$ and $d = 60 \text{ \AA}$. These are arbitrary values used to check the uniform increase in c-expansion with

increase in dipole width.

5.1.7 User input and graphical output

The QT platform has been developed by Nokia corporation with the aim of facilitating the creation of mobile phone and desktop applications. It has been used here to allow for animation of the dislocation model. The platform also offers straightforward integration of interactive buttons, sliders etc. This makes it easy to allow user interaction at runtime. ImageMagick [155] libraries have been called from within the program to save output of plots and images for use after the application has been closed.

It is possible to alter runtime parameters during the operation of the program. A choice to use isotropic or anisotropic elasticity theory can be made, the Burgers vector magnitude can be altered and the initial number of dislocation dipoles can be chosen.

Parameters that can be set for the running of the program include the number of iterations to be executed and for each iteration the number of new dislocation dipoles to be entered into the model. Also, if there is to be relaxation of the dislocation energies for each iteration, the number of time steps can be chosen. This controls the number of time steps for which the dislocations will be allowed to relax before the introduction of any new dislocations with the next iteration.

A *Dislocation positions* option can be used for testing purposes. The normal option is to use the *Randomise positions* option. This introduces the new dislocations into the system at random x and y positions rather than in a predefined order.

The size of the plane can be chosen in the x and y directions. The values input are in units of Angstrom. The two dimensional plane containing the dislocations can be seen in, for example, the upper half of Fig 5.6. A single prismatic dislocation dipole is shown. The effect on the edge of the plane, caused by strain from the introduction of dislocation dipoles, is indicated by the black dashed line. This is

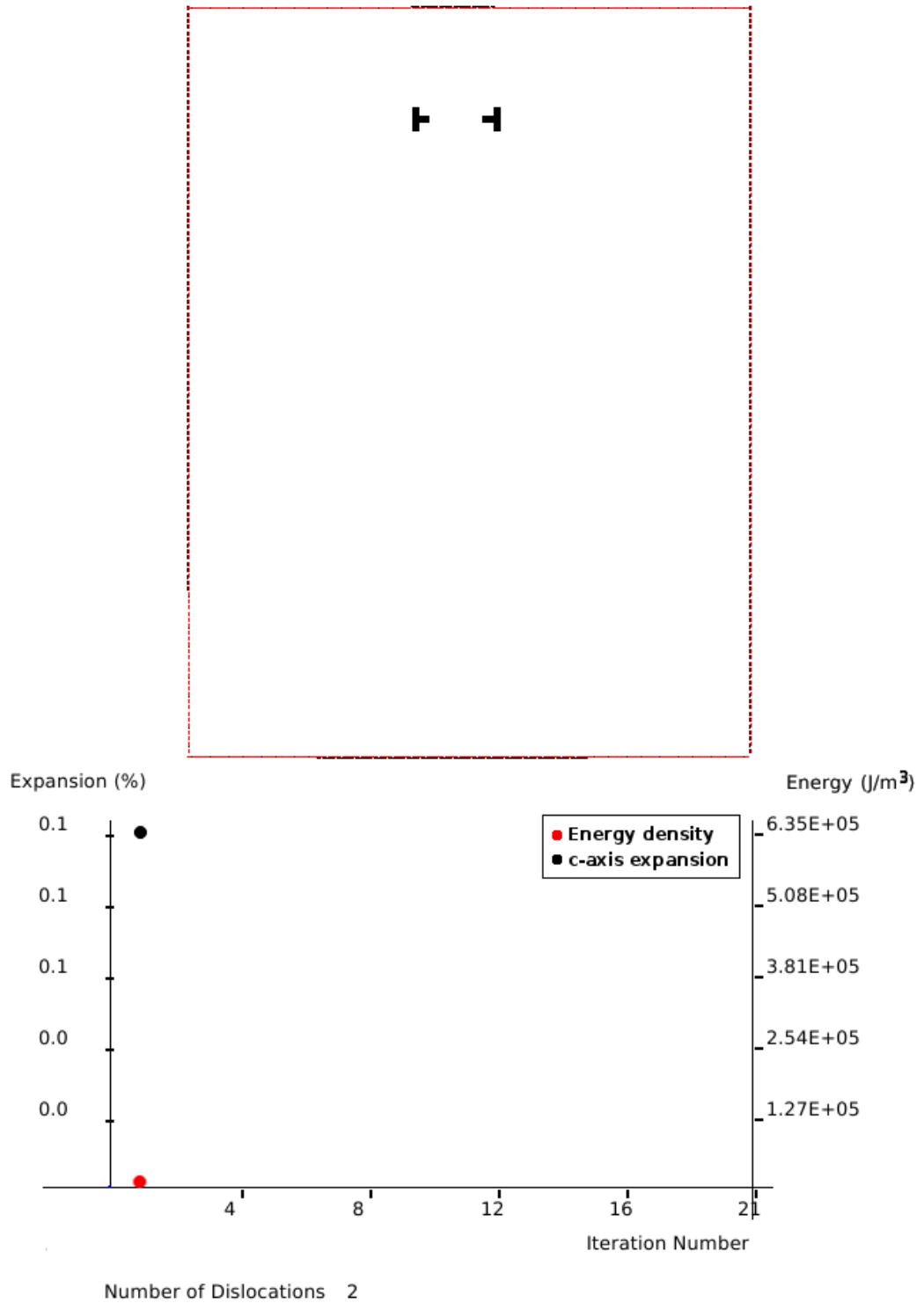


Figure 5.6: Example sequence of outputs from DD2D run for 800×600 cell
 1) First iteration showing single prismatic dislocation dipole

Upper image displays geometry of dislocations within the 2-D crystal
 red/black outline describes unstrained/strained crystal boundary

Lower image displays plotted points of the energy and c-axis expansion vs iteration

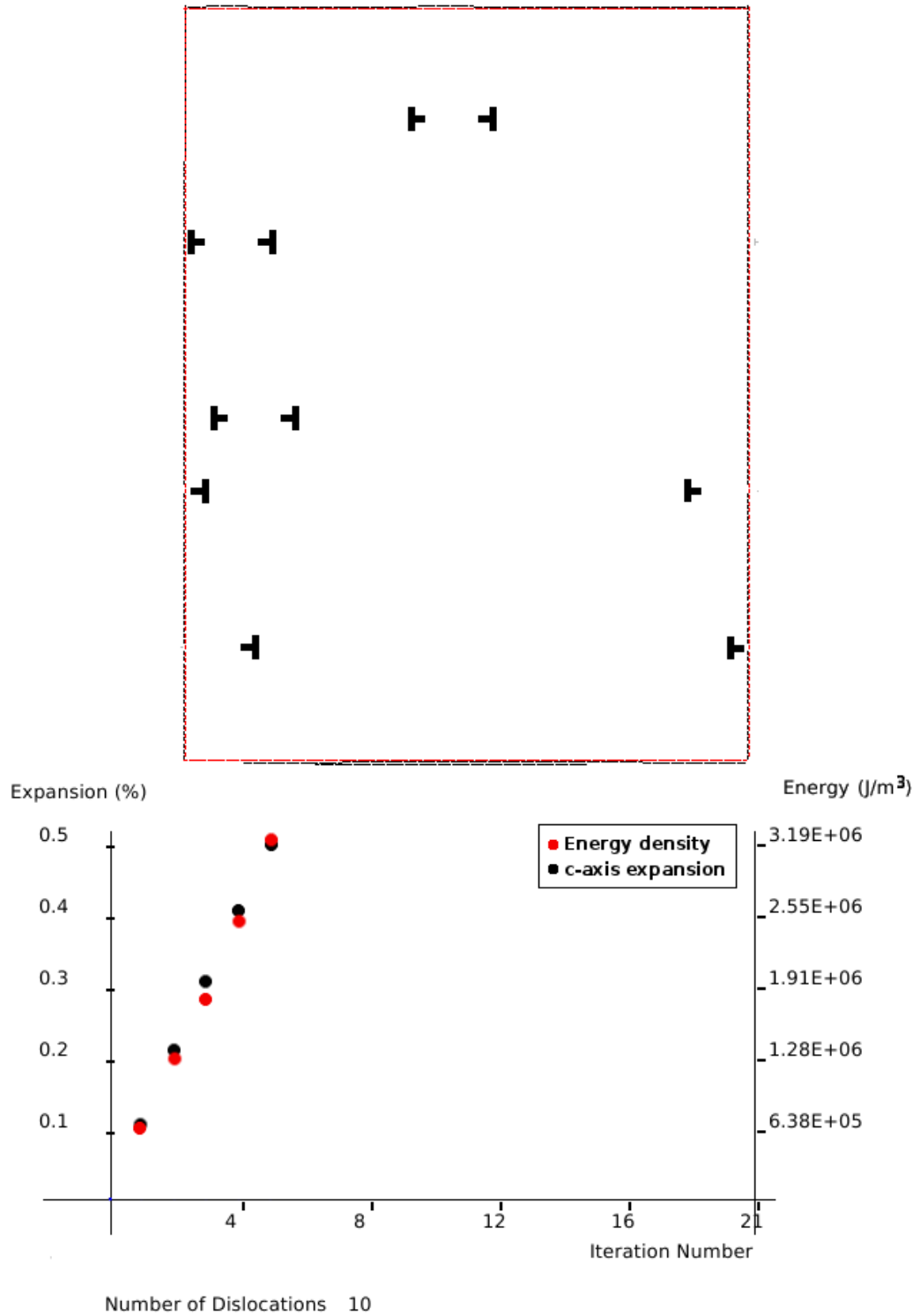


Figure 5.7: Example sequence of outputs from DD2D run for 800×600 cell
 2) Iteration 10 showing 10 prismatic dislocation dipoles

Upper image displays geometry of dislocations within the 2-D crystal
 red/black outline describes unstrained/strained crystal boundary

Lower image displays plotted points of the energy and c-axis expansion vs
 iteration

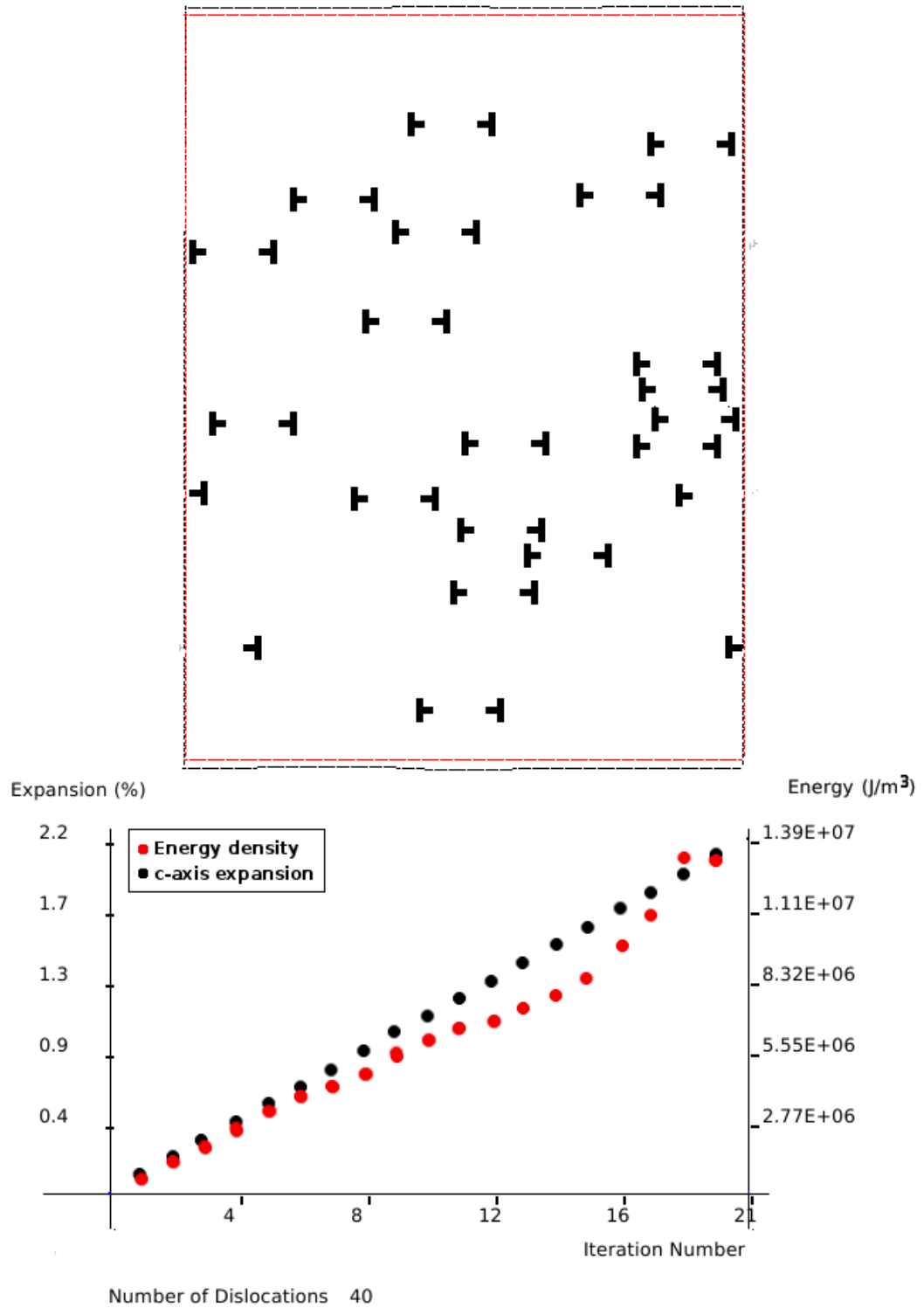


Figure 5.8: Example sequence of outputs from DD2D run for 800×600 cell
3) Iteration 40 showing 40 prismatic dislocation dipoles

Upper image displays geometry of dislocations within the 2-D crystal
red/black outline describes unstrained/strained crystal boundary

Lower image displays plotted points of the energy and c-axis expansion vs iteration

compared to the dashed red line showing the demarcation of the unstrained cell.

An option *Calculate energy* can be used to calculate and display the current energy after each iteration. The values are displayed on the same plot as that of the c-expansion as shown in, for example, the lower half of Fig 5.6.

A sequence of three outputs taken at arbitrary points during a DD2D run are displayed in Figs 5.6-5.8. The first of these images shows a dislocation dipole introduced into the plane. The following images show the effects of the expansion of the plane in the vertical direction, representing c-axis expansion, and the increase in energy with the introduction of greater numbers of dislocation dipoles. The c-axis expansion is seen to increase linearly while the energy increases in a more complicated manor.

5.1.8 Boundary Conditions

The DD2D model has been implemented using boundary conditions of repeated cells. The repeated cells are along the horizontal direction when looking at the visualisation of the model *i.e.* perpendicular to the prismatic direction. An identical copy of the dislocation types and positions contained in the particular model is repeated equally in each direction by an amount specified. The first repeat cells for a single prismatic dislocation dipole are shown in Fig 5.9.

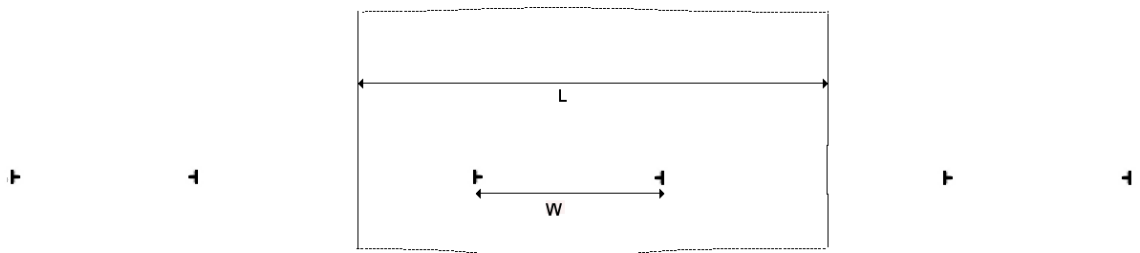


Figure 5.9: Prismatic dipole with repeat images

The two measurements of displacement and energy are shown to converge in the model when the number of repeat cells is increased sufficiently. The displacement

for prismatic dislocations only affects the prismatic direction. Convergence to a result published by Lehto and Öberg [156] is found.

The Lehto paper is a study of the effects of dislocation strain fields when periodic boundary conditions are used in supercell calculations. The aim of the paper is to develop “a general and self-consistent method to construct unit cells containing dislocations”. This requires translational invariance of the unit cell so that the structure can be multiplied out in all directions for a three dimensional model.

The translational vectors \mathbf{c}_i for the three spatial directions are the dimensions of a dislocation free unit cell. The translational vectors for the unit cell containing dislocations is related to the dislocation free vectors by $\mathbf{c}'_i = \mathbf{c}_i + \Delta\mathbf{c}_i$ where

$$\Delta\mathbf{c}_i = -\mathbf{b} \int_A \frac{\mathbf{c}_i \cdot d\mathbf{A}}{|\mathbf{c}_1 \cdot (\mathbf{c}_2 \times \mathbf{c}_3)|} \quad (5.1)$$

In Eq 5.1 \mathbf{b} is the Burgers vector and the term $d\mathbf{A}$ is an infinitesimal of surface area terminated by dislocation line with direction vector normal to the surface .

For the case of the DD2D model the prismatic translational vector represented by \mathbf{c}_3 is the only applicable calculation. In the two dimensional model with infinite straight dislocation lines the Equation 5.1 can be written simply as the magnitude of the Burgers vector multiplied by the fraction of the length of the material by the width of the cell

$$\Delta\mathbf{c}_3 = \frac{bW}{L} \quad (5.2)$$

where W is the length of material terminated by the prismatic dislocation dipole lines and L the width of the cell. Figure 5.9 shows W and L for a prismatic dislocation dipole.

The plots in Fig 5.10 show the effects of increasing the number of image cells for a prismatic dislocation dipole. The plot in Fig 5.10 (a) shows the convergence of energy/volume. The increase by percentage in the c direction compared to the dislocation free cell is shown in Fig 5.10 (b).

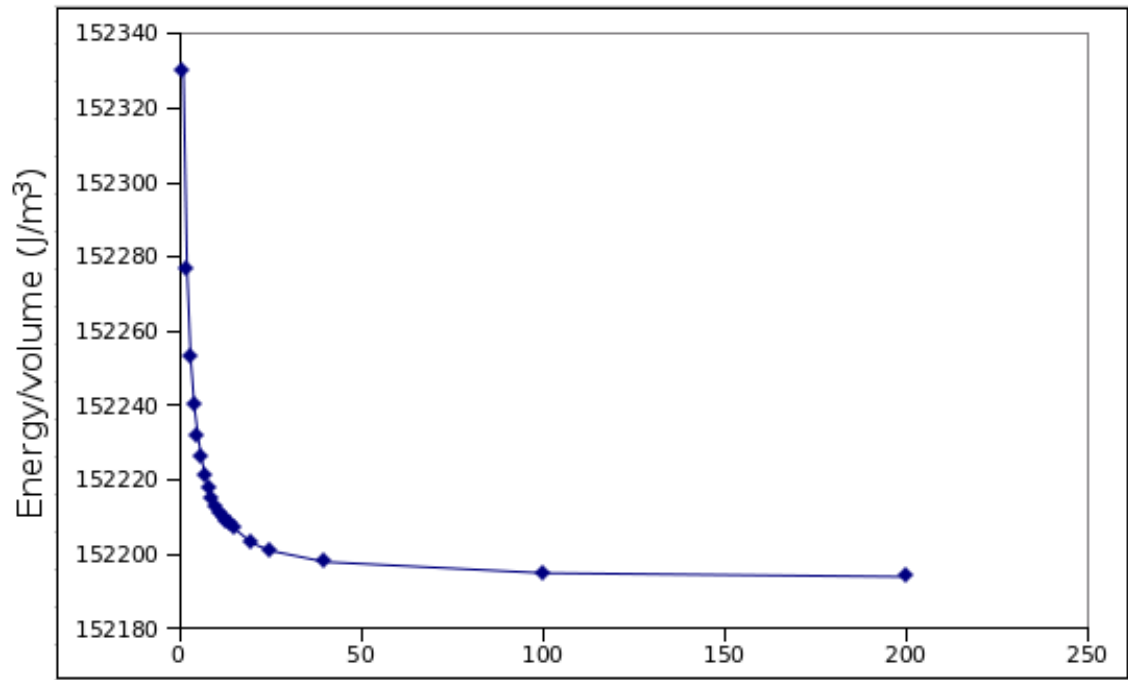
Taking values of $b = 6.64 \text{ \AA}$, $W = 80 \text{ \AA}$ and $L = 1200 \text{ \AA}$ for the Lehto expression of Eq 5.2 gives a value $\Delta c_3 = 0.443$. The results from the DD2D model are seen to converge to this value in Fig 5.10 (b).

5.1.9 Displacement and energy

The displacement and energy as used in the model have been described in Chapter 2.5. Both anisotropic and isotropic versions have been implemented. The anisotropic theory more accurately describes the expansion of a material which is highly anisotropic. The model implements two-dimensional plane strain for which exact solutions are known describing both displacements and energies in the anisotropic and isotropic theories.

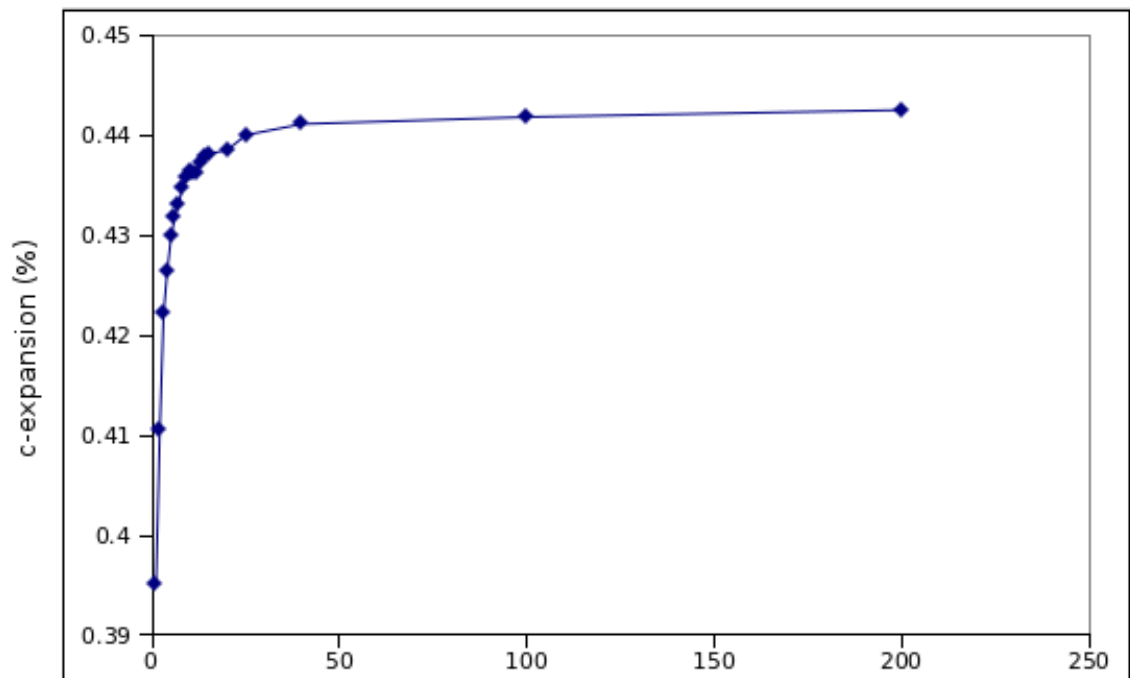
For both cases, isotropic and anisotropic, the energies are made up of a contribution from interaction energy and a contribution from self energy. The isotropic displacements used in the code are from Eq 2.83. The isotropic energy is from the hollow core and free surface model Eq 2.87. The anisotropic displacements used in the program are from Eq 2.119. These are coupled with the expressions for the anisotropic self energy from Eq 2.120 and interaction energy of Eq 2.124.

The self energy increases at a constant rate with increase of dislocations to a system. This is not the case for the interaction energies. Each dislocation interacts with any other dislocations in the model. The strength of the interaction energies change as a function of the position of other dislocations. There is an increase in internal energy for similar Burgers vectors or decrease for opposite Burgers vectors. As the density of dislocations increases the interaction energy combined with the self energy increases. At a certain density the total internal energy can be seen to level off or even begin to decrease in magnitude. At this point the interaction energy is reducing the total energy of the system. This cannot happen to the energy provided by the self energy as it is always positive. This feature can be seen as a saturation level of dislocations and as an indication of melting, see for example [157, 158].



(a)

Number of repeat cells



(b)

Number of repeat cells

Figure 5.10: (a) Energy/volume for increasing image cells
(b) Percentage increase in *c* direction for increasing image cells

5.1.10 Method

Once the initial starting conditions for the model have been specified by the user input options as described in Section 5.1.7 the program can be executed. Prismatic dislocation dipoles are introduced one pair at a time into the predefined area being modelled. The location of a pair is chosen using a randomly generated x position for one of the dislocations. The y position is randomly chosen from a position representing a horizontally aligned layer. The dislocation Burgers vector sign is also chosen randomly. To create the dipole an oppositely signed dislocation will be introduced at a set horizontal distance along the plane from its pair. Depending on the sign of the first dislocations Burgers vector its pair will be placed to either the left or right.

If the situation occurs that the dislocation should be placed outside of the limit defined by the boundary the second dislocation will be placed at the appropriate distance from the opposite boundary. This is equivalent to the dislocation passing through one boundary of a cell and reentering the cell smoothly at the opposite boundary. This is a result of the boundary conditions applied to the model.

Another consideration built into the program is that the placement of the dislocations cannot occur within an exclusion zone denoted by a specified distance from the dislocation coordinates. This value has been set to the magnitude of 1 Burgers vector $|b| = 6.64 \text{ \AA}$. This is so as not to allow the dislocations to be created coincidentally with another. If random dislocation coordinates for a new dislocation are coincident with one already existing a new random position will be found. This operation is repeated if the following position is also occupied within the bounds of the exclusion zone until an unoccupied position has been located.

For each dislocation introduced into the model an identical dislocation is placed into any repeat cell horizontally aligned either side of the original cell. The number of repeat cells is currently defined within the program. The size of the repeat cell used is 8 to both the left and right of the initial cell.

The model is filled with the required number of dislocations for one iteration

in the manner described above. Having completed this step the displacement is calculated. The displacement calculation is the same for each dislocation as described in Section 5.1.9. The sum of all displacements gives the expansion resulting from one iteration. The total displacement for the particular iteration is then plotted.

Following the displacement routines the energy is calculated. The energy is calculated as described in Section 5.1.9. The energy is plotted and copies of the displacement/energy plot and the visualisation of the positions of the model are saved in two separate files. This procedure is repeated at the end of each iteration.

The process of dislocations being introduced and displacements and energies being calculated as described above occurs until the number of chosen iterations have been completed.

5.1.11 Results

A selection of output images showing the results from a group of runs using the DD2D program will be shown in this section. The runs were executed using various different parameters and scales as discussed below.

All runs were undertaken using eight image cells either side of the primary cell. The size of the exclusion zone was held constant at 6.64 \AA .

For each particular set of parameters, as listed below, the code was run using three model sizes,

1. a single line modelling one graphene layer 1200 \AA wide
2. a two dimensional model $500 \times 500 \text{ \AA}^2$
3. a two dimensional model $600 \times 800 \text{ \AA}^2$

In addition a larger cell size of $1200 \times 1600 \text{ \AA}^2$ was used for one run.

The single line model was run at a rate of 2 *dislocations/iteration*, *i.e.* one dipole per iteration. The remaining area sizes were run using a rate of 200 *dislocations/iteration*.

The parameters that have been altered for subsequent runs include the magnitude of the Burgers vector b . The size of the initial cell along each side in units of Å *i.e.* area $a = (x \times y) \text{ \AA}^2$. The horizontal distance between dislocation dipoles, d , measured in units of Å.

The results displayed in Fig 5.11 were from a DD2D run using a Burgers vector size of $b = 6.64 \text{ \AA}$, a dipole separation of $d = 30 \text{ \AA}$ and an area of $1200 \times 6.64 \text{ \AA}^2$. The image shows a constant gradient increase of c-axis expansion with constant rate of dislocations introduced to the model.

The energy density can be seen to increase quite regularly, albeit with some fluctuation, with the constant rate of dislocations added until it reaches the stage ringed in blue in Fig 5.11. The energy is then seen to fluctuate with dips and then increases but the rate of increase does not continue as it did before this point. The self energy of the dislocations must always increase as positive energy is placed into the system. If an energy dip occurs it is because the interaction energy introduced to the system is greater than the added self energy. This effect has been described by Cotterill [157] as the point when a system makes the transition from a two-dimensional solid state to a two-dimensional liquid state. Burakovsky [158] has calculated such a melting point in a two dimensional solid to have a dislocation density of

$$\rho_m = (0.61 \pm 0.02)b^{-2} \quad (5.3)$$

where the units are the reciprocal of the magnitude of the particular Burgers vector squared.

The limits of the region where melting is expected to take place, according to the Burakovsky parameters Eq 5.3, has been highlighted in Fig 5.11 using two vertical blue lines. This is within the melting zone predicted. It should be noted that the gradient of the c-expansion remains constant throughout.

Figure 5.12 results were generated using a Burgers vector magnitude of $b = 6.64 \text{ \AA}$, the dipole separation used was $d = 60 \text{ \AA}$ and the area of the cell

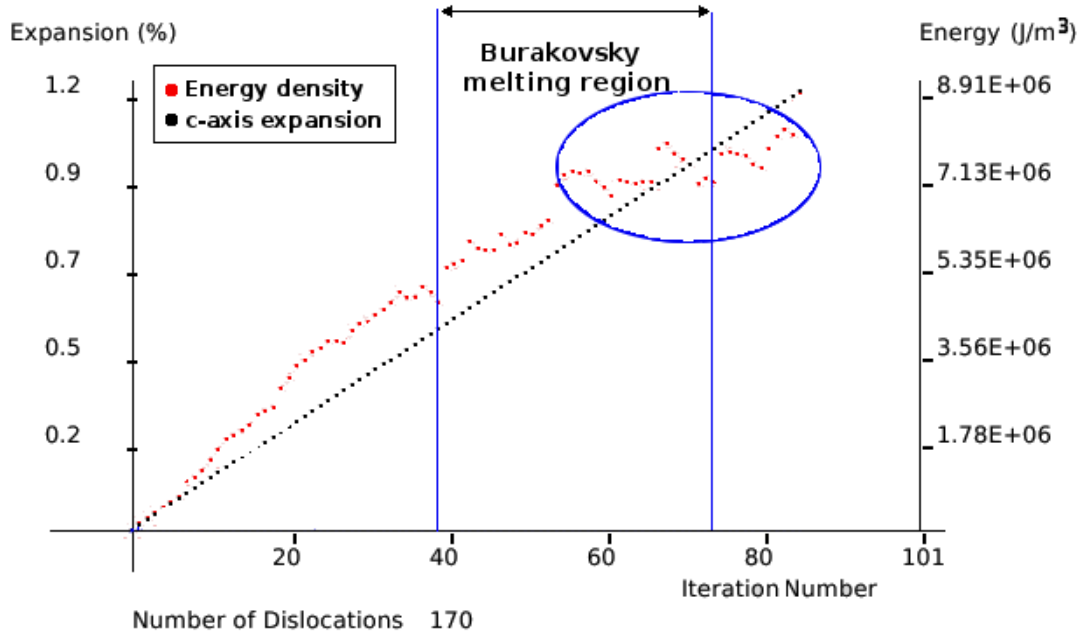


Figure 5.11: DD2D run with Burgers vector magnitude $b = 6.64 \text{ \AA}$, dipole separation $d = 30 \text{ \AA}$ and area $a = 1200 \times 6.64 \text{ \AA}^2$. Two dislocations introduced per iteration. Total number of dislocations: 170. Burakovsky melting region is indicated between blue lines marked by arrows.

$$a = 500 \times 500 \text{ \AA}^2.$$

The results shown in Fig 5.13 were calculated using a Burgers vector magnitude of $b = 6.64 \text{ \AA}$, dipole separation of $d = 30 \text{ \AA}$ and cell area $a = 1200 \times 1600 \text{ \AA}^2$.

It can be seen for all of the runs that the displacement increases linearly with the introduction of dipoles at a continuous rate. The gradient can be increased or decreased by altering the width of dislocation dipole separation d but always remains constant. This is the desired result as the dipole separation d corresponds to the amount of additional material being placed into the crystal per dipole as described in Sec 5.1.6.

The energy does not increase with such regularity. The range where the energy tails off has been circled in blue for each of the images Figs 5.11 - 5.13. This result is in line with the predicted melting density of dislocations Eq 5.3 made by Burakovsky.

The results of this model can be seen as a proof of concept. The two-dimensional

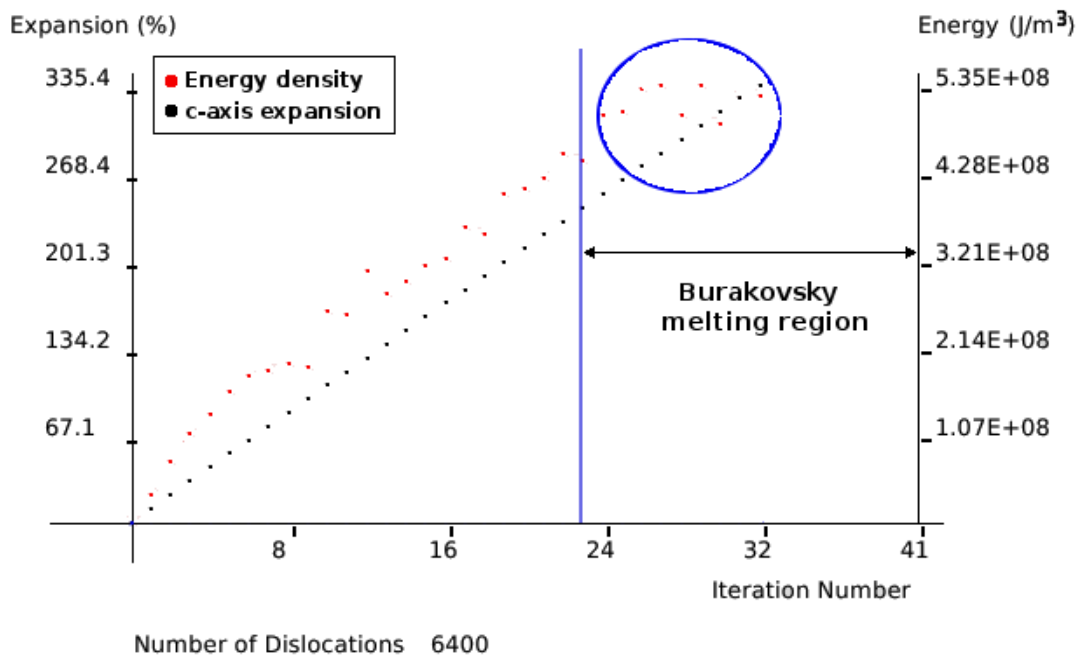


Figure 5.12: DD2D run with Burgers vector magnitude $b = 6.64 \text{ \AA}$, dipole separation $d = 60 \text{ \AA}$ and area $a = 500 \times 500 \text{ \AA}^2$. 200 dislocations introduced per iteration. Total number of dislocations: 6400. Beginning of Burakovsky melting region is indicated by blue line. The zone showing energy density dipping is circled in blue.

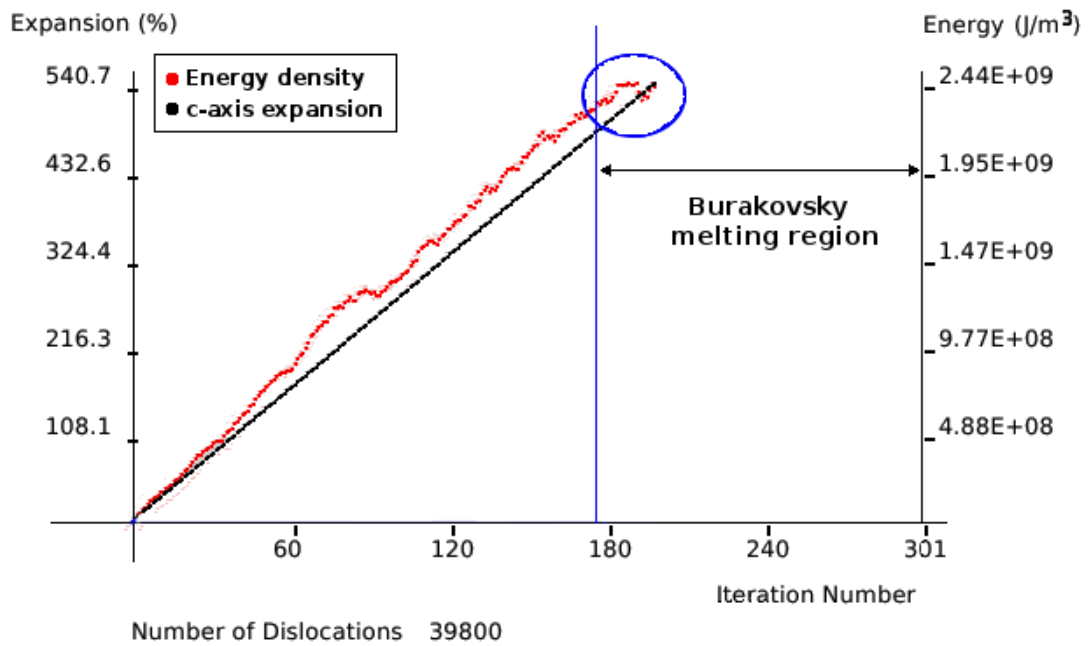


Figure 5.13: DD2D run with Burgers vector magnitude $b = 6.64 \text{ \AA}$, dipole separation $d = 60 \text{ \AA}$ and area $A = 1200 \times 1600 \text{ \AA}^2$. 200 dislocations introduced per iteration. Total number of dislocations: 39800. Beginning of Burakovsky melting region is indicated by blue line. The zone showing energy density dipping is circled in blue.

prismatic dislocation dipole model can be used to simulate expansion of the c-axis as seen in irradiated graphite. The DD2D is a simple model that has been shown to work in this respect. It is also a way of modelling at the macroscopic level rather than the microscopic level thereby giving predictions that are more readily tested against experimental evidence on a scale larger than the atomic level.

It is hoped that future work will combine the basal and prismatic dislocations into one model that can explain more of the details seen in neutron irradiation in graphite. The basal dislocations will be responsible for transporting material around the crystal. Pileups of basal dislocations will be represented using prismatic dislocations which will drive the c-axis expansion.

Another area will need to be developed to provide a more realistic model. Currently extra material is introduced into the model but no account is taken of the relocation of that material from other areas of the crystal. For the sake of conservation of material this must be taken into account. With this feature would come a way of explaining the a-axis shrinkage seen in irradiated graphite samples that is not currently covered in the DD2D model.

Graphite in nuclear moderators does not consist of one large crystal of pure hexagonal graphite, as implied by the DD2D model, but is made up of randomly oriented crystals of graphite. This feature could be a future development to be incorporated into the two-dimensional model. This would involve randomly orienting crystals and aligning them with other crystals with appropriate boundary conditions.

Chapter 6

Conclusion

The study of this thesis has been concerned with the properties of graphite. The two areas studied have been, firstly, the elastic properties of pure hexagonal graphite and bromine intercalated graphite and, secondly, dislocation theory applied to irradiated graphite.

A study of the elastic constants of hexagonal graphite using DFT with LDA has been undertaken using the AIMPRO code. The calculations have described the total and partial elastic constants of the five second order and 10 third order independent elastic constants. A high k-point mesh of $72 \times 72 \times 26$ coupled with a *pddd*p basis set has given well-converged results. The results presented are the first to use these parameters to optimise and then calculate the single point energies over the strained lattices. These are also the first results to show the contributions of internal strain to the third order elastic constants using DFT with LDA.

The study of the third order elastic constants could be taken further. The results of the current calculations are a representation of the combined internal elastic constants for the given strains. Using appropriate combinations of homogeneous strains the full array of internal elastic constants could be extracted and represented individually.

The zero point energy contribution to the hexagonal graphite elastic constant C_{33} has been calculated using vibrational mode DFT with LDA results from Haffenden. The anharmonic contribution to C_{33} has also been calculated from

the vibrational mode data. The vibrational mode data has also been used in the calculation for the interlayer separation of hexagonal graphite. The result for the combination of LDA SPE and ZPE with LJ [6 – 12] at 300 K gave a separation $D = 3.37 \text{ \AA}$ in excellent agreement with experimental data.

Lennard-Jones [5 – 10] and [6 – 12] models were combined with the LDA SPE results to model hexagonal graphite binding energy. The LJ [6 – 12] model combined with the LDA SPE results gave a binding energy of $BE = -51 \text{ meV/atom}$ in agreement with a recent experimental study [83]. To apply the ZPE and temperature effects to the binding energy requires further vibrational mode calculations to be performed. The results used in this thesis are suitable for the calculation of elastic constants and interlayer separation effects where relative energy differences are suitable. For the binding energy absolute energies are needed.

The elastic constant C_{33} , C_{44} and C_{55} have been studied for stage-1 and stage-2 intercalated graphite compounds. These are the first to be reported using DFT with LDA. The energies were well defined and should be interpreted as correct for DFT with LDA within a margin of error. They indicate that the results for C_{33} are somewhat lower than that for hexagonal graphite as would be expected.

More information concerning the interlayer binding mechanism could be investigated using band structure calculations available in AIMPRO and imaging of the molecular orbitals using AIMVIEW an extension package for AIMPRO. A further study could also be undertaken to calculate the full array of second and third order elastic constant values of bromine intercalated graphite. Also various other unit cell arrangements with varying bromine densities and staging could be taken into consideration.

A dislocation dynamics model has been created in collaboration with Pippa Young. Various runs of the model have been carried out modelling the response of graphite, modelled as a continuum, to dose. The prismatic dislocation model describes the c expansion using anisotropic elastic displacement fields. The internal energy has been modelled using anisotropic self energy coupled with the interaction

energy of the dislocation fields.

The results of the simulations show a shielding of energy for high dislocation density. This comes from the interaction energy of dislocations entered into the system having lower energy than the always positive self energy contributions. This is in broad agreement with data. The density of dislocations when the effects of the shielding are most obviously seen to coincide with the value of $0.61/b^2$ in agreement with the [158] study.

It has been shown that two-dimensional dislocation theory is a suitable framework for modelling irradiation effects in graphite. Although this is a simple model it shows scope for development and potential to solve some of the problems that have not been properly addressed by the interstitial standard model.

The model is still under development. It is hoped that basal dislocations will be incorporated within the current prismatic model. With suitable boundary conditions applied a number of variously aligned crystals in a two dimensional array could be modelled. This could lead to a more realistic modelling of irradiated graphite within a reactor environment where the randomly oriented crystallites form a highly isotropic macroscopic material. Non periodic boundary conditions would also allow the modelling of basal contraction of the crystallites which is missing in the current program.

Appendix A

Lennard-Jones Script

Octave script, LJ.m, used for Lennard-Jones calculations in Chapter 3. Can be run using a run script similar to that shown in Appendix B.

LJ.m

```
function[LJE]=LJ(strain)

%
% Calculate LJ interactions for graphite
%
% To run:
% open octave in shell [i.e. inside shell type: octave]
% type: LJ(strain)
% where strain is an integer [e.g. LJ(0.1) for calculation at 10% strain]
%
% Returns a value LJE for the Lennard-Jones energy depending on parameters used
% and atom positions specified
%
output_precision(9);
% set output precision required
% zero variables for first iteration
LJEtmp=0;
```

```
LJCurrent1=0;
LJCurrent2=0;
%
% cut: horizontal cut off radius for calculation [adjust as required]
cut=36.000;
%
% num: number of atoms in reference layer
num_atoms=5208;
%
% sep: 2xinterlayer separation. To increase separation
% between reference atoms and double layer
sep=2*3.32358502659;
%
% R0: vdW radius
R0=7.05;
% power values in LJ [e.g. P1=6, P2=12 for LJ 6-12 potential]
P1=6;
P2=12;
% epsilon: energy coefficient [Ha]
epsilon=0.0000324;
% positions for alpha and beta reference atoms [adjust as required]
% alpha atom:
alpha=[42.32211467872, 36.69428817675, -3.32358502659];
% beta atom:
beta=[40.91137752277, 36.69428817675, -3.32358502659];
% load atom positions to data1
%[atom_pos.dat: file of atom positions in columns of format: x y z
% where x,y,z are integers in chosen units]
data1=load("atom_pos.dat");
```

```

%%
% ralpha, rbeta: measure atom-atom distance from alpha and beta
% reference atoms to particular atom
% j: count over number of double layers required
%
for j=1:15
    for i=1:num_atoms
        % calculate the atom-atom distance
        ralpha=sqrt((alpha(1)-data1(i,1))^2+(alpha(2)-data1(i,2))^2+(alpha(3)...
            -(data1(i,3)+(j-1)*sep)*(1+strain))^2);
        rbeta=sqrt((beta(1)-data1(i,1))^2+(beta(2)-data1(i,2))^2+(beta(3)...
            -(data1(i,3)+(j-1)*sep)*(1+strain))^2);
        % LJ energy calculation
        if(sqrt((alpha(1)-data1(i,1))^2+(alpha(2)-data1(i,2))^2)<cut)
            LJEcurrent1=-4*epsilon*((R0/ralpha)^P1-(R0/ralpha)^P2);
        endif;
        if(sqrt((beta(1)-data1(i,1))^2+(beta(2)-data1(i,2))^2)<cut)
            LJEcurrent2=-4*epsilon*((R0/rbeta)^P1-(R0/rbeta)^P2);
        endif;
        LJEcurrent=LJEcurrent1+LJEcurrent2;
        % add new value to LJE
        LJE=LJEcurrent+LJEtmp;
        LJEtmp=LJE;
        % reset LJEcurrent
        LJEcurrent1=0.;
        LJEcurrent2=0.;
    end
end
end

```

Appendix B

Lennard-Jones run file

Example run file for LJ.m as shown in [Appendix A](#)

```
runLJ.m
```

```
function[x]=runLJ
```

```
% example of a run script to be used with LJ.m
```

```
%
```

```
% open octave in shell
```

```
% to run type: runLJ
```

```
clear;
```

```
% str_min: use as zero binding-energy reference point [adjust as needed]
```

```
str_min=LJ(20);
```

```
% conv: conversion factor [adjust as needed]
```

```
conv=6802.90620152929;
```

```
% strain values as required
```

```
str1=[
```

```
-0.2  
-0.15  
-0.1  
-0.05  
0.0  
0.05  
0.1  
0.15  
0.2  
];
```

```
% call LJ.m to perform calculations
```

```
for i=1:9
```

```
ens1(i)=(LJ(str1(i))-str_min)*conv;
```

```
end
```

```
ens=ens1';
```

```
% save results as a column of values in file out.dat
```

```
save out.dat ens
```

List of Figures

2.1	(a)Graphene electron bands at K (b)Graphene bilayer bands at K for AB	15
2.2	Basal direction view (top row) and c-axis view (bottom row) of wave functions at K for graphene bilayer.[19] Iso-surfaces of positive phase wavefunctions are shown in red while negative phase iso-surfaces are shown in blue. (a) $(\alpha_1 + \alpha_2)$ In phase wavefunctions leading to interlayer binding (b) and (c) Non interacting, out of phase wavefunctions (d) $(\alpha_1 + \alpha_2)$ Opposite phase, anti binding wavefunctions	16
2.3	Transformation of axes [22]	20
2.4	Shear on an area element [26]	23
2.5	Stress on an infinitesimal cube [25]	24
2.6	The relative displacement of two sublattices: L_α and L_β (a) Interlattice vector $\mathbf{r}_0^{\alpha\beta}$ in the undeformed state (b) Homogeneous strain J causes no internal strain (c) $\delta^{\alpha\beta}$ has magnitude and direction equal to the displacement of the points relative to the homogeneous strain positions $J\mathbf{r}_0^{\alpha\beta}$ [30]	32
2.7	Frenkel model used to calculate the required shear stress σ for moving one atomic later over another [26] a interlayer spacing b intralayer spacing	35
2.8	Edge dislocation moving by glide along a slip plane [26]	36

2.9	(adapted from [25]) (a) Shear applied to perfect crystal (b) Dislocation moves from left to right leaving slip step to left (c) Dislocation leaves slip step to right on leaving crystal	37
2.10	Burgers circuit [25] (a), (b) begin by creating a path around the deformation (a). This is then repeated in the perfect crystal (b). The Burgers vector is the vector closing the circuit from finish (F) to start (S) (c), (d) a path is drawn inside the perfect crystal (a). This path is then taken around the crystal containing the deformation (b). The Burgers vector, in this case, is the vector pointing from start (S) to finish (F).	39
2.11	Screw dislocation with radius R perpendicular and Burgers vector \mathbf{b} horizontal to the line vector ξ [25]	41
2.12	Edge dislocation with radius r and Burgers vector \mathbf{b} perpendicular to the line vector ξ [25]	43
2.13	A dislocation loop within a crystal	49
2.14	Coordinate system for hexagonal graphite with line direction ξ parallel to z	52
3.1	Hexagonal graphite primitive unit cell	58
3.2	The stacking formation of three allotropes of graphite [57] (a) Hexagonal (Bernal) AB s (b) Rhombohedral ABC stacking (c) AA stacking	59
3.3	Energy per unit cell volume vs strain	67
3.4	Anharmonic contribution to C_{33} vs strain	71
3.5	Anharmonic contribution to C_{33} in hex graphite vs temperature	73
3.6	Binding energy vs interlayer separation (a) DFT with LDA Single Point Energy (SPE) (b) DFT with LDA SPE, ZPE and LJ [5–10] and LJ [6–12] (current work) (c) Spanu [87] using Quantum Monte Carlo	80
4.1	(a) $C_{18}Br_2$ unit cell (b) $C_{36} - Br_2$ unit cell	83

5.1	Bending, breaking and cross connecting of the graphene planes[110]. Left hand images are basal plane traces of right hand images	87
5.2	(a) Graphite irradiated to 10^{20} n/cm^2 at $30^\circ C$ (b) Graphite irradiated to 8×10^{20} n/cm^2 at $50^\circ C$ [115]	89
5.3	Changes of the 0002 x-ray line with increasing dose [122]	89
5.4	The four fundamental dislocation types of graphite. Adapted from [152]	92
5.5	(a) Ruck and tuck (b) Wrinkle dislocations shown in red dislocation dipole separation d	94
5.6	Example sequence of outputs from DD2D run for 800×600 cell 1) First iteration showing single prismatic dislocation dipole Upper image displays geometry of dislocations within the 2-D crystal red/black outline describes unstrained/strained crystal boundary Lower image displays plotted points of the energy and c-axis expansion vs iteration	96
5.7	Example sequence of outputs from DD2D run for 800×600 cell 2) Iteration 10 showing 10 prismatic dislocation dipoles Upper image displays geometry of dislocations within the 2-D crystal red/black outline describes unstrained/strained crystal boundary Lower image displays plotted points of the energy and c-axis expansion vs iteration	97
5.8	Example sequence of outputs from DD2D run for 800×600 cell 3) Iteration 40 showing 40 prismatic dislocation dipoles Upper image displays geometry of dislocations within the 2-D crystal red/black outline describes unstrained/strained crystal boundary Lower image displays plotted points of the energy and c-axis expansion vs iteration	98
5.9	Prismatic dipole with repeat images	99
5.10	(a) Energy/volume for increasing image cells (b) Percentage increase in c direction for increasing image cells	102

- 5.11 DD2D run with Burgers vector magnitude $b = 6.64 \text{ \AA}$, dipole separation $d = 30 \text{ \AA}$ and area $a = 1200 \times 6.64 \text{ \AA}^2$. Two dislocations introduced per iteration. Total number of dislocations: 170 Beginning of Burakovsky melting region is indicated between blue lines marked by arrows. 106
- 5.12 DD2D run with Burgers vector magnitude $b = 6.64 \text{ \AA}$, dipole separation $d = 60 \text{ \AA}$ and area $a = 500 \times 500 \text{ \AA}^2$. 200 dislocations introduced per iteration. Total number of dislocations: 6400 Beginning of Burakovsky melting region is indicated by blue line. The zone showing energy density dipping is circled in blue. 107
- 5.13 DD2D run with Burgers vector magnitude $b = 6.64 \text{ \AA}$, dipole separation $d = 60 \text{ \AA}$ and area $A = 1200 \times 1600 \text{ \AA}^2$. 200 dislocations introduced per iteration. Total number of dislocations: 39800 Beginning of Burakovsky melting region is indicated by blue line. The zone showing energy density dipping is circled in blue. 108

List of Tables

2.1	Symmetry of the Second and Third Order Elastic Constants of Hexagonal Graphite	30
2.2	Δ_{ij} and Δ_{ijk} terms for hexagonal graphite	34
3.1	Lattice Parameters of Hexagonal Graphite	64
3.2	Combinations of second and third order elastic constants for various strains	66
3.3	Hexagonal Graphite: 2 nd order elastic constants [GPa] (C_{xx} denotes total elastic constant, C_{xx}^0 partial elastic constant, Δ_{xx} internal contribution to the elastic constant) (a) Savini <i>et al.</i> [72] (b) Michel and Verbeck [70] (c) Bosak <i>et al.</i> [68] (d) Mounet and Marzari [16] (e) Cousins and Heggie [46] (f) Blackslee <i>et al.</i> [60] (g) Grimsditch [64]	68
3.4	Hexagonal Graphite: 3 rd order elastic constants [GPa] Cousins' results are from a modified Keating model. (C_{xxx} denotes total elastic constant, C_{xxx}^0 partial elastic constant, Δ_{xxx} internal contribution to the elastic constant)	69
3.5	Interlayer separation LDA SPE with ZPE using LJ [5 – 10] and [6 – 12] models at 300 K and LDA SPE with LJ [5 – 10] and [6 – 12] models at 0 K	73
3.6	Binding energy results from experiment (expt) and theory	78
4.1	Elastic constant values (GPa) for Br_2 intercalated graphite	84

Bibliography

- [1] G. Haffenden. *First Principles Calculations of the Spectroscopic and Thermal Properties of Graphitic Materials*. DPhil thesis, School of Life Sciences, 2009.
- [2] L. Luyken, M. Schmidt, A. N. Jones, B. Marsden, and T. J. Marrow. Simulating material property changes of irradiated nuclear graphite. Presentation, UNTF, 2010.
- [3] P. R. Briddon and R. Jones. LDA Calculations Using a Basis of Gaussian Orbitals. *phys. stat. sol. (b)*, 217:131, 2000.
- [4] Patrick Briddon and M. J Rayson. Accurate Kohn-Sham DFT with the speed of tight binding: Current techniques and future directions in materials modelling. *phys. stat. sol. (b)*, 248(6):1309–18, 2010.
- [5] Patrick Briddon and R. Jones. LDA Calculations Using a Basis of Gaussian Orbitals. *phys. stat. sol. (b)*, 217(1):131–171, 2000.
- [6] F. Jensen. *Introduction to Computational Chemistry*. Wiley, Chichester, 1999.
- [7] P. Hohenberg and W. Kohn. Inhomogeneous electron gas. *Phys. Rev. B*, 136, 1964.
- [8] W. Kohn and L. J. Sham. Self-consistent equations including exchange and correlation effects. *Phys. Rev.*, 140(4A):A1133–A1138, Nov 1965.
- [9] John P. Perdew and Yue Wang. Accurate and simple analytic representation

- of the electron-gas correlation energy. *Phys. Rev. B*, 45(23):13244–13249, Jun 1992.
- [10] John P. Perdew, Kieron Burke, and Matthias Ernzerhof. Generalized gradient approximation made simple. *Phys. Rev. Lett.*, 77(18):3865–3868, Oct 1996.
- [11] C. Hartwigsen, S. Goedecker, and J. Hutter. Relativistic separable dual-space Gaussian pseudopotentials from H to Rn. *Phys. Rev. B*, 58(7):3641–3662, August 1998.
- [12] G. B. Bachelet, D. R. Hamann, and M. Schlüter. Pseudopotentials that work: from H to Pu. *Phys. Rev. B*, 26(8):4199–4228, 1982.
- [13] N. Troullier and J. L. Martins. Efficient pseudopotentials for plane-wave calculations. *Phys. Rev. B*, 43(3):1993–2006, 1991.
- [14] H. J. Monkhorst and J. D. Pack. Special points for Brillouin-zone integrations. *Phys. Rev. B*, 13(12):5188–5192, June 1976.
- [15] P. Pulay. Ab initio calculation of force constants and equilibrium geometries in polyatomic molecules. I. theory. *Mol. Phys.*, 17:197, 1969.
- [16] N. Mounet and N. Marzari. First-principles determination of the structural, vibrational and thermodynamic properties of diamond, graphite, and derivatives. *Phys. Rev. B*, 71(20), MAY 2005.
- [17] M.I. Heggie. Private communication.
- [18] J. C. Charlier, X. Gonze, and J. P. Michenaud. First-principles study of the stacking effect on the electronic properties of graphite(s). *Carbon*, 32:289–299, 1994.
- [19] C. Davidson. *Looking Ahead to Computer-Controlled Molecular Assembly*. DPhil thesis, School of Life Sciences, 2011.

- [20] M. Born and K. Huang. *Dynamical Theory of Crystal Lattices*. Oxford University Press, New York, 1954.
- [21] B. T. Kelly and M. Eslick. Zero-point energy corrections to the interlayer spacing and the c_{33} elastic constant of graphite. *Carbon*, 13:43–45, June 1974.
- [22] A. H. Love. *A Treatise on the Mathematical Theory of Elasticity*. Cambridge University Press, 1934.
- [23] L. D. Landau & E. M. Lifshitz. *Theory of Elasticity*. Pergamon Press, Oxford, 1975.
- [24] S. Timoshenko & J. N. Goodier. *Theory of Elasticity*. McGraw-Hill, New York, 1951.
- [25] J. P. Hirth & J. Lothe. *Theory of Dislocations*. Krieger Publishing Company, Malabar, Florida, 2nd edition, 1982.
- [26] D. Hull & D. J. Bacon. *Introduction to Dislocations*. Butterworth Heinemann, Oxford, 4th edition, 2001.
- [27] C. S. G. Cousins. Formal elasticity of four carbon allotropes: II. the anatomy of the macroscopic elastic constants, compliances, and pressure derivatives and a generalized method of homogeneous deformation. *Journal of Physics: Condensed Matter*, 14(20):5115, 2002.
- [28] T. (Ed.) Hahn. *International Tables for X-ray Crystallography*. John Wiley & Sons, 2005.
- [29] C. S. G. Cousins. Formal elasticity of four carbon allotropes: I. the inner elastic constants, internal strain tensors, and zone-centre optic mode frequencies and their pressure dependences. *Journal of Physics: Condensed Matter*, 14(20):5091, 2002.

- [30] C. S. G. Cousins. Inner Elasticity. *Journal Of Physics C-Solid State Physics*, 11(24):4867–4879, 1978.
- [31] C. S. G. Cousins. Symmetry Of Inner Elastic-Constants. *Journal Of Physics C-Solid State Physics*, 11(24):4881–4900, 1978.
- [32] T. H. K. Barron and R. W. Munn T. G. Gibbons. Thermodynamics of internal strain in perfect crystals. *Journal of Physics*, 4:2805, 1971.
- [33] F. R. N Nabarro. *Theory of Crystal Dislocations*. Oxford University Press, London, 1967.
- [34] A. H. Cottrell. *Dislocations and Plastic Flow in Crystals*. Oxford University Press, London, 1956.
- [35] O. Mugge. *Neues Jahrb. Min.*, 13, 1883.
- [36] A. Ewing and W. Rosenhain. *Phil. Trans. Roy. Soc.*, A193, 1899.
- [37] V. Volterra. Sur l'équilibre des corps lastiques multiplement connexes. *Ann. Ecole Norm. Super.*, 24:401, 1907.
- [38] Ya. I. Frenkel and T. A. Kontorova. *Zh. Eksp. Teor. Fiz.*, 8:1340, 1938.
- [39] Tindler R. F. *J. Metals*, 16:94, 1964.
- [40] E. Orowan. Zur kristallplastizitt iii: ber die mechanismus des gleitvorganges. *Zeits. f. Physik*, 89:634, 1934.
- [41] M. Polanyi. Ueber eine art von gitterstörung, die einem. kristal plastisch machen konnte. *Z. Phys.*, 89:660, 1934.
- [42] G.I. Taylor. *Proc. Roy. Soc.*, A145:362, 1934.
- [43] R. Bullough B. A. Bilby and E. Smith. Continuous distributions of dislocations: A new application of the methods of non-riemannian geometry. *Proc. Roy. Soc. A*, 231(1185):263–273, 1955.

- [44] Burgers J. M. Some considerations on the fields of stresses connected with dislocations in a regular crystal lattice. *Kon. Ned. Akad.*, 42:293, 1939.
- [45] M. Peach and J. S. Koehler. The forces exerted on dislocations and the stress fields produced by them. *Phys. Rev.*, 80:436–439, Nov 1950.
- [46] C. S. G. Cousins and M. I. Heggie. Elasticity of carbon allotropes. iii. hexagonal graphite: Review of data, previous calculations, and a fit to a modified anharmonic Keating model. *Phys. Rev. B*, 67:024109, Jan 2003.
- [47] W. Shockley J. D. Eshelby, W. T. Read. Anisotropic elasticity with applications to dislocation theory. *Acta Metallurgica*, 1:251–259, May 1953.
- [48] A. J. E Foreman. Dislocation energies in anisotropic crystals. *Acta Metallurgica*, 3(4):322 – 330, 1955.
- [49] A. N. Stroh. Dislocations and cracks in anisotropic elasticity. *Philosophical Magazine*, 3(30):625–646, 1958.
- [50] G. B. Spence. Theory of extended dislocations in symmetry directions in anisotropic infinite crystals and thin plates. *Journal of Applied Physics*, 33:729, 1962.
- [51] Y. T. Chou. Interaction of parallel dislocations in a hexagonal crystal. *Journal of Applied Physics*, 33:2747, 1962.
- [52] L. J. Teutonico. Dynamical behavior of dislocations in anisotropic media. *Physical Review*, 124(4):1039, November 1961.
- [53] K. Maln. The analysis of the strain field of an edge dislocation when the anisotropy factor is negative. *Scripta Metallurgica*, 2(4):223 – 226, 1968.
- [54] J. C. Charlier, J. P. Michenaud, and P. Lambin. Tight-binding density of electronic states of pregraphitic carbon. *Phys. Rev. B*, 46:4540–4543, Aug 1992.

- [55] J. D. Bernal. The structure of graphite. *Proc. R. Soc. London, Ser. A*, 106(740):749–773, December 1924.
- [56] A. R. Ubbelohde & F. A. Lewis. *Graphite and its Crystal Compounds*. Clarendon Press, Oxford, 1960.
- [57] I. Surez Martnez. *Theory of diffusion and plasticity in layered carbon materials*. Phd thesis, Faculty of Chemistry, University of Sussex, United Kingdom, 2007.
- [58] QingYun Lin, TongQi Li, ZhanJun Liu, Yan Song, LianLong He, ZiJun Hu, QuanGui Guo, and HengQiang Ye. High-resolution tem observations of isolated rhombohedral crystallites in graphite blocks. *Carbon*, 50(6):2369 – 2371, 2012.
- [59] M. S. Dresselhaus and G. Dresselhaus. Intercalation compounds of graphite. *Advances in Physics*, 51(1):1–186, 2002.
- [60] O. L. Blakslee, D. G. Proctor, E. J. Seldin, G. B. Spence, and T. Weng. Elastic constants of compression-annealed pyrolytic graphite. *Journal of Applied Physics*, 41(8):3373–3382, 1970.
- [61] D. E. Soule and C. W. Nezbeda. Direct basal-plane shear in single-crystal graphite. *Journal of Applied Physics*, 39(11):5122–5139, 1968.
- [62] E. J. Seldin and C. W. Nezbeda. Elastic constants and electron-microscope observations of neutron-irradiated compression-annealed pyrolytic and single-crystal graphite. *Journal of Applied Physics*, 41(8):3389–3400, 1970.
- [63] M. Grimsditch. Surface brillouin scattering from graphite. *Physica Status Solidi B*, 193(k9), 1996.
- [64] M. Grimsditch. Shear elastic modulus of graphite. *J. Phys. C: Solid State Phys.*, 16(L143-L144), 1982.

- [65] R. Nicklow, N. Wakabayashi, and H. G. Smith. Lattice dynamics of pyrolytic graphite. *Phys. Rev. B*, 5:4951–4962, 1972.
- [66] B. T. Kelly. *High Temp. High Press.*, 13:245, 1981.
- [67] You Xiang Zhao and Ian L. Spain. X-ray diffraction data for graphite to 20 gpa. *Phys. Rev. B*, 40:993–997, Jul 1989.
- [68] Alexey Bosak, Michael Krisch, Marcel Mohr, Janina Maultzsch, and Christian Thomsen. Elasticity of single-crystalline graphite: Inelastic x-ray scattering study. *Phys. Rev. B*, 75:153408, Apr 2007.
- [69] Peter Trucano and Ruey Chen. Structure of graphite by neutron diffraction. *Nature*, 258:136, 1975.
- [70] K. H. Michel and B. Verberck. Theory of the evolution of phonon spectra and elastic constants from graphene to graphite. *Phys. Rev. B*, 78:085424, Aug 2008.
- [71] M. Mohr, J. Maultzsch, E. Dobardžić, S. Reich, I. Milošević, M. Damnjanović, A. Bosak, M. Krisch, and C. Thomsen. Phonon dispersion of graphite by inelastic x-ray scattering. *Phys. Rev. B*, 76:035439, Jul 2007.
- [72] G. Savini, Y. J. Dappe, S. Öberg, J. C. Charlier, M. I. Katsnelson, and A. Fasolino. Bending modes, elastic constants and mechanical stability of graphitic systems. *Carbon*, 49(1):62 – 69, 2011.
- [73] G. Savini. *Theory of Plastic and Elastic Properties of Graphite and Silicon Carbide*. PhD thesis, University of Bologna, 2007.
- [74] G. Savini and M. I. Heggie. Mesoscale elastic constants in graphite. In *Carbon 2007 Proceedings*, Seattle, Washington, July 2007.
- [75] X. Gonze, J.M. Beuken, R. Caracas, F. Detraux, M. Fuchs, and G. Rignanese. First-principles computation of material properties: the abinit software project. *Comput Mater Sci*, 2002.

- [76] J. P. Perdew and Y. Wang. Accurate and simple analytic representation of the electron-gas correlation-energy. *Phys. Rev. B*, 45(23):13244–13249, 1992.
- [77] Aimpro, 2009. <http://aimpro.ncl.ac.uk>.
- [78] K. Komatsu. Particle-Size Effect Of The Specific Heat Of Graphite At Low Temperatures. *Journal Of Physics And Chemistry Of Solids*, 6(4):380–385, 1958.
- [79] B. T. Kelly. Effects Of Bond-Bending Coefficient On Thermal-Expansion Coefficient Of Graphite Parallel To Hexagonal Axis. *Carbon*, 11(4):379–381, 1973.
- [80] J. Donohue. *The Structures of the Elements*. Krieger, Malabar, 1982.
- [81] L. A. Girifalco and R. A. Lad. Energy of cohesion, compressibility, and the potential energy functions of the graphite system. *J. Chem. Phys.*, 25:693, 1956.
- [82] Lorin X Benedict, Nasreen G Chopra, Marvin L Cohen, A Zettl, Steven G Louie, and Vincent H Crespi. Microscopic determination of the interlayer binding energy in graphite. *Chemical Physics Letters*, 286(56):490 – 496, 1998.
- [83] Renju Zacharia, Hendrik Ulbricht, and Tobias Hertel. Interlayer cohesive energy of graphite from thermal desorption of polyaromatic hydrocarbons. *Phys. Rev. B*, 69:155406, 2004.
- [84] Z. Liu, J. Z. Liu, Y. Cheng, Z. Li, L. Wang, and Q. Zheng. Interlayer binding energy of graphite: A mesoscopic determination from deformation. *Phys. Rev.*, 85:205418, 2012.
- [85] Quanshui Zheng, Bo Jiang, Shoupeng Liu, Yuxiang Weng, Li Lu, Qikun Xue, Jing Zhu, Qing Jiang, Sheng Wang, and Lianmao Peng. Self-retracting motion of graphite microflakes. *Phys. Rev. Lett.*, 100:067205, Feb 2008.

- [86] B. T. Kelly and M. J. Duff. On the validity of lennard-jones potentials for the calculation of elastic properties of a graphite crystal. *Carbon*, 8(1):77 – 83, 1970.
- [87] Leonardo Spanu, Sandro Sorella, and Giulia Galli. Nature and strength of interlayer binding in graphite. *Phys. Rev. Lett.*, 103:196401, Nov 2009.
- [88] Judith Harl and Georg Kresse. Accurate bulk properties from approximate many-body techniques. *Phys. Rev. Lett.*, 103:056401, Jul 2009.
- [89] S. Lebègue, J. Harl, Tim Gould, J. G. Ángyán, G. Kresse, and J. F. Dobson. Cohesive properties and asymptotics of the dispersion interaction in graphite by the random phase approximation. *Phys. Rev. Lett.*, 105:196401, Nov 2010.
- [90] M. Dion, H. Rydberg, E. Schröder, D. C. Langreth, and B. I. Lundqvist. Van der waals density functional for general geometries. *Phys. Rev. Lett.*, 92:246401, Jun 2004.
- [91] Pier Luigi Silvestrelli. Van der waals interactions in dft made easy by wannier functions. *Phys. Rev. Lett.*, 100:053002, Feb 2008.
- [92] Alexandre Tkatchenko and Matthias Scheffler. Accurate molecular van der waals interactions from ground-state electron density and free-atom reference data. *Phys. Rev. Lett.*, 102:073005, Feb 2009.
- [93] Y. J. Dappe, M. A. Basanta, F. Flores, and J. Ortega. Weak chemical interaction and van der waals forces between graphene layers: A combined density functional and intermolecular perturbation theory approach. *Phys. Rev. B*, 74:205434, Nov 2006.
- [94] G. Graziano, J. Klime, F. Fernandez-Alonso, and A. Michaelides. Improved description of soft layered materials with van der Waals density functional theory. *Nature*, 22(71):022201, 2012.
- [95] S. Sorella. <https://qe-forge.org/projects/turborvb/>.

- [96] James P. Lewis, Kurt R. Glaesemann, Gregory A. Voth, Jürgen Fritsch, Alexander A. Demkov, José Ortega, and Otto F. Sankey. Further developments in the local-orbital density-functional-theory tight-binding method. *Phys. Rev. B*, 64:195103, Oct 2001.
- [97] D. R. Bowler, J. Klimes, and A. Michaelides. Chemical accuracy for the van der waals density functional. *J. Phys.: Condens. Matter*, 022201, 2010.
- [98] W. T. Eeles and J. A. Turnbull. The Crystal Structure of Graphite-Bromine Compounds. *Proc. R. Soc. Lond. A*, 28:179 – 193, 1965.
- [99] Steve M. Heald and Edward A. Stern. Extended-x-ray-absorption-fine-structure study of the br₂-graphite system. *Phys. Rev. B*, 17:4069–4081, May 1978.
- [100] T. Sasa, Y. Takahashi, and T. Mukaibo. Crystal structure of graphite bromine lamellar compounds. *Carbon*, 9(4):407 – 416, 1971.
- [101] Ch. Simon, F. Batallan, I. Rosenman, G. Pepy, and H. Lauter. The anisotropy of the c44 shear constant in bromine-graphite intercalation compound: A precursor effect of the anisotropic melting. *Physica B+C*, 136(1-3):15–17, 1986.
- [102] A. Yaya, C. P. Ewels, I. Suarez-Martinez, Ph. Wagner, S. Lefrant, A. Okotrub, L. Bulusheva, and P. R. Briddon. Bromination of graphene and graphite. *Phys. Rev. B*, 83:045411, Jan 2011.
- [103] C.P. Ewels. Private communication.
- [104] G. E. Bacon and B. E. Warren. X-ray diffraction studies of neutron-irradiated graphite. *Acta Crystallogr.*, 9(12):1029–1035, December 1956.
- [105] B. T. Kelly, B. J. Marsden, K. Hall, D. G. Martin, A. Harper, and A. Blanchard. *Irradiation damage in graphite due to fast neutrons in fission and fusion systems*, volume 1154 of *TECDOC*. IAEA, Vienna, 2000.

- [106] B. T. Kelly, W. H. Martin, A. M. Price, P. Dolby, and K. Smith. The annealing of irradiation damage in graphite. *J. Nucl. Mater.*, 20(2):195–209, August 1966.
- [107] M. I. Heggie, I. Suarez-Martinez, C. Davidson, and G. Haffenden. Buckle, ruck and tuck: A proposed new model for the response of graphite to neutron irradiation. *J. Nucl. Mater.*, 413(3):150–155, June 2011.
- [108] A. Asthana, Y. Matsui, M. Yasuda, K. Kimoto, T. Iwata, and K. Ohshima. Investigations on the structural disordering of neutron-irradiated highly oriented pyrolytic graphite by x-ray diffraction and electron microscopy. *J. Appl. Cryst.*, 38(2):361–367, 2005.
- [109] S. Muto and T. Tanabe. Damage process in electron-irradiated graphite studied by transmission electron microscopy. I. high-resolution observation of highly graphitized carbon fibre. *Philos. Mag. A*, 76(3):679–690, September 1997.
- [110] T. Tanabe, S. Muto, and K. Niwase. On the mechanism of dimensional change of neutron irradiated graphite. *Appl. Phys. Lett.*, 61(14):1638–1640, October 1992.
- [111] T. Tanabe, S. Muto, Y. Gotoh, and K. Niwase. Reduction of the crystalline size of graphite by neutron irradiation. *Journal of nuclear materials*, 175(3):258–261, December 1990.
- [112] L. Arnold. *Windscale 1957: anatomy of a nuclear accident*. Macmillan, Basingstoke, 2nd edition, 1995.
- [113] W. H. Zachariasen. *Manhattan Project Report*, 1945.
- [114] A. Grenall. Direct observation of dislocations in graphite. *Nature*, 182(4633):448–450, aug 1958.

- [115] W. Bollmann. Electron-microscopic observations on radiation damage in graphite. *Phil. Mag.*, 5(54):621–624, June 1960.
- [116] E. P. Wigner. On the calculation of the distribution function. *Physical Review*, 61(7-8):524, 1942.
- [117] F. Seitz. On the disordering of solids by action of fast massive particles. *Discuss. Faraday Soc.*, 5(271), 1949.
- [118] T. Iwata and H. Suzuki. Radiation damage in reactor materials - 1962 (proceedings series vol 99). (*Vienna: International Atomic Energy Agency*), pages 565–579, 1963.
- [119] C. A. Coulson, S. Senent, M. A. Herraez, M. Leal, and E. Santos. Deformation of graphite lattices by interstitial carbon atoms. *Carbon*, 3(4):445–457, February 1966.
- [120] B. T. Kelly. Graphite—the most fascinating nuclear material. *Carbon*, 20(1):3–11, 1982.
- [121] P. A. Thrower and R. T. Loader. Interstitial atom energies in graphite. *Carbon*, 7(4):467–477, August 1969.
- [122] W. K. Woods. Proceedings of the first international conference on peaceful uses of atomic energy. volume 7, page 455, New York, 1956. United Nations.
- [123] N. Ghoniem and Amodeo R. Computer simulation of dislocation pattern formation. *Solid State Phenomena*, 3,4:377–388, 1988.
- [124] J. Lepinoux and L.P. Kubin. The dynamic organization of dislocation structures: A simulation. *Phil. Mag. A*, 54:631, 1986.
- [125] J. Lepinoux and L.P. Kubin. The dynamic organization of dislocation structures: A simulation. *Scripta Metallurgica*, 21(6):833 – 838, 1987.

- [126] R. LeSar A. N. Guluoglu, D. J. Srolovitz and R. S. Lomdahl. Dislocation distributions in two dimensions. *Scr. Mater.*, 23:1347, 1989.
- [127] R. J. Amodeo and N. M. Ghoniem. Dislocation dynamics. i. a proposed methodology for deformation micromechanics. *Phys. Rev. B*, 41:6958–6967, Apr 1990.
- [128] R. J. Amodeo and N. M. Ghoniem. Dislocation dynamics. ii. applications to the formation of persistent slip bands, planar arrays, and dislocation cells. *Phys. Rev. B*, 41:6968–6976, Apr 1990.
- [129] R. J. Amodeo and N. M. Ghoniem. Dislocation dynamics. ii. applications to the formation of persistent slip bands, planar arrays, and dislocation cells. *Phys. Rev. B*, 41:6968–6976, Apr 1990.
- [130] L. P. Kubin, G. Canova, M. Condat, B. Devincre, V. Pontikis, and Y. Brechet. Dislocation Microstructures and Plastic Flow: A 3D Simulation. *Solid State Phenomena*, 23-24:445, 1992.
- [131] B. Devincre and M. Condat. Model validation of a 3d simulation of dislocation dynamics: Discretization and line tension effects. *Acta Metallurgica et Materialia*, 40(10):2629 – 2637, 1992.
- [132] A. Moulin, M. Condat, and L.P. Kubin. Simulation of frank-read sources in silicon. *Acta Materialia*, 45(6):2339 – 2348, 1997.
- [133] Hussein M. Zbib, Moono Rhee, and John P. Hirth. On plastic deformation and the dynamics of 3d dislocations. *International Journal of Mechanical Sciences*, 40(23):113 – 127, 1998.
- [134] Kukta R. V. and Freund L. B. Multiscale modelling of material. *MRS Proc. ed V V Bulatov, Tomas Diaz de la Rubia, R Phillips, E Kaxiras and N Ghoniem*, 1998.

- [135] Nasr M. Ghoniem and L. Z. Sun. Fast-sum method for the elastic field of three-dimensional dislocation ensembles. *Phys. Rev. B*, 60:128–140, Jul 1999.
- [136] H. Gao M. J. Buehler, A. Hartmaier. Hierarchical multi-scale modelling of plasticity of submicron thin metal films. *Modelling and Simulation in Materials Science and Engineering*, 12:391–413, 2004.
- [137] H. D. Espinosa, M. Panico, S. Berbenni, and K. W. Schwarz. Discrete dislocation dynamics simulations to interpret plasticity size and surface effects in freestanding fcc thin films. *International Journal of Plasticity*, 22(11):2091 – 2117, 2006.
- [138] V. S. Deshpande, A. Needleman, and E. Van der Giessen. Discrete dislocation plasticity modeling of short cracks in single crystals. *Acta Materialia*, 51(1):1 – 15, 2003.
- [139] N. C. Broedling, A. Hartmaier, and H. Gao. A combined dislocation cohesive zone model for fracture in a confined ductile layer. *International Journal of Fracture*, 140:169–181, 2006.
- [140] Tanmay K. Bhandakkar, Audrey C. Chng, W.A. Curtin, and Huajian Gao. Dislocation shielding of a cohesive crack. *Journal of the Mechanics and Physics of Solids*, 58(4):530 – 541, 2010.
- [141] M.I. Hussein, U. Borg, C.F. Niordson, and V.S. Deshpande. Plasticity size effects in voided crystals. *Journal of the Mechanics and Physics of Solids*, 56(1):114 – 131, 2008.
- [142] Javier Segurado and Javier Llorca. An analysis of the size effect on void growth in single crystals using discrete dislocation dynamics. *Acta Materialia*, 57(5):1427 – 1436, 2009.
- [143] M. P. ODay, P. Nath, and W. A. Curtin. Thin film delamination: A discrete dislocation analysis. *Journal of the Mechanics and Physics of Solids*, 54(10):2214 – 2234, 2006.

- [144] P. J. Guruprasad, W. J. Carter, and A. A. Benzerga. A discrete dislocation analysis of the bauschinger effect in microcrystals. *Acta Materialia*, 56(19):5477 – 5491, 2008.
- [145] S. B. Biner and J. R. Morris. A two-dimensional discrete dislocation simulation of the effect of grain size on strengthening behaviour. *Modelling Simul. Mater. Sci. Eng.*, 10:617, 2002.
- [146] S. Lefebvre, B. Devincere, and T. Hoc. Simulation of the hallpetch effect in ultra-fine grained copper. *Materials Science and Engineering: A*, 400401(0):150 – 153, 2005.
- [147] Srinath S. Chakravarthy and W. A. Curtin. Effect of source and obstacle strengths on yield stress: A discrete dislocation study. *Journal of the Mechanics and Physics of Solids*, 58(5):625 – 635, 2010.
- [148] Naveed Ahmed and Alexander Hartmaier. A two-dimensional dislocation dynamics model of the plastic deformation of polycrystalline metals. *Journal of the Mechanics and Physics of Solids*, 58(12):2054 – 2064, 2010.
- [149] T. Mura. *The continuum theory of dislocations*. In: *Herman, H. (Ed.), Advances in Materials Research, vol. 3*. Interscience Publishers, New York, 1968.
- [150] L. Pang. *A new $O(n)$ method for modeling and simulating the behavior of a large number of dislocations in anisotropic linear elastic media*. DPhil thesis, School of Life Sciences, 2001.
- [151] Qt sdk. <http://qt.nokia.com>.
- [152] F. E. Fujita and K. Izui. Observation of lattice defects in graphite by electron microscopy, part I. *J. Phys. Soc. Jpn.*, 16(2):214–227, February 1961.
- [153] Rob H. Telling and Malcolm I. Heggie. Stacking fault and dislocation glide on

the basal plane of graphite. *Philosophical Magazine Letters*, 83(7):411–421, 2003.

- [154] I. Suárez Martínez. *Theory of diffusion and plasticity in layered carbon materials*. DPhil thesis, School of Life Sciences, University of Sussex, May 2007.
- [155] Imagemagick. <http://www.imagemagick.org/>.
- [156] Niklas Lehto and Sven Öberg. Effects of dislocation interactions: Application to the period-doubled core of the 90° partial in silicon. *Phys. Rev. Lett.*, 80:5568–5571, Jun 1998.
- [157] R. M. J. Cotterill. The physics of melting. *Journal of Crystal Growth*, 48(4):582 – 588, 1980.
- [158] Leonid Burakovsky, Dean L. Preston, and Richard R. Silbar. Melting as a dislocation-mediated phase transition. *Phys. Rev. B*, 61:15011–15018, Jun 2000.